Active/passive Feedback Controls and Energy Harvesting from Vortex-Induced Vibrations

Arshad Mehmood

Dissertation submitted to the Faculty of the Engineering Science and Mechanics
Department of Virginia Polytechnic Institute and State University
in partial fulfillment of the requirements for the degree of

Doctor of Philosophy
in
Engineering Mechanics

Muhammad R. Hajj, Chairman
Saad A. Ragab
Jeffrey T. Borggaard
Calvin J. Ribbens

September 23, 2013
Blacksburg, Virginia

Keywords: Vortex-Induced Vibrations, Actice/passive Controls, Nonlinear Energy Sink,
Rotary Oscillations, Inline Oscillations, Energy Harvesting

Active/passive Feedback Controls and Energy Harvesting from Vortex-Induced Vibrations

Arshad Mehmood

(ABSTRACT)

Fluid-structure interactions occur in many enginnering and industrial applications. Such interactions may result in undesirable forces acting on the structure that may cause fatigue and degradation of the structural components. The purpose of this research is to develop a solver that simulates the fluid-structure interaction, assess tools that can be used to control the resulting motions and analyze a system that can be used to convert the structure's motion to a useful form of energy. For this purpose, we develop a code which encompasses three-dimensional numerical simulations of a flow interacting with a freely-oscillating cylinder. The solver is based on the accelerated reference frame technique (ARF), in which the momentum equations are directly coupled with the cylinder motion by adding a reference frame acceleration term; the outer boundary conditions of the flow domain are updated using the response of the cylinder.

We develop active linear and nonlinear velocity feedback controllers that suppress VIV by directly controlling the cylinder's motion. We assess their effectiveness and compare their performance and required power levels to suppress the motion of the cylinder. Particularly, we determine the most effective control law that requires minimum power to achieve a desired controlled amplitude. Furthermore, we investigate, in detail, the feasibility of using a nonlinear energy sink to control the vortex-induced vibrations of a freely oscillating circular cylinder. It has been postulated that such a system, which consists of a nonlinear spring, can be used to control the motion over a wide range of frequencies. However, introducing an essential nonlinearity of the cubic order to a coupled system could lead to multiple stable solutions depending on the initial conditions, system's characteristics and parameters. Our investigation aims at determining the effects of the sink parameters on the response of the coupled system.

We also investigate the extent of drag reduction that can be attained through rotational

oscillations of the circular cylinder. An optimization is performed by combining the CFD solver with a global deterministic optimization algorithm. The use of this optimization tool allows for a rapid determination of the rotational amplitude and frequency domains that yield minimum drag. We also perform three-dimensional numerical simulations of an inline-vibrating cylinder over a range of amplitudes and frequencies with the objective of suppressing the lift force. We compare the amplitude-frequency response curves, levels of lift suppression, and synchronization maps for two- and three-dimensional flows.

Finally, we evaluate the possibility of converting vortex-induced vibrations into a usable form of electric power. Different transduction mechanisms can be employed for converting these vibrations to electric power, including electrostatic, electromagnetic, and piezoelectric transduction. We consider the piezoelectric option because it can be used to harvest energy over a wide range of frequencies and can be easily implemented. We particularly investigate the conversion of vortex-induced vibrations to electric power under different operating conditions including the Reynolds number and load resistance.

Acknowledgments

Completion of this study would have been impossible for me without the constant guidance from my advisor and colleagues.

I am indebted to Dr. Muhammad R. Hajj, my advisor for his guidance and encouragement. This guidance will be a treasure for my entire professional career. I thank him for all the effort to enhance my approach to the problem formulation and solution. I am also grateful to Dr. Hajj for giving me the freedom to work with many other professors namely Dr. Ali Nayfeh, Dr. Imran Akhtar, Dr. Abdessattar Abdelkefi and Dr. Abdullah Nuhait. I am grateful to Dr. Ali H. Nayfeh, whose mindprovoking comments and guidence always helped my academic pursuit. It is an honour for me having the chance to work with Dr. Nayfeh. My special thanks to Dr. Imran Akhtar for his help and patience to get me started with my research. Dr. Akhtar has always been there to motivate, discuss all the technical, non-technical problems and give precious advices about the future research goals. Special thanks also go to Dr. Abdessattar Abdelkefi with whom I worked on many interesting problems such as energy harvesting and nonlinear phenomena. I would like to also thank Dr. Abdullah Nuhait of King Saud University for helping me in Hamming predictor-corrector method. I would also like to thank Dr. Saad A. Ragab, Dr. Jeff Borggaard and Dr. Calvin J. Ribbens for providing very useful advices and suggestions about my research work and also serving on my PhD committee.

I truly enjoyed sharing the same office with several colleagues. Specially worth noting are Naveed Ahmad and Kareem Akhtar with whom I spent most of my time during my PhD studies. We also shared the same apartment and in the rare free days traveled together. I owe thanks to both for their consistent encouragement and motivation. Dr. Arash Bahrami

is another outstanding colleague, with whom I spent a lot of time discussing the current research areas.

Also, my thanks are given to Dr. Samah Ben Ayed, Haitham Taha, Zhimiao Yan, Youssef Bichiou, Abdulmohsen Alothman, Hassan El-Hady Fayed, Saikat Basu, Saikat Jana, Suvojit Ghosh, Souvick Chatterjee, Umar Kalim and his wife Mariam Umar, Abdul Hafeez, Zaka Ullah Zahid, Tariq Kamal, Abid Ullah, Zeeshan Haider and Zulfiqar Ali who made my stay at Virginia Tech a great experience.

I would like to thank all staff members of the Department of Engineering Science and Mechanics. Special thanks go to Lisa Smith and Anne-Marie Bracken whom helped me in all the departmental documentations.

I am specially grateful to my parents Abdul Khaliq and Booba Khana, my brothers Khalid Mehmood, Asif Mehmood, Qasim Mehmood and Aamir Mehmood, my sisters, Azmat Bano, Tahira Bano, Bushra Bano and Sadaf Bano, my bhabi Farhat Khalid, my brothers in law Zahid Iqbal and Aatif Rahim, my nephews Saim Arman, Muhammad Rehan Iqbal, and my niece Irwa Arman. Their love, duas and encouragement have always been a great source of strength for me. This work is dedicated to them.

At the end, I pray from Almighty Allah, who bestowed all these blessings on me, to give me the strength and wisdom to use this knowlege the way He wants.

Contents

List of Figures

List of Tables

Chapter 1

Introduction

The flow over a circular cylinder and its induced vibrations have been studied extensively because of the complex phenomena involved in this system's dynamics. At low Reynolds number, the flow remains attached over the whole surface of the cylinder. Near a Reynolds number of about 47 (8), flow separation is observed over the rear surface of the cylinder. The nonlinear interaction of the separated shear layer and feedback from the wake results in concentrated alternating vortices, known as the von Kármán vortex street, as shown in Figure 1.1. These vortices are shed with a specific frequency, represented by a nondimensional Strouhal number ($St = \frac{f^*_{vs} D}{U_\infty}$) where f^*_{vs} is the dimensional frequency of vortex shedding, U_∞ is the incoming free-stream velocity, and D the diameter of the cylinder. These shed vortices exert oscillatory forces on the body, which are often decomposed into lift and drag components. If the cylinder is free to move, it responds to these oscillatory forces and the resulting motion is referred as vortex-induced vibrations (VIV), as shown in Figure 1.2. In cases where the vortices are shed at a frequency near the natural frequency of the cylinder, it undergoes high-amplitude oscillations, in a direction perpendicular to the incoming flow. This phenomenon is referred to as "lock-in" or "synchronization" (8–11). During these high-amplitude oscillations, vortices are shed with the cylinder's natural frequency, deviating from the conventional Strouhal number. Real engineering structures have a number of possible mode of vibrations and the synchronization phenomenon can be realized or takes place when the frequency of any structural mode is matched with the frequency of vortex shedding.

Understanding the lock-in phenomenon has been of great interest to many researchers because of its applications in the design and maintenance of engineering structures such as high-rise buildings, bridges, heat exchanger tubes, and in marine technology.

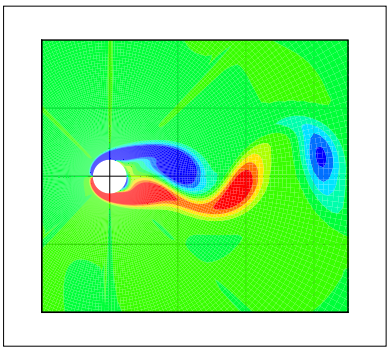

Figure 1.1: Snapshots of the vorticity contours for the flow over a stationary cylinder.

Since Roshko (12) measured the vortex shedding period behind a bluff body, many researchers have investigated this phenomenon experimentally and numerically for a wide range of Reynolds numbers. The flow over a circular cylinder has constituted a canonical problem for studying flow separation, vortex shedding, and associated force coefficients (8; 13–15) in flows over bluff bodies. Bearman (9) gave a detailed survey of the body oscillations, induced by the vortices from bluff bodies of various shapes. He discussed various aspects of free and forced vibrations, difference between cross-flow and inline oscillations, and the phase changes with changes in the body oscillations. Williamson et al. in a series of papers (8; 10; 16; 17), gave a comprehensive review of the experimental and numerical work on vortex-induced vibrations (VIV). They discussed the flow physics related to free and forced vibrations, highlighted some fundamental concepts such as maximum attainable amplitude for a body moving with very small mass and damping, different modes of the system, their associated response between these modes and the effect of Reynolds number on VIV phenomenon. Recently, Gabbai and Benaroya (11) presented a detailed investigation of the experimental and computational solutions, related to the motion induced in structures by shedding vortices. They reviewed the dynamics of freely oscillating cylinder, modes of vortex shedding and also discussed the effect of three-dimensionality.

Anagnostopoulos and Bearman (1) investigated experimentally the phenomenon of vortex-

induced vibrations at low Reynolds numbers between 90 and 150. The experiments were conducted in a small water channel, with a cylinder hinged in a cantilever fashion without attaching end plates. Maximum oscillations-amplitudes were observed at the start of the lock-in regime. They observed a lock-in phenomenon over $104 \leq \mathrm{Re} \leq 126$. Beyond this Reynold number, the lock-in phenomenon bifurcates, and the vortices are shed with the Strouhal frequency and the cylinder oscillates with low modulated amplitudes. Anagnostopoulos (18) also performed numerical investigation of the flow around a freely oscillating circular cylinder in a range to match the experimental (1) regime of the Reynolds number. Analogus to the experimental results, he found that at the lower limit of the lock-in region, the oscillating amplitudes of the cylinder, lift and drag coefficients, remain high and then gradually decreases as the Reynolds number is increased. Blackburn and Henderson (19) investigated the lock-in behavior at Reynolds number equal to 250 by changing the cylinder natural frequency in each simulation. They observed maximum oscillations amplitudes of about $0.45D$ in the middle of the lock-in regime. They termed the response of the cylinder as chaotic outside the lock-in regime.

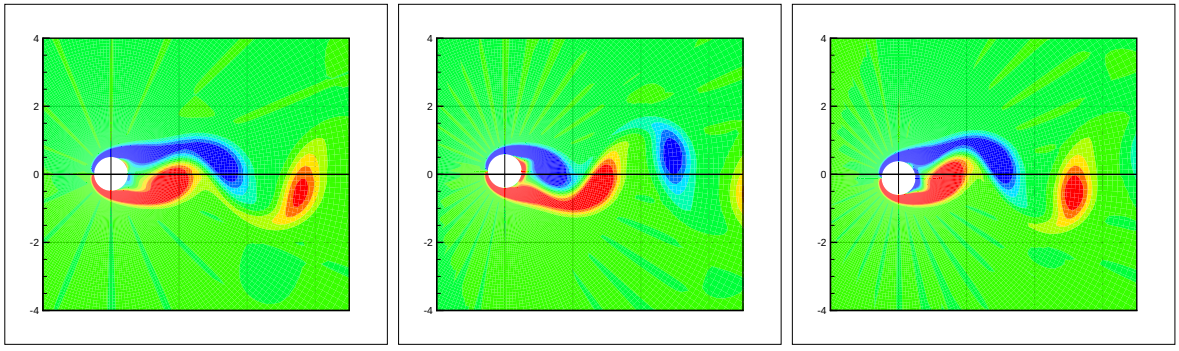

(a) (b) (c)

Figure 1.2: Three snapshots of the vorticity contours for the flow over a freely oscillating cylinder.

1.1 Motivation

Despite the progress in research and technology, the analytical, experimental and numerical investigations of separating flows over complex shapes face significant challenges. Due to the complicated nature of the physical flows, the scope of theoretical analysis has been in general very limited. Experimental techniques have become very sophisticated in recent years, but an extensive spatial and temporal interrogation of complex 3-D flow fields would quickly overwhelm available resources. In terms of cost effectiveness, numerical simulations provide a promising approach when compared to experimental investigation.

The numerical simulation of the equations governing the vortex-induced vibrations of a circular cylinder is very challenging as one cannot solve for the motion of the cylinder without determining the fluid loads. Yet, one cannot determine the fluid loads without the knowledge of the motion of the cylinder. This complication necessitates that equations governing the dynamics of the flow field, and equations which govern the dynamics of the cylinder be solved in a coupled manner. To do so, we consider the fluid flow, and the cylinder as a single dynamical system and use the Hamming fourth-order predictor-corrector technique (20) to overcome the coupling issue. In this technique, the fluid loads (output of the CFD code) are coupled to ODEs governing the motion of the cylinder. Moreover, the governing equations are solved on a parallel platform using the domain decomposition approach on a distributed-memory platform. Message passing interface (MPI) libraries are employed to partition the grid and to communicate among neighboring processors.

The control of vortex-induced vibrations has been a subject of interest in recent years. Reducing or controlling vortex-induced vibrations is desired for enhancing a structure's safety, performance, and lifetime. This can be achieved by reducing the strength of the generated vortices and/or by controlling the motion of the structure in an appropriate manner. Much research has been devoted to the manipulation of the flow over circular cylinders to control the vortex shedding. Both active (21–28) and passive control (29; 30) approaches of VIV of circular cylinders have been explored. Some of the proposed acoustic excitation (21; 26; 27), blowing and suction (24), inline and transverse oscillations(6; 31), rotational oscillations(4; 5; 32–34), and velocity feedback controllers (25). These controllers couple the

control input to the flow instabilities and can operate in a broad range of conditions. However, these active controllers require appropriate sensors and actuators. Proposed passive controllers of VIV includ splitter plates(12; 35; 36), wire ropes and impact, tuned, and structural dampers (30). The wire ropes cause an increase in the natural frequency and damping of the structure. Impact and tuned dampers absorb considerable amount of energy of the vibrating structure. Suppressing the oscillation amplitude of the cylinder in a passive manner would have the added advantages of lower cost and weight and would potentially become an attractive solution for shock and vibration isolation. However, passive controllers are usually designed for a specific oscillation amplitude/frequency and may not be effective over a wide range of oscillation amplitudes and may be constrained to a limited frequency range (30). Recently, Tumkur et al. (37; 38) proposed passive control of VIV of a circular cylinder over a broad frequency range by attaching a secondary system that has an essential nonlinear stiffness. This secondary system is usually termed as nonlinear energy sink (NES). Their results show a reduction in the root mean square (rms) of the oscillation amplitude of the cylinder for different NES masses. However, introducing an essential cubic nonlinearity to a coupled system could lead to multiple stable responses, depending on the initial conditions and the system characteristics and parameters.

When a fluid passes over a cylinder, and vortices are shed at a frequency near the natural frequency of the cylinder, it undergoes high-amplitude oscillations. During this fluid-structure interaction, naturally occuring motion is available, that can be converted by attaching energy harvesting materials. Different transduction mechanisms have been proposed for converting these available vibrations to electric power, including electrostatic (39; 40), electromagnetic (41), and piezoelectric (41; 42) transduction. Of particular interest is the piezoelectric option, which has received the most attention because it can be used to harvest energy over a wide range of frequencies (40) and can be easily implemented. There has been several investigations into different systems for converting aeroelastic vibrations to electric power (43–46).

1.2 Contributions

The major contributions of this thesis are:

1. The development and validation of a parallel CFD code for the direct numerical simulation of the flow field over a freely-oscillating circular cylinder. In this code the incompressible continuity and unsteady Navier-Stokes equations are solved using an accelerated reference frame (ARF) technique. In this method, the momentum equation is directly coupled with the cylinder motion by adding a reference frame acceleration term; the outer boundary conditions of the flow domain are then updated using the response of the cylinder.

2. The characterization of the effects of different initial conditions on the bifurcation leading to the lock-in or synchronization regime. We find that there is an unstable region at both ends of the synchronization regime depending on the initial displacement/velocity of the cylinder. The system's response over the different regions has also been characterized using modern methods of nonlinear dynamics including time histories, power spectra, phase portraits, and Poincaré sections for different sets of initial conditions and Reynolds numbers.

3. A comparison of the effectiveness of linear and nonlinear velocity feedback controllers in suppressing high-amplitude oscillations of an elastically-mounted rigid cylinder. The results show that, for relatively allowed large controlled amplitudes, the linear velocity feedback controller is more efficient. On the other hand, for very small controlled amplitudes, the cubic velocity feedback controller is more efficient.

4. An evaluation of the feasibility of using a nonlinear energy sink (NES) to control the vortex-induced vibrations of a freely oscillating circular cylinder. The results show a significant shortcoming in having multiple solutions including periodic, two-period quasiperiodic, and period-doubled steady-state responses (attractors) that depend on the initial conditions of the cylinder.

5. An optimization of forcing the cylinder with harmonic rotational oscillations to reduce the drag coefficient. For this purpose, we have combined the CFD solver with a global optimizer to speed up the search for the regions where maximum drag reduction can be realized. Our results show that increasing the forcing frequency leads to a reduction in

the drag. We have also observed that there is a threshold of the oscillation amplitude below which the mean drag does not decrease for any forcing frequency. The use of the optimizer enabled the identification of the optimal points where maximum drag reduction is reached.

6. An analysis of the lift suppression phenomenon through forced inline oscillations of the cylinder. We have compared the frequency response curves for two and three dimensional flows and observed a shift in the synchronization maps towards higher frequency ratios/amplitude of oscillations indicating that more energy is required to achieve synchronization in the three-dimensional flow.

7. An assessment of energy harvesting from vortex-induced vibrations of a circular cylinder. Using linear analysis, we have found that the load resistance impacts the onset of synchronization because it affects the global frequency and damping of the electromechanical system. The results also show that the voltage output continuously increases when increasing the load resistance. In contrast, there is an optimum value of the electrical load resistance for which the level of the harvested power is maximum. This value corresponds to the minimum value of the cylinder's displacement which shows that the electrical and mechanical components of the system are tightly coupled.

These contributions will be discussed in the following chapters.

Chapter 2

Numerical Methodology

We present the governing equations which describe the motion of an incompressible flow and cylinder. We implement the accelerated reference frame technique, in which the momentum equation is directly coupled with the cylinder motion by adding a reference frame accelaration term. The outer boundary condition of the flow domain are changed according to the response of the cylinder. We employ Hamming's fourth-order predictor-corrector method that accounts for the interaction between the fluid loads and the motion of the cylinder. This approach considers the fluid and the cylinder as elements of a single dynamical system and integrates all of the governing equations simultaneously, and interactively in the time domain. We also validate the developed code.

2.1 Introduction

The numerical solutions of the flow that interacts with the freely moving structures are considered to be among the most challenging problems in fluid science. The complication arises due to the dependence of fluid forces on the structural motion and vice versa *i.e.*, the structure moves and changes its position in response to the flowing fluid load, and similarly flowing fluid changes its position to accommodate the structural motion. These responses results from fluid-structure coupling. In order to simulate this problem, different formulations have been developed such as the arbitrary Lagrangian-Eulerian (ALE) method (3; 47), immersed boundary (IB) methods (2; 48), and the accelerating reference frame (ARF) method (49; 50).

In the arbitrary Lagrangian-Eulerian (ALE) method, the computational mesh local to the structure is distorted continuously in time as the structure moves. The boundary conditions on the body and in the far field are usually fixed in time. The disadvantages of this approach in terms of computational cost, is the re-meshing and the temporal changes of the mesh interpolation functions. Schulz and Kallinderis (3) proposed a loosely coupled numerical scheme where the fluid and the cylinder dynamics were solved independentaly for each time step. In the implemented scheme, an ALE finite element formulations was used, where the mesh is distorted and regenerated following the motion of the cylinder as it moves through the fluid. In the immersed boundary (IB) methods, the flow is simulated with immersed boundaries where the grid boundaries do not conform to the defined boundaries. The advantage of this method appears in the grid generation, which does not require coordinate transformation at every increment of body motion. However, applying appropriate boundary conditions is not straightforward and resolving the boundary layer at high Reynolds numbers increases the grid-size requirement faster than a corresponding body conformal grid. More recently, Yang et al. (2) investigated the fluid-structure interaction phenomenon at low Reynolds number using embedded-boundary formulation. Fluid flow is solved on a Cartesian grid, which was not alligned to the boundaries of the cylinder. An alternative to this method is the accelerating reference frame (ARF) method (50). Unlike ALE, the mesh is fixed to the structure, allowed it to move in space with the structure and the momentum equations and corresponding boundary conditions are modified accordingly to accommodate this motion. In this way, the computational overhead associated with the coordinate transformation at every time step is avoided (49).

2.2 Numerical Methodology

2.2.1 Structure Equation

In an inertial reference frame, the governing equations of an elastically-mounted rigid cylinder, allowed to vibrate only in the transverse direction, as shown in Fig. 2.1, is expressed as:

$$M\ddot{Y} + C\dot{Y} + KY = F_Y(t) \tag{2.1}$$

where M is the oscillating structural mass per unit length, C and K are the structural damping and stiffness, respectively. $F_Y(t)$ characterizes the time-dependent external excitation from the fluid flow applied on the structure. The response of the structure is described by the displacement Y, the velocity $\dot{Y}$ and the acceleration $\ddot{Y}$.

Equation (2.1) is nondimensionalized using the cylinder diameter D as a reference length, and incoming freestream velocity U_∞ as a reference velocity and is rewritten as:

$$\ddot{Y}^* + 2\zeta(\frac{2\pi}{U_r})\dot{Y}^* + (\frac{2\pi}{U_r})^2 Y^* = \frac{2}{\pi m^*} C_Y \tag{2.2}$$

where $Y^* = Y/D$ is the nondimensional transverse cylinder displacement, $U_r = \frac{U_\infty}{f_n D}$ is the reduced velocity, $\zeta = C/C_{crit} = C/2\sqrt{KM}$ is the structural damping ratio, $m^* = \frac{M}{M_f}$ the mass ratio where $M_f = \rho_f \frac{\pi}{4} D^2$ represents the fluid mass replaced by the cylinder per unit length, f_n the natural frequency of the cylinder, and C_Y represents the lift coefficient, which is computed from the numerical simulation of the flow field.

Equation (2.2) can be equivalently rewritten as a system of two coupled first-order ordinary differential equations as follows,

$$\dot{y_1} = y_2, \tag{2.3}$$

$$\dot{y_2} = -2\zeta(\frac{2\pi}{U_r})y_2 - (\frac{2\pi}{U_r})^2 y_1 + \frac{2}{\pi m^*} C_Y, \tag{2.4}$$

where $y_1 = Y^*$, $y_2 = \dot{Y}^*$.

2.2.2 Flow Equations

The governing equations describing the relative motion of incompressible fluid in the Cartesian reference frame attached to the structure take the following form

$$\frac{\partial u_i}{\partial x_i} = 0 \tag{2.5}$$

$$\frac{\partial u_i}{\partial t} + \frac{\partial}{\partial x_j}(u_j u_i) = -\frac{\partial p}{\partial x_i} + \nu \frac{\partial^2 u_i}{\partial x_j \partial x_j} - \ddot{Y}_i^*, \tag{2.6}$$

where i,j=1,2,3; u_i represents the cartesian velocity components; p and ν are, respectively, the pressure and kinematic viscosity of the fluid. Equations (2.5) and (2.6) are also nondimensionalized using the same reference scale, *i.e*, the diameter of the cylinder D and the incoming freestream velocity U_∞. The flow Reynolds number is defined as $Re = \frac{U_\infty D}{\nu}$.

Equations (2.2) and (2.6) are coupled through the cylinder's acceleration $\ddot{Y}_i^*$, which is along the cross-flow direction in the current simulations. Using the ARF technique, the momentum equations are directly coupled with the cylinder motion by adding a reference frame acceleration term (49); the outer boundary conditions of the flow domain are then updated in accordance to the response of the cylinder. At the domain boundary, the velocity boundary condition is modified to include the effects of moving cylinder, such that

$$u = u_D - v \tag{2.7}$$

where u_D is the velocity in the inertial frame of reference and $v = \dot{Y}_i^*$ is the cylinder's velocity. On the structure surface, the velocity boundary condition is typically $u_i = 0$. In the far field boundary, $\frac{\partial u_i}{\partial t} = -\ddot{Y}_i^*$, while on the surface $\frac{\partial u_i}{\partial t} = 0$ and $u_i = 0$. The lift coefficient is computed from the surface pressure as

$$C_L = -\int_0^{2\pi} \left(p \ \sin\theta - \frac{1}{\mathrm{Re}} \omega_z \ \cos\theta \right) d\theta, \tag{2.8}$$

where ω_z is the spanwise vorticity component on the cylinder surface and θ is the angle that the outer normal of the area component makes with the flow direction. An "O"-type grid is employed to simulate the flow over the cylinder as shown in Fig. 2.2.

The governing equations are solved on a nonstaggered grid topology (51). The Cartesian velocity components (u, v,w) and pressure (p) are defined at the center of the control volume in the computational space. A second-order central-difference scheme is used for

all spatial derivatives except for convective terms, which are discretized using QUICK (52). The temporal advancement is performed using a fractional step method where a predictor step calculates an intermediate velocity field, and a corrector step updates the velocity by satisfying the pressure-Poisson equation at the new time step. The diagonal viscous terms are advanced implicitly using the second-order accurate Crank-Nicolson method, whereas all of the other terms are advanced using the second-order accurate Adams-Bashforth method. Further details of the numerical discretization and the parallel implementation can be found in Refs. (24; 28; 53).

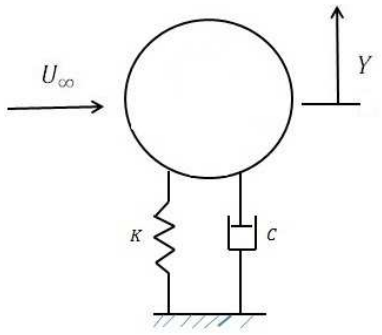

Figure 2.1: A schematic diagram of an elastically-mounted cylinder.

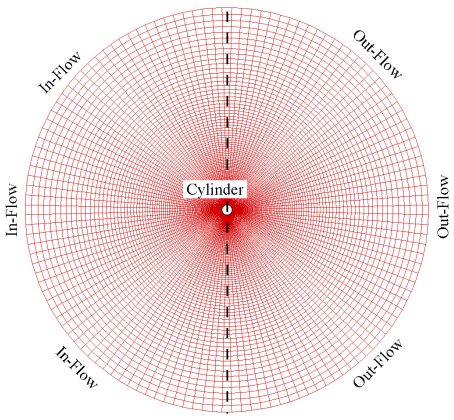

Figure 2.2: A 2-D layout of an "O"-type grid in the (r, θ)-plane.

2.3 Fluid-Structure Coupling (Predictor-Corrector)

In performing the simulations, equations (2.5) and (2.6), which govern the dynamics of the fluid flow, and equations (2.2), which govern the dynamics of the cylinder, must be solved in a coupled manner. To do so, we consider the fluid flow, the cylinder motion as a single dynamical system, and use the Hamming fourth-order predictor-corrector technique (20; 54) to overcome the coupling issue. In this technique, the fluid loads (equation 2.8) are coupled to the ODEs (equations 2.3 and 2.4) governing the motion of the cylinder. The basic idea is that the predicted state of the cylinder, based on the fluid load that is computed in the previous time step, is used in the CFD code to compute the new fluid load. This load is then used to compute the new state of the cylinder, using the corrector scheme. These steps are repeated until a match between the fluid load and the cylinder motion, as defined by a specified conditional error at each time step is reached.

2.4 Predictor-Corrector Scheme

In order to describe the numerical procedure of solving the equations of motion, we will write Equations (2.3) and (2.4) in the following set of system of first-order differential equations:

$$\dot{y}(t) \ = f(t, y_i(t)) \qquad \text{for i } = 1, 2, ... \text{ no. of state space variables} \tag{2.9}$$

Let $t_j = j\Delta t$ denotes the time at the $j-th$ time step, where Δt is the time-step size used to obtain the numerical solution, and

$$y_j = y(t_j) \tag{2.10}$$

$$\dot{y}_j = \dot{y}(t_j) \tag{2.11}$$

$$f_j = f[y(t_j)] \tag{2.12}$$

At t_0 (i.e., t=0), the initial conditions of the system are known, i.e., we know $y_0 = y(t_0)$ and using equation (2.9) we obtain the value of $\dot{y}_0$ as:

$$\dot{y}_0 = f_0 = f(y(t_0)) \tag{2.13}$$

1. **Step1-(Euler and modified Euler method)**

   (a) At t_1 (i.e., $t = 1\Delta t$), the predicted state, y_1^p, of the system is computed by the Euler Method as:

   $$y_1^p = y_0 + \Delta t f_0 \tag{2.14}$$

   (b) The predicted state, y_1^p, of the system is then corrected by the modified Euler method as:

   $$^{k+1}y_1^c = y_0 + \frac{\Delta t}{2}(^k f_1 + f_0) \tag{2.15}$$

   where k denotes the iteration counter, and

   $$^k f_1 = f(^k y_1)$$

   where $^1 y_1 = y_1^p$

   (c) These steps are repeated until the iteration error is less than the predefined value ϵ.

   $$e_1 = \|^{k+1} y_1 - ^k y_1 \|_\infty \tag{2.16}$$

   If $e_1 > \epsilon$ then we set

   $$^k y_1 = {}^{k+1}y_1^c \tag{2.17}$$

   $$^k f_1 = {}^k \dot{y}_1 = {}^{k+1}\dot{y}_1^c \tag{2.18}$$

   and then using equation (2.15), the state of the system is recalculated $^{k+1}y_1^c$; if $e_1 \leq \epsilon$ then we set

   $$y_1 = {}^{k+1}y_1^c \tag{2.19}$$

   $$f_1 = \dot{y}_1 = {}^{k+1}\dot{y}_1^c \tag{2.20}$$

   and compute the state of the system at $t_2 = t_1 + \Delta t$

2. **Step2-(Adams-Bashforth and Adams-Moulton 2-step methods)**

   (a) At t_2 (i.e., $t = 2\Delta t$)), the predicted state, y_2^p, of the system is computed by the Adams-Bashforth two step method

   $$y_2^p = y_1 + \frac{\Delta t}{2}(3f_1 - f_0) \tag{2.21}$$

(b) The predicted state, y_2^p, of the system is then corrected by the Adams-Moulton two step method

$$^{k+1}y_2^c = y_1 + \frac{\Delta t}{12}(5^k f_2 + 8^k f_1 - f_0) \tag{2.22}$$

where

$$^k f_2 = f(^k y_2)$$

and $^1y_2 = y_2^p$

(c) These steps are repeated until the iteration error is less than the predefined value ϵ

$$e_2 = \|^{k+1}\, y_2 - ^k\, y_2 \,\|_\infty \tag{2.23}$$

If $e_2 > \epsilon$ then we set

$$^k y_2 = {}^{k+1}y_2^c \tag{2.24}$$

$$^k f_2 = {}^k\, \dot{y}_2 = {}^{k+1}\dot{y}_2^c \tag{2.25}$$

and then using equation (2.22), the state of the system is recalculated $^{k+1}y_2^c$; if $e_2 \leq \epsilon$ then we set

$$y_2 = {}^{k+1}y_2^c \tag{2.26}$$

$$f_2 = \dot{y}_2 = {}^{k+1}\dot{y}_2^c \tag{2.27}$$

and compute the state of the system at $t_3 = t_2 + \Delta t$

3. **Step3-(Adams-Bashforth and Adams-Moulton 3-step methods)**

(a) At t_3 (i.e., $t = 3\Delta t$), the predicted state, y_3^p, of the system is computed by the Adams-Bashforth three step method

$$y_3^p = y_2 + \frac{\Delta t}{12}(23f_2 - 16f_1 + 5f_0) \tag{2.28}$$

(b) The predicted state, y_3^p, of the system is then corrected by the Adams-Moulton three step method

$$^{k+1}y_3^c = y_2 + \frac{\Delta t}{24}(9^k f_3 + 19f_2 - 5f_1 + f_0) \tag{2.29}$$

where

$$^{k}f_3 = f(^{k}y_3)$$

and $^{1}y_3 = y_3^p$

(c) These steps are repeated until the iteration error is less than the predefined value ϵ.

$$e_3 = \|^{k+1}\, y_3 - ^{k}\, y_3 \,\|_{\infty} \tag{2.30}$$

If $e_3 > \epsilon$ then we set

$$^{k}y_3 = {}^{k+1}y_3^c \tag{2.31}$$

$$^{k}f_3 = {}^{k}\,\dot{y}_3 = {}^{k+1}\dot{y}_3^c \tag{2.32}$$

and then using equation (2.29), the state of the system is recalculated $^{k+1}y_3^c$; if $e_3 \leq \epsilon$ then we set

$$y_3 = {}^{k+1}y_3^c \tag{2.33}$$

$$f_3 = \dot{y}_3 = {}^{k+1}\dot{y}_3^c \tag{2.34}$$

and compute the state of the system at $t_4 = t_3 + \Delta t$

4. **Step4-(Hamming 4th order Predictor-Corrector methods)**

(a) For $t \geq t_4$, the system response is computed by using Hamming's fourth-order predictor corrector method. The predicted state, y_t^p, of the system is computed as:

$$y_t^p = y_{t-4} + \frac{4\Delta t}{3}(2f_{t-1} - f_{t-2} + 2f_{t-3}) \tag{2.35}$$

(b) The predicted state, y_t^p, of the system is modified using the local truncation error which is calculated from the previous time step

$$^{mp}y_t = y_t^p + \frac{112}{9}e_{t-1} \tag{2.36}$$

(c) The modified-predicted state, y_t^p, of the system is then corrected using the Hamming's Corrector Equation as:

$$^{k+1}y_t^c = \frac{1}{8}(9y_{t-1} - y_{t-3} + 3\Delta t(^{k}f_t + 2f_{t-1} - f_{t-2})) \tag{2.37}$$

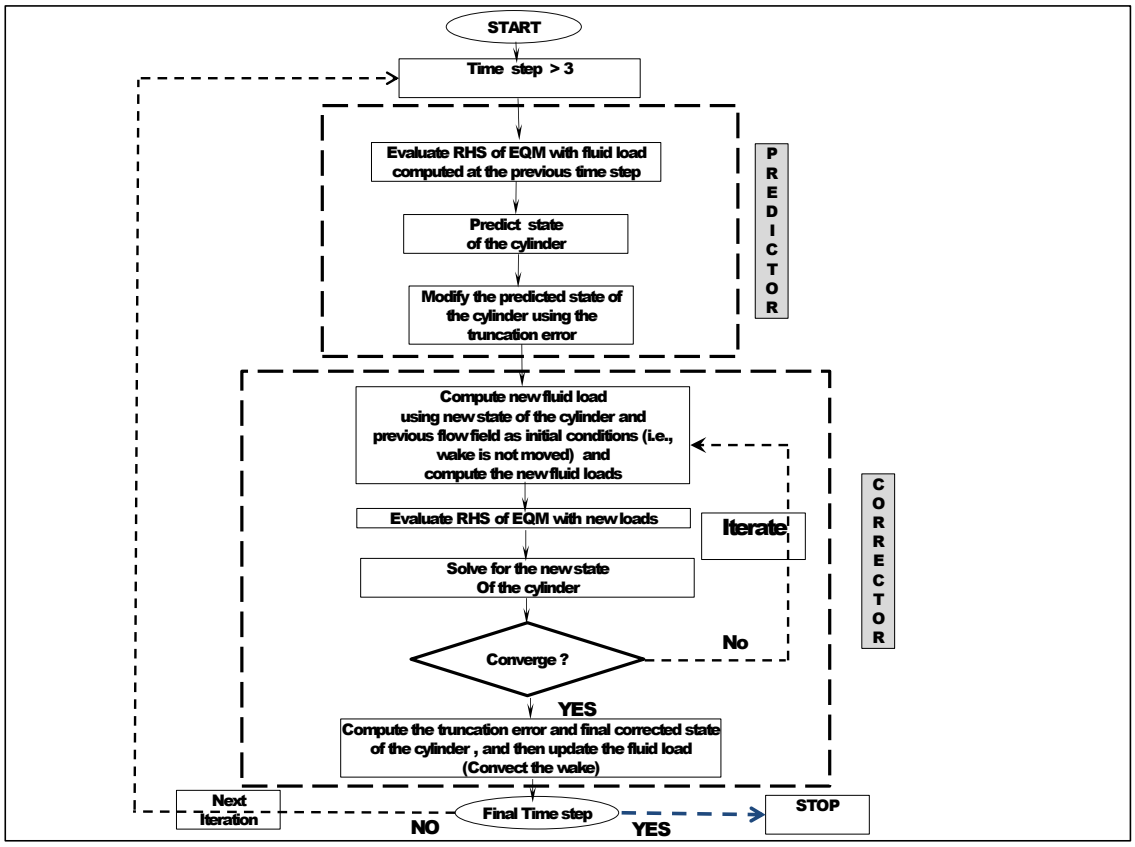

Figure 2.3: layout of predictor-corrector scheme

where

$$^{k}f_t = f(^{k}y_t)$$

and $^{1}y_t = y_t^{mp}$

(d) These steps are repeated until the iteration error is less than the predefined value ϵ.

$$e_t = \|^{k+1} y_t - ^{k} y_t \|_{\infty} \tag{2.38}$$

If $e_t > \epsilon$ then we set

$$^{k}y_t = {}^{k+1}y_t^c \tag{2.39}$$

$$^{k}f_t = {}^{k}\dot{y}_t = {}^{k+1}\dot{y}_t^c \tag{2.40}$$

Also, the local truncation error is calculated to be used in the current and next time steps as

$$e_t = \frac{9}{121}({}^{k+1}y_t - {}^{mp}y_t) \tag{2.41}$$

and go to equation (2.37) to recalculate ${}^{k+1}y_t^c$; if $e_t \leq \epsilon$ then final solution at step t is

$$y_t = {}^{k+1}y_t^c - e_t \tag{2.42}$$

5. To calculate the solution at the next time step, we update the table of y's and f's as

   $y_{t-4} = y_{t-3}, y_{t-3} = y_{t-2}, y_{t-2} = y_{t-1}, y_{t-1} = y_t$

   and

   $f_{t-3} = f_{t-2}, f_{t-2} = f_{t-1}, f_{t-1} = f_t$

   also

   $e_{t-1} = e_t$

   and go to equation (2.35) to repeat the procedure.

   During the continuous flow, so at any time t, the flow variables moves to their new positions and simultaneously, the cylinder moves to its new position. As the flow (i.e.,wake) is convected to its new position, the fluid load is calculated and the whole flow variables are freezed at this time. Using this fluid load, the current state of the cylinder is predicted using equations (2.35) and (2.36). At this stage (end of predictor section), the number of iterations are set equal to one. At this level, the reponse of the cylinder is found and is supplied to the fluid solver in order to compute newe fluid loads for this time step. Note that, the fluid load is computed using the previous flow field (i.e., frozen variables) with the new state (i.e, based on the predictor section) of the cylinder. The right hand side of equation (2.9) is re-evaluated at the current time step. Then Hamming's corrector equation (2.37) is used to compute the corrected solution ${}^{k+1}y_t^c$. The condition of convergence is evaluated. If the convergence is not satisfied, then according to equations (2.39), the procedure is repeated until there is convergence. After convergence, equation (2.42) is used to find the final position and velocity of the

cylinder and then these are used to compute the flow field for the next time step. The above overall coupling scheme has been summarized in the flow chart, as shown in figure. (2.3).

2.5 Validation of the Fluid Flow Solver and the Coupling Scheme

We validate the fluid flow solver and the coupling scheme by comparing the results of our numerical simulations with the experimental results of Anagnostopoulos and Bearman (1) and other numerical simulations performed of Yang et al. (2) and Schulz (3). We consider the same parametric study case as in the experimental work of (1) *i.e.*, mass ratio $m^* = \frac{M}{M_f} = 149.10$ and damping ratio $\zeta = 0.0012$. The numerical simulations were performed on a computational domain of $25D$ with a resolution of 192×252 grid points in r and θ directions, respectively. A time step of $\Delta t = 0.002$ is used in all simulations. Numerical simulations were performed in the range of $96 \leq \mathrm{Re} \leq 140$ and each simulation corresponds to a specific Reynolds number. In order to measure the vortex shedding frequency for a specific Reynolds number, the flow passing over a fixed cylinder at that Reynolds number was initially computed. Figure 2.4 shows the time history and power spectrum of the lift coefficient, respectively, for a stationary cylinder when $\mathrm{Re} = 104$. The lift coefficient oscillates with a peak value of $C_Y = 0.2931$ as presented in figure. 2.4(a). The power spectrum of the lift coefficient shows that vortices are shed at a nondimensional frequency $f_{st} = 0.1564$, as shown in figure. 2.4(b).

Afterwards, the cylinder was allowed to oscillate freely under the action of the fluid force in the transverse direction. Each simulation was run long enough to make sure that steady-state oscillations are obtained. After reaching the steady state, the cylinder response amplitude ($\frac{Y_{max}}{D}$), oscillation frequency (f_c), and the vortex shedding frequency (f_{vs}) are obtained. Figure 2.5 shows the variation of the nondimensional maximum oscillation amplitude $\frac{Y_{max}}{D}$ of the cylinder as a function of the Reynolds number. It follows from this plot that our simulations are in good agreement with the experimental results of Anagnostopoulos and Bearman (1) and particularly in finding the location of the bifurcation point (onset of synchronization) than the previously reported numerical simulations (2; 3). However, there is a small differ-

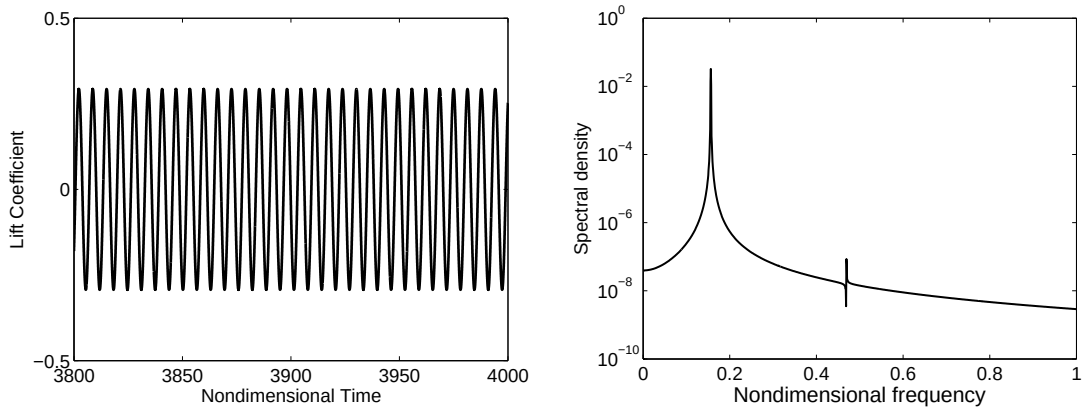

(a) (b)

Figure 2.4: (a) Time history and (b) power spectrum of the lift coefficient for a stationary cylinder when Re = 104.

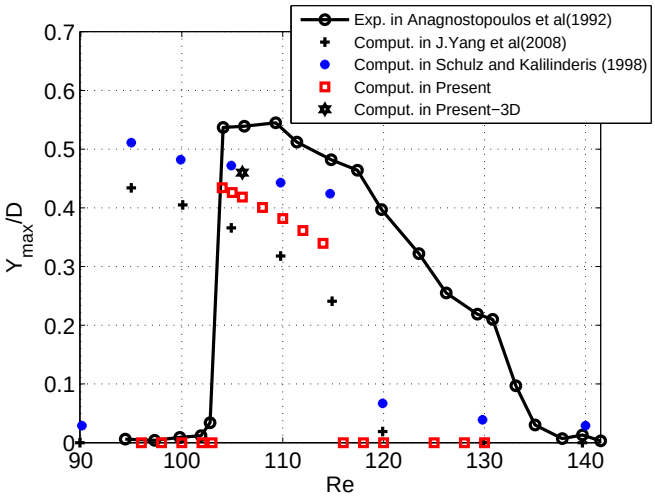

Figure 2.5: Comparison of the maximum displacement amplitudes as predicted in our numerical simulations (◇) with the experimental measurements (1)(-○) and other numerical simulations (2) (∗) and (3) (+).

ence between our numerical simulations and the experimental results (1) when comparing the maximum amplitudes and the range of the synchronization regime. This difference could be due to three-dimensional effects, since the experiments were performed without end plates.

The current author performed numerical simulations for three-dimensional flow at Re = 106 and found higher amplitudes as shown in Figure 2.5 with *asterisk* symbol.

Chapter 3

Phenomena and Nonlinear Characterization of Vortex-Induced Vibrations of a Circular Cylinder

We investigate the effects of a set of different initial conditions around the onset of its bifurcation region. We find an unstable region at both ends of the synchronization regime. We also characterize the system's response and observe a periodic response within the synchronization regime and period-n (where n $>$ 1), quasiperiodic and chaotic responses outside the synchronization regime.

3.1 Introduction

It has been observed that structures experience oscillations by extracting energy from the flow near linear resonance conditions. These oscillations modify the flow and give rise to nonlinear interactions. The excitation force results from flow separation has a nonlinear aspect that could interact with the structure and may vary the bounds of the large-amplitude oscillations regime. Feng (55) was the first one who observed that higher amplitudes were obtained during the forward sweep of the reduced velocity and a different bound of higher oscillating amplitude were obtained when the reduced velocity is swept back over the same range. After

their findings, the hysteresis effect has been the topic of interest of many studies. Inspecting the plotted curves in figure 2.5, we note that in the reported numerical simulations of Yang et al. and Schulz (2; 3), the onset of synchronization phenomenon is observed much earlier than that of the experimental observations. We argue that there exists an unstable region around the bifurcation point. To this end, we consider different sets of initial conditions to check the presence of the unstable branches.

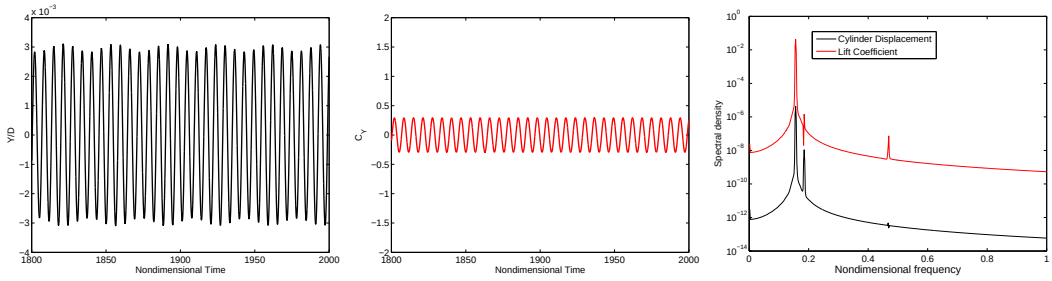

(a) (b) (c)

Figure 3.1: Time histories of the (a) cylinder transverse displacement, (b) fluctuating lift coefficient, and (c) power spectra of the cylinder displacement and lift coefficient when Re = 96.

3.2 System Response for Zero Initial Conditions

In the first case, all the numerical simulations were started from rest (*i.e.*, zero initial conditions). Time histories of the cylinder oscillation amplitude, lift coefficient, and their corresponding power spectra are shown in Figs. 3.1(a), 3.1(b), 3.1(c), respectively, for Re = 96. From figure 3.1(a), we note that the oscillation amplitude of the cylinder is modulated and the oscillations remains very low ($\frac{Y}{D} \sim 10^{-3}$). Inspecting the time history of the lift coefficient as presented in figure 3.1(b), it is clear that it oscillates around a zero mean with a peak value of ($C_Y = 0.293$). The power spectrum of the motion and the lift coefficient, as shown in figure 3.1(c), reveal that the lift coefficient has a major peak at 0.1564 and a neighboring smaller one at 0.185 and an additional peak at $3f_{vs} = 0.4692$. The cylinder's

motion has peaks at the same values but they are orders of magnitude smaller than the lift coefficient. Qualitatively, similar low modulated oscillation amplitudes are observed as the Reynolds number is increased, till reaching Re = 104.

As the value of the Reynolds number reaches 104, there is a dramatic change in the nature of the oscillation amplitude of the cylinder and lift coefficient. At this Reynolds number, the amplitude of cylinder oscillation increases continuously and reaches a stable limit cycle oscillations (LCOs), as shown in figure 3.2(a). The plot shows that the cylinder oscillations reaches a peak amplitude of over 43% of the cylinder diameter. The lift coefficient (C_Y) also oscillates with a higher amplitude with a peak value of ($C_Y = 1.5156$), as presented in figure 3.2(b). Both the lift coefficient and the motion of the cylinder appear to be pure periodic. The power spectra of the cylinder's response and the lift coefficient, as shown in figure 3.2(c), show that both the frequencies are locked-in to the same frequency (i.e., 0.1727). This is approximately equal to the natural vibrational frequency of the cylinder ($f_n^* = f_n \frac{D^2}{\mathrm{Re}\ \nu} = 7.016 * \frac{(1.6\times10^{-3})^2}{104*1\times10^{-6}} = 0.1717$). However, we have to mention that the vortex-shedding frequency at this Reynolds number (i.e., 104) is $f_{st} = 0.1564$, as shown in figure 2.4(b). Here, we can inferred that in the lock-in regime the cylinder oscillation frequency controls the flow pattern. This Reynolds number lies in the synchronization regime and the range extends upto Re = 114.

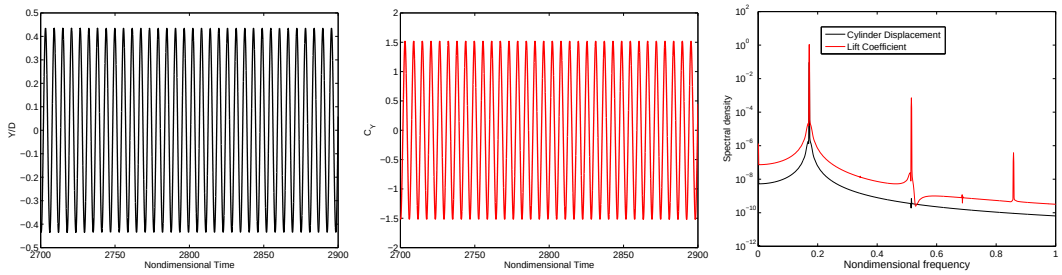

(a) (b) (c)

Figure 3.2: Time histories of the (a) cylinder transverse displacement, (b) fluctuating lift coefficient, and (c) power spectrum of the cylinder displacement and lift coefficient when Re = 104.

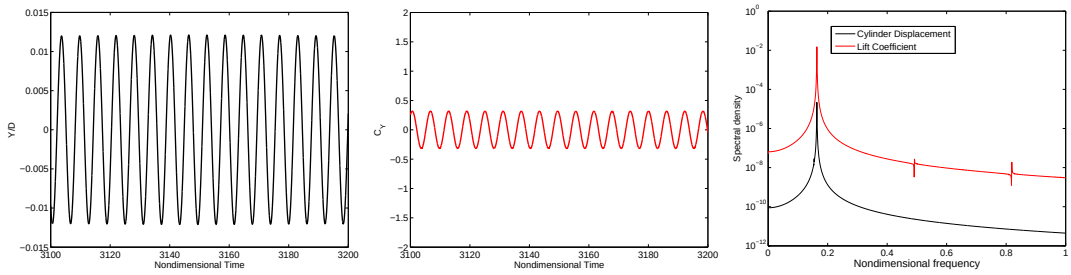

(a) (b) (c)

Figure 3.3: Time histories of the (a) cylinder transverse displacement, (b) fluctuating lift coefficient, and (c) power spectrum of the cylinder displacement and lift coefficient when Re = 116.

At Re = 115, the locked-in phenomenon bifurcates and the cylinder oscillates with smaller amplitudes, as shown in figure 3.3(a). The lift coefficient, presented in figure 3.3(b), also shows low-amplitude oscillations. The power spectra of the cylinder displacement and the lift coefficient show that the lift coefficient has a major peak at 0.1636, as shown in figure 3.3(c). The cylinder motion also shows the same peak but it is few orders of magnitude smaller than the lift coefficient. Qualitatively, similar low oscillation amplitudes are observed beyond Re = 114.

3.3 Effect of Initial Conditions: Hysterisis Region

To investigate the presence of any bifurcation phenomenon (unstable solutions) lower than Re = 104, we assess the effects of the initial conditions on the response of the system. Numerical simulations were performed for different sets of initial conditions. For that purpose, we vary the velocity of the cylinder (y_2) while keeping the cylinder displacement $y_1 = 0$. Figures 3.4(a) and 3.4(b) show the variations of the nondimensional RMS values of the oscillation amplitude and lift coefficient as a function of the Reynolds number. It is apparent from these plots that the range of synchronization regime is wider when considering non-zero initial conditions than the trivial case (i.e., with zero initial conditions). However, the

RMS oscillation amplitudes of the cylinder and the lift coefficient remain the same in the synchronization intersection range. Variations in the bounds of the different regimes (*i.e.*, presynchronous, synchronous, and postsynchronous) when varying the set of initial conditions of the cylinder are shown in Table 3.1.

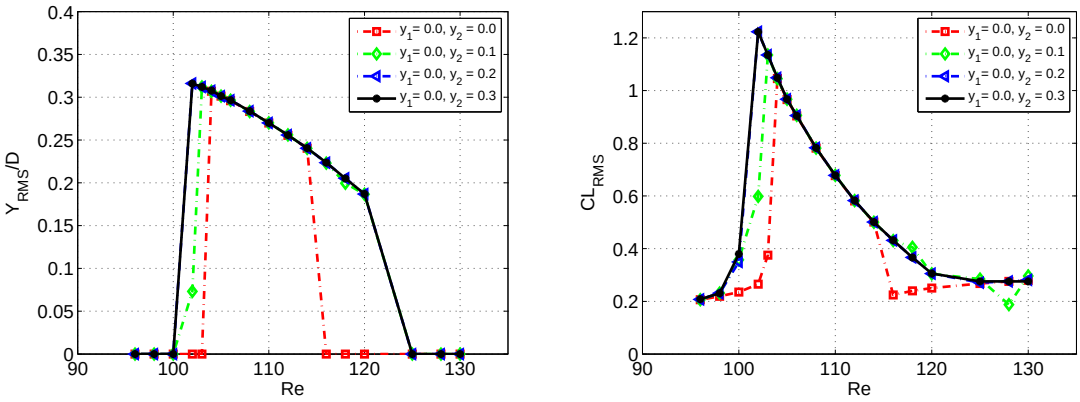

(a) (b)

Figure 3.4: Variations of the nondimensional RMS value of the (a) transverse displacement and (b) fluctuating lift coefficient as a function of the Reynolds number for different sets of initial conditions.

Table 3.1: Different regimes based on the response of the cylinder.

Cases	Initial Conditions	Pre-synchronous	Synchronization	Post-synchronous
1	$y_1 = 0.0, y_2 = 0.0$	$\mathrm{Re} < 104$	$104 \leq \mathrm{Re} \leq 114$	$\mathrm{Re} > 114$
2	$y_1 = 0.0, y_2 = 0.1$	$\mathrm{Re} < 103$	$103 \leq \mathrm{Re} \leq 120$	$\mathrm{Re} > 120$
3	$y_1 = 0.0, y_2 = 0.2$	$\mathrm{Re} < 102$	$102 \leq \mathrm{Re} \leq 120$	$\mathrm{Re} > 120$
4	$y_1 = 0.0, y_2 = 0.3$	$\mathrm{Re} < 102$	$102 \leq \mathrm{Re} \leq 120$	$\mathrm{Re} > 120$

To characterize exactly the response of the system and differentiate between different responses (*i.e.*, periodic, quasiperiodic, and chaotic), we use modern methods of nonlinear dynamics including time histories, power spectra, phase portraits, and Poincaré sections for different sets of initial conditions and Reynolds numbers. Time histories can be used to

characterize the low-order periodic responses of the system. The response is period-1, when the time trace has a uniform and harmonic behavior and also the motion cycle completes approximately equal to the period of the cylinder motion. Period-n, where n ≥ 2, responses are observed when the time trace is modulated and the motion cycle completes at n-times of the period of cylinder motion. However, for very small and modulated motions, it is hard to characterize the response of the system based on the time history. Considering the power spectrum of the motion of the cylinder, the response of the system is period-1 when it has a single sharp peak at the cylinder vibration frequency. For high-order periodic responses, the power spectrum shows sharp peaks at the vortex shedding frequency (f_{vs}) and at its subharmonics. However, when the number of spikes are too many and also when the spikes are not commensurate with the excitation frequency, then the system characterization using the power spectrum method is not feasible. Next, we use the two-dimensional projections of the phase-portrait onto the $y_1 - y_2$ plane to characterize the response of the system. The system response is periodic, if a closed orbit in the state space is obtained. The number of closed orbits corresponding to the number of periods. However, for highly modulated responses, it is not convenient to count the number of orbits and also whether they are closing on themselves.

For period-n responses time histories, power spectrum, phase portraits are generally enough to characterize the response of the system. However, when the response of the system is somehow complicated, these tools are not useful to discriminate between period-n, quasiperiodic, and chaotic responses. Consequently, we use the Poincaré sections to determine the correct response. Here, period-n responses correspond to n-discrete points. Quasiperiodic responses correspond to infinitely many points falling on a closed curve. If neither finite number of points nor infinitely points falling on a closed curve, the response is chaotic. Using these advanced tools of nonlinear dynamics, we found different behaviors of the system before, within and after the onset of synchronization.

The plotted curves in Figs. 3.5 show the response of the coupled system at Re = 96 for different initial conditions. For the trivial initial conditions ($y_1 = 0.0$ and $y_2 = 0.0$), we observe a damped response of the system as shown in figure 3.5(a). It follows from the steady state response that the motion of the cylinder is modulated with small amplitude as

shown in figure 3.5(b). Figure 3.5(c) also shows that this response consists of more than one independent frequency. The two-dimensional projection of the phase portrait onto the $y_1 - y_2$ plane, presented in figure 3.5(d), shows many closed curves that indicate a high-order periodic response. The Poincaré section in figure 3.5(e) shows finite number of points confirming a period-6 response. However, the response of the system is qualitatively very different when considering nonzero initial conditions ($i.e., y_2 = 0.1, y_2 = 0.2, y_2 = 0.3$) as shown in Figs. 3.5(f)- 3.5(t). For the initial conditions ($y_1 = 0.0, y_2 = 0.1$), the response of the system is also damped as shown in figure 3.5(f). However, the steady-state response, as plotted in figure 3.5(g), shows that the response of the system is complex. We observe small modulated amplitudes, however these modulations are quite different in their responses. The power spectrum, as plotted in figure 3.5(h), shows multiple peaks. The two-dimensional projection of the phase portrait onto the $y_1 - y_2$ plane presented in figure 3.5(i) shows characteristics that indicate quasiperiodic or chaotic responses. This is because the trajectories of quasiperiodic and chaotic responses are not close on themselves and consequently time histories, power spectrum, and phase portraits are not useful to determine the exact response of the system. Therefore, we plot the respective Poincaré section to determine the exact response of the system, as shown in figure 3.5(j). It follows from this plot that there are neither finite number of points nor infinitely many points falling on a closed curve, confirming the chaotic response. Qualitatively, the same behavior is obtained for the initial conditions $y_2 = 0.2$, and $y_2 = 0.3$, as can be seen from the time history, power spectrum, phase portrait, and the Poincaré section presented in Figs. 3.5(k)- 3.5(t).

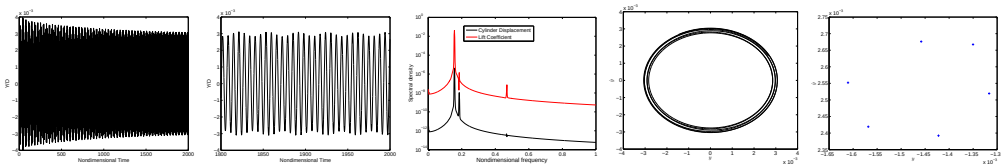

(a) TL displ. (b) SS displ. (c) Spectral density (d) Phase portrait (e) Poincaré map

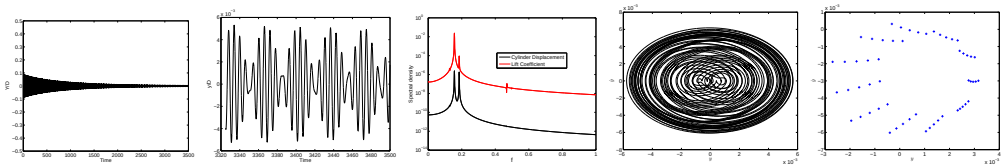

(f) TL displ. (g) SS displ. (h) Spectral density (i) Phase portrait (j) Poincaré map

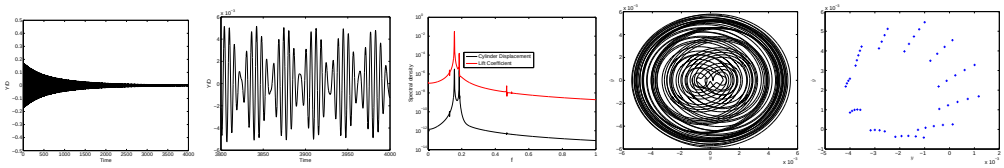

(k) TL displ. (l) SS displ. (m) Spectral density (n) Phase portrait (o) Poincaré map

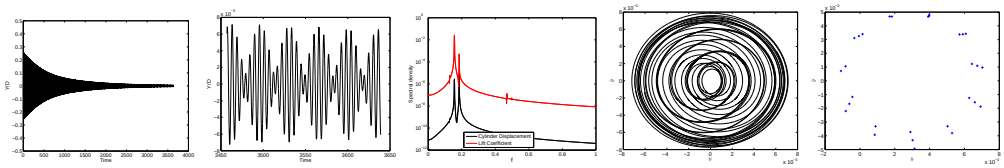

(p) TL displ. (q) SS displ. (r) Spectral density (s) Phase portrait (t) Poincaré map

Figure 3.5: Response of the cylinder when Re=96 (a,b,c,d,e)- $\dot{y} = 0.0$, (f,g,h,i,j)- $\dot{y} = 0.1$, (k,l,m,n,o)- $\dot{y} = 0.2$, (p,q,r,s,t)- $\dot{y} = 0.3$ (TL-total length, SS-steady state).

The same low-amplitude modulated response was observed for different Reynolds number under different initial conditions till Re = 102. Incrementing the Reynolds number to (Re = 102), different responses were observed for the considered sets of initial conditions, as shown in the plotted curves of figure 3.6. For the zero initial conditions (i.e., $y_1 = 0.0, y_2 = 0.0$), we observe a modulated response of the cylinder, as shown in figure 3.6(b). Figure 3.6(c) also reveals that both the lift coefficient and cylinder motion show a band of frequencies around the vortex-shedding frequency. The two-dimensional projection of the phase portrait onto the $y_1 - y_2$ plane presented in figure 3.6(d) shows finite number of closed orbits that indicate a more than one periodic response. The Poincaré section in figure 3.6(c) shows twelve points falling on a closed curve, indicating that the response is twelve-period. For the initial conditions ($y_1 = 0.0, y_2 = 0.1$), we observe a different response of the cylinder. The time history of the cylinder's response shows a high-amplitude modulated response, as shown in figure 3.6(g). The power spectra of the lift coefficient and the oscillation amplitude of the cylinder, as presented in figure 3.6(h), show that there is a band of frequencies. From this plot, we can argue that the system is close to the bifurcation but the system's nonlinearities are able to suppress the bifurcation phenomenon. We can conclude here that the system might need more initial energy to attain the bifurcation. The phase portrait show a band of closed orbits as shown in figure 3.6(i) and the Poincaré section show an infinitely many points following on a closed curve, as shown in figure 3.6(j), indicating a quasiperiodic response.

Next, changing the initial conditions to ($y_1 = 0.0, y_2 = 0.2$), the response of the coupled system is quite different. The response of the cylinder grows to reach a limit cycle, as shown in figure 3.6(l). The power spectra of the displacement of the cylinder and the lift coefficient exhibit a sharp peak at 0.1745, (*i.e.*, the cylinder natural frequency), and smaller peaks at its third and fifth harmonics. Furthermore, we also note that the system oscillates with the cylinder natural frequency deviating from the vortex shedding frequency. The two-dimensional projection of the phase portrait in figure 3.6(n) shows a single closed curve, indicating its period-1 response. The Poincaré section in figure 3.6(o) consists of a single point, further confirming the period-1 response of the coupled system. The same period-1 response was obtained for the initial conditions $y_1 = 0.0, y_2 = 0.3$, as shown from the time history, power spectrum, phase portrait, and Poincaré section presented in Figs. 3.6(q),

3.6(r), 3.6(s), 3.6(t), respectively.

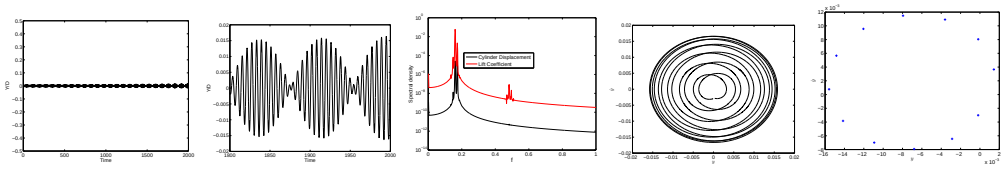

(a) TL displ. (b) SS displ. (c) Spectral density (d) Phase portrait (e) Poincaré map

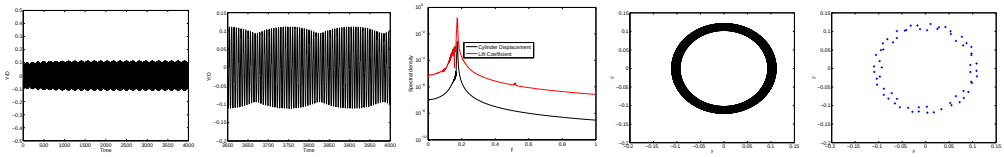

(f) TL displ. (g) SS displ. (h) Spectral density (i) Phase portrait (j) Poincaré map

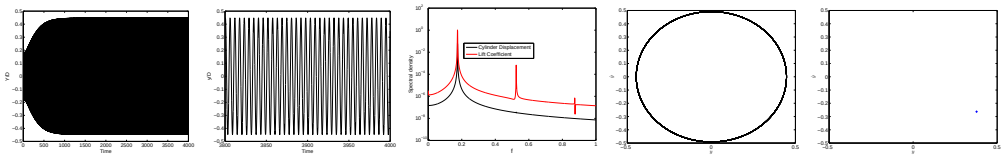

(k) TL displ. (l) SS displ. (m) Spectral density (n) Phase portrait (o) Poincaré map

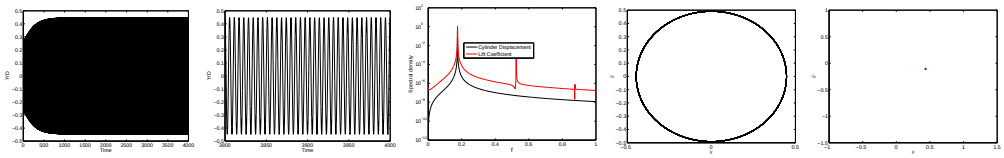

(p) TL displ. (q) SS displ. (r) Spectral density (s) Phase portrait (t) Poincaré map

Figure 3.6: Response of the cylinder when Re=102 (a,b,c,d,e)- $\dot{y} = 0.0$, (f,g,h,i,j)- $\dot{y} = 0.1$, (k,l,m,n,o)- $\dot{y} = 0.2$, (p,q,r,s,t)- $\dot{y} = 0.3$ (TL-total length, SS-steady state).

Next, we consider the response of the system when Re = 106 under different initial conditions. We can see from the time histories for all considered initial conditions, that response of the cylinder grows to reach a stable limit cycle, as shown in Figs. 3.7(b), 3.7(g), 3.7(g), and 3.7(q). The power spectra of the response of the cylinder and that of the fluid show that the system resonates with the same frequency (i.e., the cylinder natural frequency), as shown in Figs. 3.7(c), 3.7(h), 3.7(h), and 3.7(r). Furthermore, the phase portarits show a single closed curve and the associated Poincaré sections, presented in figure 3.7 consist of a single point, confirming the period-1 response of the coupled system. Qualitatively, the same period-1 response of the system is observed till Re = 114 under all different initial conditions.

The response of the cylinder at Re = 116 for different initial conditions is shown in the plotted curves of figure 3.8. We can see from the time history of the cylinder displacement, that at this flow condition the system possess more than one solution, depending on the initial input energy. For the trivial condition, the cylinder oscillates with low amplitude as shown in figure 3.8(b). The power spectra of the cylinder displacement and the lift coefficient have a peak at 0.1636 and smaller peak at 0.4921. The obtained phase portrait and the Poincaré section presented in Figs. 3.8(d) and 3.8(e), respectively, confirming the periodic response of the system. For all other initial conditions (i.e., $y_2 = 0.1, y_2 = 0.2$, and $y_2 = 0.3$), the cylinder oscillates with higher amplitudes as can be noted from the time histories as shown in Figs. 3.8(g), 3.8(l), 3.8(q). The power spectra for these conditions show that the shedding frequency and the cylinder oscillation frequency coincides. Hence, we can say that the response is period-1 and the cylinder motion controls the flow pattern and vortices are shed with the cylinder natural frequency. The two-dimensional projection of the phase portrait for all the conditions as shown in Figs. 3.8(d), 3.8(i), 3.8(n), 3.8(s) shows a single closed curve exhibiting its period-1 behavior. The Poincaré sections presented in Figs. 3.8(e), 3.8(j), 3.8(o), 3.8(t) consist of a single point, confirming the period-1 response of the coupled system.

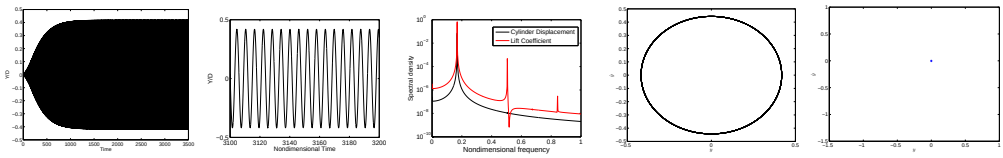

(a) TL displ. (b) SS displ. (c) Spectral density (d) Phase portrait (e) Poincaré map

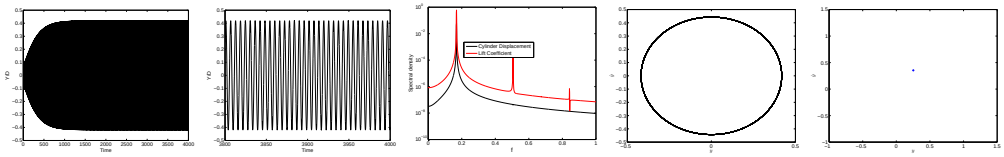

(f) TL displ. (g) SS displ. (h) Spectral density (i) Phase portrait (j) Poincaré map

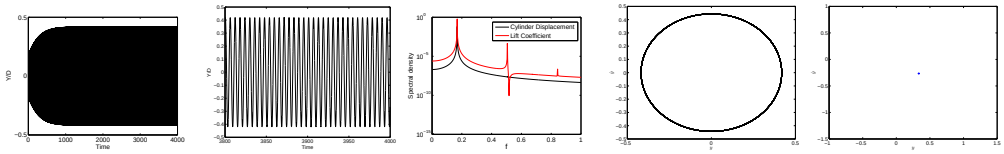

(k) TL displ. (l) SS displ. (m) Spectral density (n) Phase portrait (o) Poincaré map

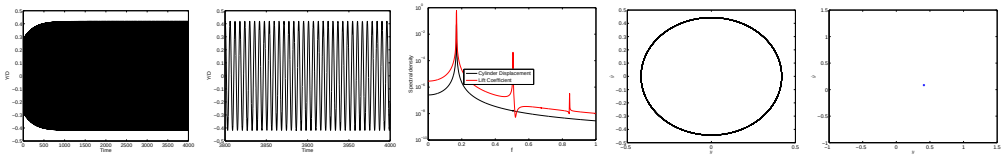

(p) TL displ. (q) SS displ. (r) Spectral density (s) Phase portrait (t) Poincaré map

Figure 3.7: Response of the cylinder when Re=106 (a,b,c,d,e)- $\dot{y} = 0.0$, (f,g,h,i,j)- $\dot{y} = 0.1$, (k,l,m,n,o)- $\dot{y} = 0.2$, (p,q,r,s,t)- $\dot{y} = 0.3$ (TL-total length, SS-steady state).

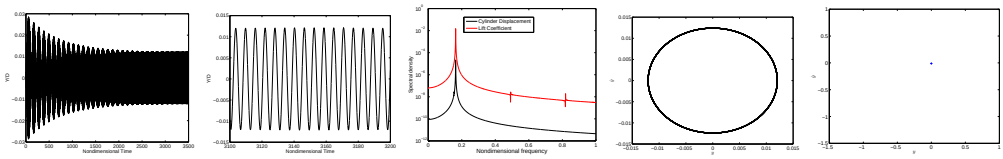

(a) TL displ. (b) SS displ. (c) Spectral density (d) Phase portrait (e) Poincaré map

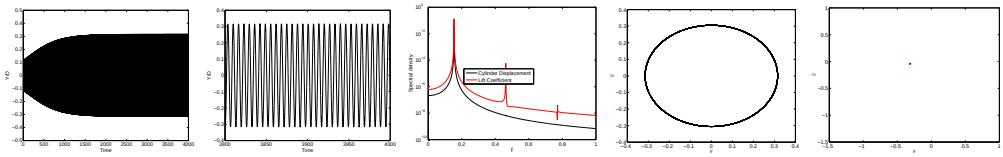

(f) TL displ. (g) SS displ. (h) Spectral density (i) Phase portrait (j) Poincaré map

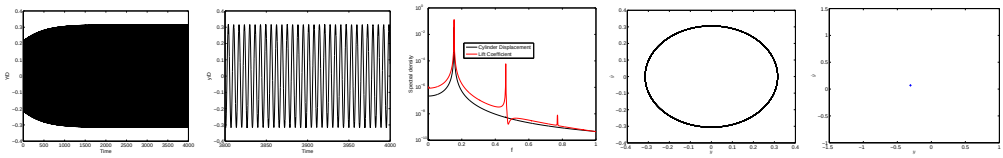

(k) TL displ. (l) SS displ. (m) Spectral density (n) Phase portrait (o) Poincaré map

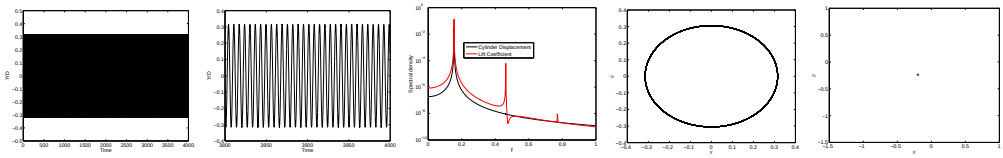

(p) TL displ. (q) SS displ. (r) Spectral density (s) Phase portrait (t) Poincaré map

Figure 3.8: Response of the cylinder when Re=116 (a,b,c,d,e)- $\dot{y} = 0.0$, (f,g,h,i,j)- $\dot{y} = 0.1$, (k,l,m,n,o)- $\dot{y} = 0.2$, (p,q,r,s,t)- $\dot{y} = 0.3$ (TL-total length, SS-steady state).

For Reynolds number equal to Re = 120, different responses were observed under different initial conditions as shown in figure 3.9. For the trivial initial conditions ($y_1 = 0.0, y_2 = 0.0$), we observe a low-amplitude response of the cylinder as shown in figure 3.9(b). The power spectra of both the lift coefficient and cylinder motion show a band of frequencies around the vortex-shedding frequency, as shown in figure 3.9(c). The two-dimensional projection of the phase portrait onto the $y_1 - y_2$ plane presented in figure 3.9(d) shows multiple closed curves, indicating high-order periodic response. However, the Poincaré section in figure 3.9(c) shows multiple points falling on a closed curve, confirming quasiperiodic response of the system.

For the initial conditions ($y_1 = 0.0, y_2 = 0.1$), we observe a completely different response of the cylinder. The time trace of the motion of the cylinder shows a large-amplitude oscillations as shown in figure 3.9(g). The power spectra of the lift coefficient and the oscillation amplitude of the cylinder, as presented in figure3.9(h), show a single sharp peak, indicating that both vortex shedding frequency and the cylinder oscillation frequency coincide at a common frequency. The phase portrait as shown in figure 3.9(i) shows a single closed curve and the Poincaré section presented in figure 3.9(j), has a single point, indicating a period-1 response of the system. Next, changing the initial condition to ($y_1 = 0.0, y_2 = 0.2$), the response of the coupled system is qualitatively same as we observed for the initial conditions $y_2 = 0.1$. The response of the cylinder grows to reach a limit cycle, as shown in figure 3.9(l). The power spectra of the displacement of the cylinder and the lift coefficient exhibit a sharp peak at 0.1545 and smaller peaks at its third and fifth harmonics. Furthermore, the system oscillates with the same frequency (*i.e.*, the cylinder natural frequency). The two-dimensional projection of the phase portrait in figure 3.9(n) shows a single closed curve, confirming its period-1 behavior. The Poincaré section in figure 3.9(o) consists of a single point, confirming the period-1 nature of the response of the coupled system. The same period-1 response was obtained for the initial conditions $y_1 = 0.0, y_2 = 0.3$, as shown from the time history, power spectrum, phase portrait, and Poincaré section presented in Figs. 3.9(q), 3.9(r), 3.9(s), and 3.9(t), respectively.

Next, we consider the response of the system at Re = 130 for different initial conditions, as shown in Figs. 3.10. For all considered initial conditions, we see that the response of the system damps out and reaching to low-amplitude responses, as shown in

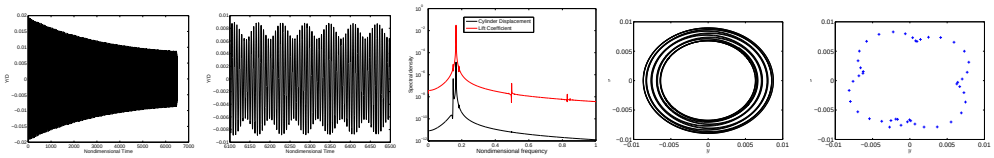

(a) TL displ. (b) SS displ. (c) Spectral density (d) Phase portrait (e) Poincaré map

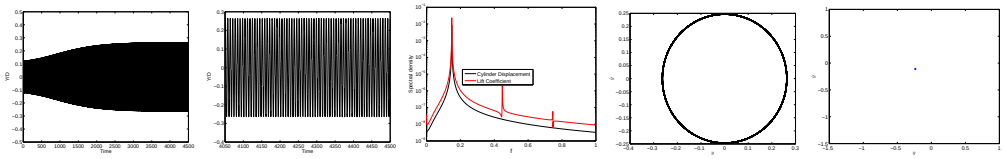

(f) TL displ. (g) SS displ. (h) Spectral density (i) Phase portrait (j) Poincaré map

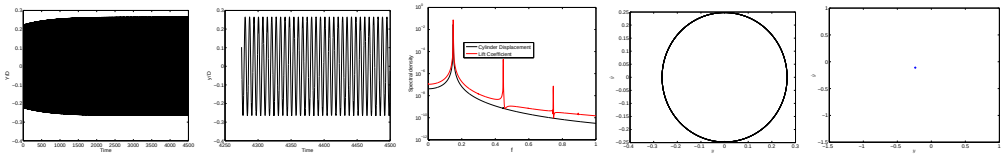

(k) TL displ. (l) SS displ. (m) Spectral density (n) Phase portrait (o) Poincaré map

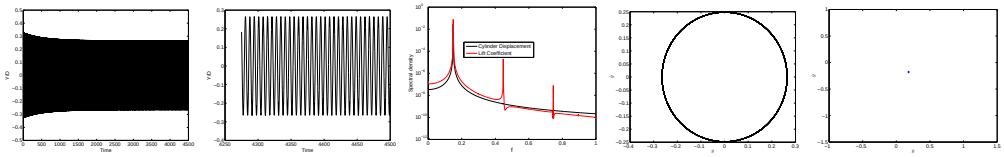

(p) TL displ. (q) SS displ. (r) Spectral density (s) Phase portrait (t) Poincaré map

Figure 3.9: Response of the cylinder when Re=120 (a,b,c,d,e)- $\dot{y} = 0.0$, (f,g,h,i,j)- $\dot{y} = 0.1$, (k,l,m,n,o)- $\dot{y} = 0.2$, (p,q,r,s,t)- $\dot{y} = 0.3$ (TL-total length, SS-steady state).

Figs. 3.10(a), 3.10(f), 3.10(k), and 3.10(p). This response is similar to the one we observed in the pre-synchronization regime for Re = 96. However, the cylinder oscillates with much higher-amplitude as shown in Figs. 3.10(b), 3.10(g), 3.10(l), and 3.10(q). The power spectra for all initial conditions show that these responses consist of more than one independent frequency. For higher initial conditions, the lift coefficient and the motion of the cylinder show a band of frequencies as shown in Figs. 3.10(c), 3.10(h), 3.10(m), 3.10(r). The two-dimensional projection of the phase portraits onto the $y_1 - y_2$ plane presented in Figs. 3.10(d), 3.10(i), 3.10(n), 3.10(s) also show infinite closed curves that indicate a non-periodic behavior. The Poincaré section in Figs. 3.10(e), 3.10(j), 3.10(o), 3.10(t) also show infinite number of points indicating that the response of the system is chaotic.

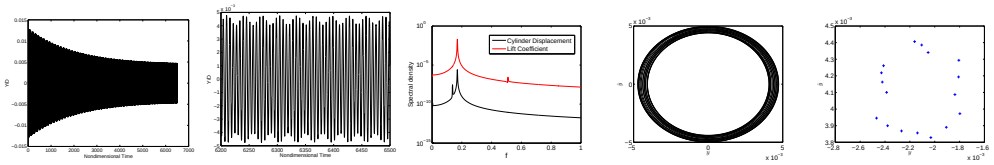

(a) TL displ. (b) SS displ. (c) Spectral density (d) Phase portrait (e) Poincaré map

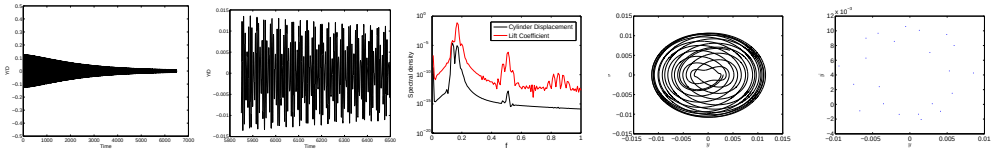

(f) TL displ. (g) SS displ. (h) Spectral density (i) Phase portrait (j) Poincaré map

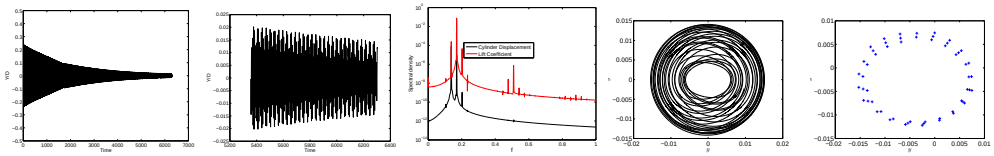

(k) TL displ. (l) SS displ. (m) Spectral density (n) Phase portrait (o) Poincaré map

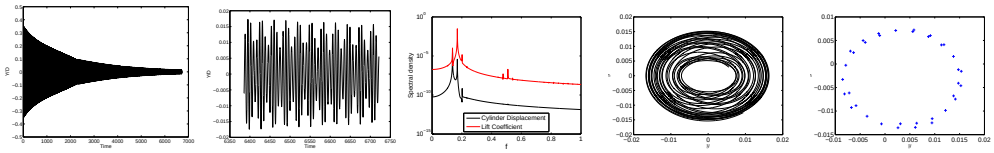

(p) TL displ. (q) SS displ. (r) Spectral density (s) Phase portrait (t) Poincaré map

Figure 3.10: Response of the cylinder when Re=130 (a,b,c,d,e)- $\dot{y} = 0.0$, (f,g,h,i,j)- $\dot{y} = 0.1$, (k,l,m,n,o)- $\dot{y} = 0.2$, (p,q,r,s,t)- $\dot{y} = 0.3$ (TL-total length, SS-steady state).

3.4 Conclusions

We have investigated the effect of different initial conditions around the bifurcation point. We found an unstable region at both ends of the synchronization regime depending on the initial input energy. We also characterized the system response using modern methods of nonlinear dynamics including time histories, power spectra, phase portraits, and Poincaré sections for different sets of initial conditions and Reynolds numbers. We observed periodic response within the synchronization regime. However outside the synchronization regime, the response was complex and we observed period-n (where $n > 1$), quasiperiodic and chaotic responses.

Chapter 4

Linear and Nonlinear Active Feedback Controls for Vortex-Induced Vibrations of Circular Cylinders

We consider the problem of suppressing the oscillations of an elastically-mounted rigid cylinder undergoing vortex-induced vibrations by linear and nonlinear active velocity feedback controllers. Each controller relies on an actuator, which imparts an opposing force to the cylinder's motion, thereby reducing its high-amplitude oscillations. The results show that the choice of the active feedback controller depends on the allowable controlled amplitude of the cylinder. It is found that a cubic velocity feedback controller is more efficient than its linear velocity counterpart when very small controlled amplitudes are desired.

4.1 Introduction

Reduction of the high oscillation amplitudes that are induced by VIV is desired for enhancing the structures safety and increasing their lifetime. This can be achieved by reducing the strength of the generated vortices and/or controlling the motion of the cylinder in an appro-

priate manner. Active flow control mechanisms, such as suboptimal flow blowing and suction (24) or acoustic feedback (21; 26; 27), have been proposed to control vortex-induced vibrations. Akhtar and Nayfeh (24) observed a suppression of the fluctuating forces and obtained more than 40% reduction in the mean drag coefficient using a couple of suction actuators on a stationary cylinder. Blevins (21) experimentally observed that sound waves can affect vortex shedding. Particularly, the introduction of sound waves with frequencies close to the natural vortex shedding frequency can alter the shedding frequency and force it to follow the imposed sound frequency. Ffowcs et al. (26) used sound as an active controller to alter the shedding process. The control loop processed signals from hot-wires placed in the cylinder wake and fed them back to the flow using a loudspeaker in a way that affects the shedding process. They observed a reduction in the velocity fluctuations by more than 30 db. They also observed that the phase of the control signal is an important factor in suppressing the VIV because a phase reversal of the signal could further amplify the oscillation amplitudes. Huang (27) locally introduced sound waves into the flow to influence the shear layer on one side of the cylinder. Suppression of the vortex shedding was observed by the destructive interference of the two shear layers.

The control mechanisms discussed above aim at suppressing or delaying the vortex shedding mechanisms. Another approach for VIV suppression is to directly control the cylinder motion using active feedback controllers. These controllers make use of an actuator signal, which imparts an opposing force to the cylinder motion, thereby reducing the cylinder high-amplitude oscillations. Baz and Ro (25) implemented a velocity feedback controller to dampen vortex-induced vibrations of a circular cylinder. They used a permanent magnetic d.c linear actuator and a stator. The actuator was placed inside the cylinder and the stator was anchored to the wall of the wind tunnel. An accelerometer was used to measure the cylinder acceleration. The signal from this accelerometer was integrated to yield the cylinder velocity. This signal was amplified and used to drive the actuator in such a way to impart a force that opposes the oscillation velocity of the cylinder. They were able to obtain more than an 80% reduction in the amplitude of the oscillations in the synchronization regime. Govardhan and Williamson (56) implemented a mechanical damper that takes the velocity of the cylinder and feeds it, after amplification, to the cylinder through a spring in such a

way that it imparts a force in phase with the cylinder velocity. Their results show that the peak amplitude of the vibration is significantly affected by the mass-damping parameter (α), which is directly proportional to the damping ratio.

In this chapter, we consider the option of using active linear and nonlinear velocity feedback controllers to suppress vortex-induced vibrations. To assess their effectiveness, we compare their performance and required power levels to suppress the motion of the cylinder. Particularly, we aim to determine the most effective control law that requires minimum power to achieve any desired controlled amplitude.

4.2 Representation of the Active Feedback Controllers

4.2.1 Linear Controller

The linear controller imparts a force that is proportional to the velocity of the cylinder. The governing equation of an elastically-mounted rigid circular cylinder subjected to external fluid forces with an active linear controller is then expressed as

$$M\ddot{Y} + C\dot{Y} + KY = F_Y(t) - K_c\dot{Y}, \tag{4.1}$$

where M is the mass of the cylinder per unit length; C and K are the structural damping and stiffness, respectively; $F_Y(t)$ characterizes the time-dependent external force exerted by the fluid flow on the cylinder; and $K_c\dot{Y}$ is the linear control force with K_c being a positive constant.

Using the diameter of the cylinder D and the incoming free-stream velocity U_∞ as length and velocity scales, respectively, we rewrite equation (4.1) in nondimensional form as

$$\ddot{Y}^* + \left(\frac{\beta}{U_r}\right)\dot{Y}^* + \left(\frac{2\pi}{U_r}\right)^2 Y^* = \frac{2}{\pi m^*}C_L, \tag{4.2}$$

where $Y^* = \frac{Y}{D}$ is the nondimensional transverse cylinder displacement, $U_r = \frac{U_\infty}{f_n D}$ is the reduced velocity, $\beta = \left(4\pi\zeta + \frac{K_c}{Mf_n}\right)$ is the controlled damping term, f_n is the natural frequency of the cylinder, $\zeta = \frac{C}{C_{crit}} = \frac{C}{2\sqrt{KM}}$ is the structural damping ratio, $m^* = \frac{M}{M_f}$ is the mass

ratio, and $M_f = \frac{1}{4}\pi\rho D^2$ represents the fluid mass per unit length replaced by the cylinder. Equation (4.2) can be equivalently written as a system of two coupled first-order ordinary differential equations; that is,

$$\dot{y_1} = y_2, \tag{4.3}$$

$$\dot{y_2} = -\left(\frac{2\pi}{U_r}\right)^2 y_1 - \frac{\beta}{U_r} y_2 + \frac{2}{\pi m^*} C_L, \tag{4.4}$$

where $y_1 = Y^*$ and $y_2 = \dot{Y}^*$.

4.2.2 Cubic Controller

The nonlinear controller imparts a force proportional to the cubic velocity of the cylinder. The governing equation of an elastically-mounted rigid circular cylinder subjected to external fluid forces with a cubic velocity feedback controller is then expressed as

$$M\ddot{Y} + C\dot{Y} + KY = F_Y(t) - G\dot{Y}^3, \tag{4.5}$$

where $G\dot{Y}^3$ is the nonlinear control law and G is a positive constant. In nondimensional form, equation (4.5) is written as

$$\ddot{Y}^* + \left(\frac{4\pi\zeta}{U_r}\right)\dot{Y}^* + \left(\frac{2\pi}{U_r}\right)^2 Y^* + \gamma U_r \dot{Y}^{*3} = \frac{2}{\pi m^*} C_L, \tag{4.6}$$

where $\gamma = \frac{G}{(\frac{M}{f_n D^2})}$. Equation (4.6) can be equivalently written as a system of two coupled first-order ordinary differential equations as

$$\dot{y_1} = y_2, \tag{4.7}$$

$$\dot{y_2} = -\left(\frac{2\pi}{U_r}\right)^2 y_1 - \frac{4\pi\zeta}{U_r} y_2 - \alpha U_r y_2^3 + \frac{2}{\pi m^*} C_L. \tag{4.8}$$

4.2.3 Coupling Scheme

Equations (2.5) and (2.6), which govern the dynamics of the flow field, and equations (4.1) and (4.5), which govern the dynamics of the cylinder based on the active controllers, are solved in

a coupled manner. For that purpose, we use the Hamming fourth-order predictor-corrector technique (20).

In this technique, the fluid load (output of the CFD code-equation-2.8) is coupled to ODEs (4.3) and (4.4) governing the cylinder's motion with linear controler and equations (4.7) and (4.8) with cubic velocity feedback controller. The predicted state of the cylinder (equation 2.36), based on the fluid load which was computed in the previous time step, is then used in the CFD code to compute the new fluid load (equation-2.8). This new load is then used to compute the new states of the cylinder using the corrector scheme (equation 2.37). To do so, equations (4.3) and (4.4) for linear controler and equations (4.7) and (4.8) for the cubic velocity feedback controller are rewritten as equation (2.9). The equations are then integerated by using the numerical integeration scheme discussed in Section 2.4.

4.3 Results and Discussion

To investigate the performance of the linear and nonlinear active controllers, we performed numerical simulations of the flow in the range $95 \leq \mathrm{Re} \leq 125$, which corresponds to reduced velocities in the range $5.29 \leq U_r \leq 6.96$. We considered a mass ratio $m^* = 149.10$ and a damping ratio $\zeta = 0.0012$. In the performed simulations, the flow developed from rest and the cylinder motion was allowed to start after 1000 time steps, which provided a sufficient time for the steady-state response to be achieved. This response, generated for each of the considered Reynolds numbers, was used as the initial condition at which the controller was implemented. After reaching steady state, the data was collected and the frequencies of vortex shedding f_{vs} and cylinder oscillations f_{co} were determined.

Variations of the root mean square (rms) oscillation amplitudes of the cylinder with the Reynolds number are presented in figure 4.1(a) and figure 4.1(b) for the linear and cubic velocity feedback controls, respectively, using different control gains. We first consider the response of the uncontrolled cylinder (i.e., $K_c = 0$ and $G = 0$) marked in figure 4.1(a) and figure 4.1(b) by the dashed lines. Below $\mathrm{Re} = 104$, the oscillation amplitude remains very low. A significant increase in the amplitude is noted near $\mathrm{Re} = 104$. Under this flow condition, the vortices are shed at a frequency close to the cylinder natural frequency, deviating slightly

from the shedding frequency of the stationary cylinder. This phenomenon is referred to as "synchronization" and Re = 104 is defined as the Reynolds number corresponding to the onset of the vortex-induced vibrations. The synchronization regime extends to Re = 114. Above this Reynolds number, the oscillation amplitude drops to very small values.

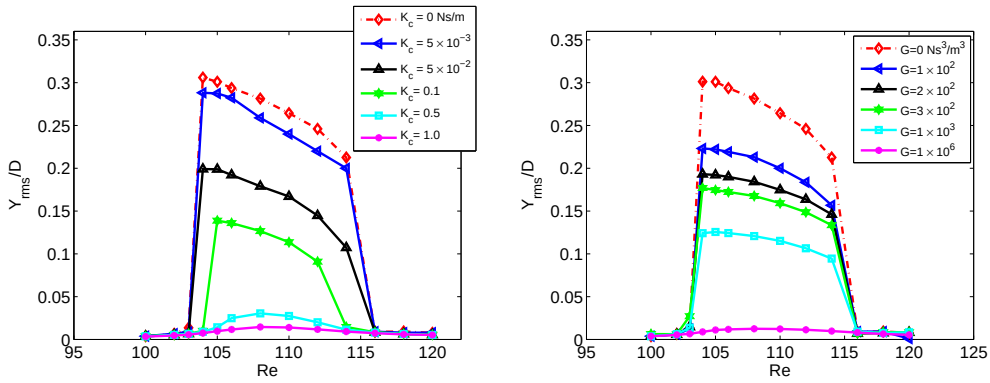

(a) Linear control (b) Nonlinear control

Figure 4.1: Variation of the cylinder displacement (Y_{rms}/D) with the Reynolds number using (a) linear velocity and (b) cubic velocity feedback controllers for different gain values.

Next, we consider the response of the cylinder when implementing the feedback controllers (i.e., $K_c \neq 0$ and $G \neq 0$) over the same range of Reynolds number. We consider different values of the linear and nonlinear gains K_c and G. Comparing the responses of the uncontrolled (dashed line) and controlled motions (solid lines), we conclude from Figs. 4.1(a) and 4.1(b) that both feedback velocity controllers can be used to reduce the oscillation amplitudes of the cylinder. This effect is evident throughout the synchronization regime.

Figure 4.1(a) illustrates the effect of increasing the linear control gain on the cylinder oscillations. The results show that, when Re = 105, an amplitude reduction of 4.5% is obtained when $K_c = 5 \times 10^{-3} Ns/m$. Reductions of 54% and 95% are obtained when $K_c = 0.1 Ns/m$ and $1.0 Ns/m$, respectively. It is interesting, however, to note that the onset of synchronization is delayed and the extent of synchronization is reduced when higher gains are used. A similar qualitative behavior was observed by (56). They observed a collapse of the peak response amplitude for various values of the combined mass-damping parameter

($\alpha = m^*\zeta$). It is interesting to note from figure 8(b) of (56) that, by increasing the mass-damping value (α), the synchronization region contracts in an analogous manner to the one observed in the current simulations. The current simulations show a controlled amplitude $\frac{Y_{max}}{D} = 0.2716$ for $\alpha = 0.4617$. (56) obtained $\frac{Y_{max}}{D} = 0.28$ for a combined mass-damping parameter $\alpha = 0.451$. Increasing the mass-damping parameter by 13.56% from $K_c = 0Ns/m$ to $K_c = 5 \times 10^{-3}Ns/m$ yields an amplitude reduction of 4.5%. Amplitude reductions of 35%, 54%, and 91.5% are, respectively, obtained for mass-damping parameter values of 0.47, 0.76, and 3.09 when Re = 106.

For the cubic velocity feedback controller, a reduced response is also observed in the whole range of synchronization. The effect of the gain G of the nonlinear velocity feedback controller on reducing the peak response amplitude is similar to that of the linear controller. For example, when Re = 105, an amplitude reduction of 26.2% is obtained when the cubic gain $G = 100Ns^3/m^3$. Reductions of 42.36% and 96% are obtained when $G = 300Ns^3/m^3$ and $1.0 \times 10^6 Ns^3/m^3$, respectively, as shown in figure 4.1(b).

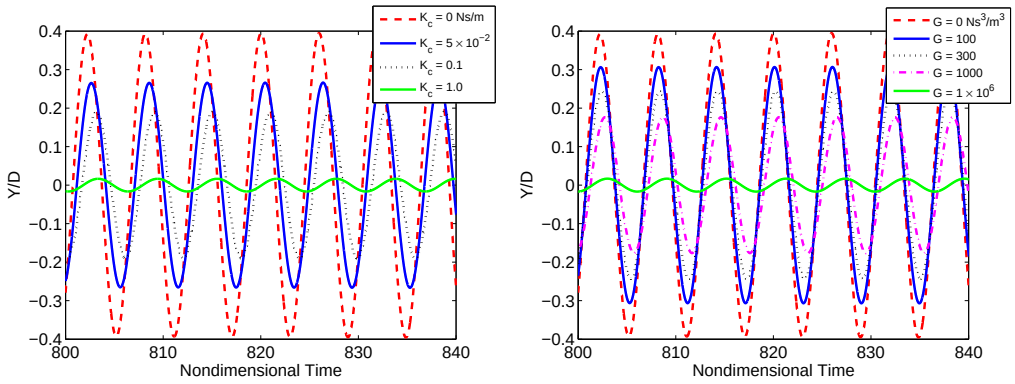

(a) Linear control (b) Nonlinear control

Figure 4.2: Time histories of the cylinder transverse displacement for (a) the linear controller and (b) the nonlinear controller for different gains when Re = 106.

Figure 4.2 shows time histories of the cylinder displacement for different linear and nonlinear control gains. Comparing the time trace of the uncontrolled case (i.e., $K_c = 0$ and $G = 0$) with those of the controlled cases (i.e., $K_c \neq 0$ and $G \neq 0$), we conclude that the

oscillation amplitudes of the cylinder decrease as the gain of either of the two controllers is increased.

4.4 Power Comparison and Optimal Control

To assess the effectiveness of both controllers, we performed a comparison between the power needed to suppress the oscillation amplitude of the cylinder to the same level. Three cases of the two controllers that yield the same level of oscillation amplitude are considered. In Case 1, we compare the results for $K_c = 5 \times 10^{-3} Ns/m$ and $G = 10 Ns^3/m^3$ when Re = 106. The oscillation amplitude of the cylinder is reduced to about $\frac{Y_{max}}{D} \sim 0.4$ using either of the two feedback controllers, as shown in figure 4.3(a). The associated velocity of the cylinder follows very closely that of the displacement for both cases, as shown in figure 4.3(b). Moreover, the lift coefficient presented in figure 4.3(c) oscillates around a zero mean with a peak value of about 1.25. All these time histories show a steady-state periodic behavior and have a dominant frequency, the cylinder natural frequency. The feedback control force is plotted for both of the linear ($\frac{K_c}{M f_n U_r} \dot{Y}^*$) and nonlinear ($\frac{G f_n D^2 U_r}{M} \dot{Y}^{*3}$) controllers in figure 4.3(d). Inspecting this plot, we note that the cubic velocity feedback controller needs more force than the linear one. This is expected because the displacement and velocity amplitudes remain very high. The time series also shows a third harmonic in the nonlinear control force.

In Case 2, we compare the controlled cases for $K_c = 6.5 \times 10^{-2} Ns/m$ and $G = 300 Ns^3/m^3$ when Re = 106. The oscillation amplitude for either of the two controllers is about $\frac{Y_{max}}{D} \sim 0.24$, as shown in figure 4.4(a). Time histories of the velocity, lift coefficient, and control force are shown in Figs. 4.4(b), 4.4(c), and 4.4(d), respectively. These plots show harmonic responses with a dominant frequency, the cylinder natural frequency. Figure. 4.4(d) shows that the cubic velocity feedback force is again higher than the force needed in the case of the linear feedback controller. This is again due to the fact that the displacement and velocity amplitudes remain very large.

In Case 3, we compare the results for $K_c = 1.2 Ns/m$ and $G = 1.5 \times 10^6 Ns^3/m^3$ considering the same Reynolds number (i.e., Re = 106). These gains are needed to obtain near zero oscillation and velocity amplitudes, as shown in figure 4.5(a) and 4.5(b). The lift coefficient,

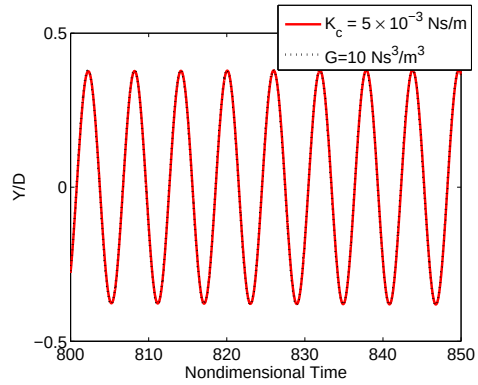

(a) Time History of Displacement

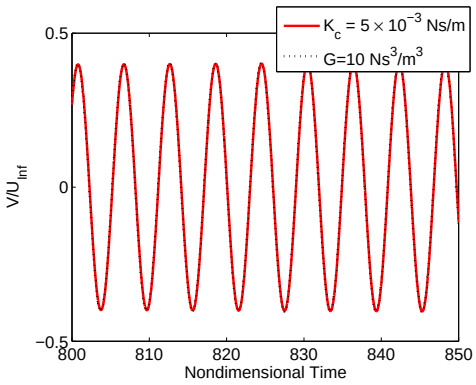

(b) Time History of Velocity

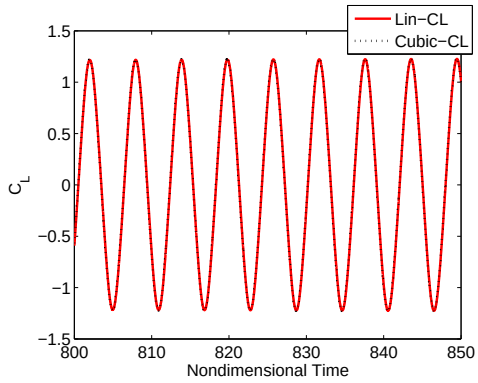

(c) Time History of C_L

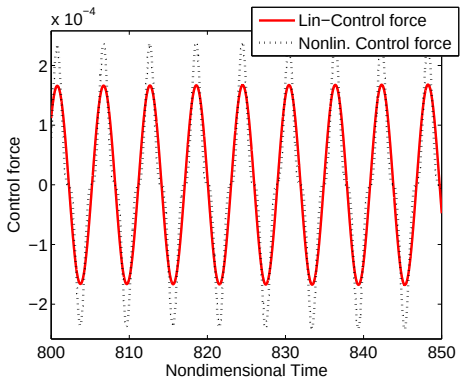

(d) Time History of Control force

Figure 4.3: Time histories of the (a) displacement, (b) velocity, (c) lift coefficient, and (d) control force when $K_c = 5.0 \times 10^{-3} Ns/m$ and $G = 10 Ns^3/m^3$ when Re = 106.

presented in figure 4.5(c), oscillates around a zero mean with a peak value of 0.42. Inspecting figure 4.5(d), we note that the force required for the nonlinear controller has a slightly lower amplitude than that of the linear one. This is due to the fact that the displacement and velocity amplitudes are very low.

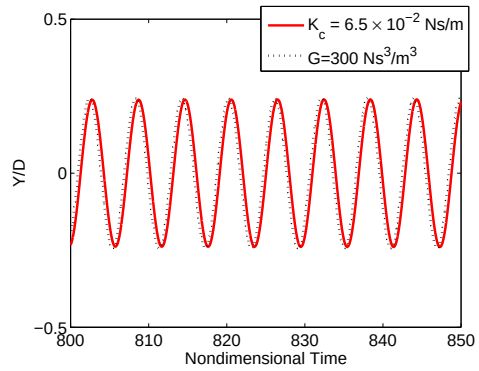

(a) Time History of Displacement

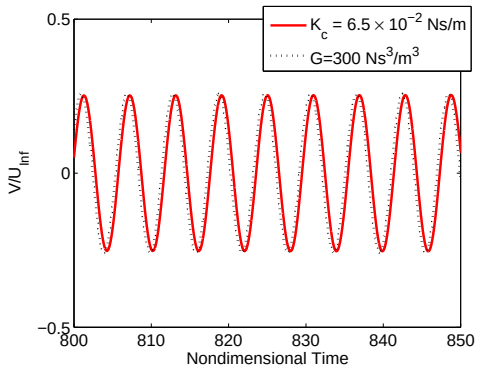

(b) Time History of Velocity

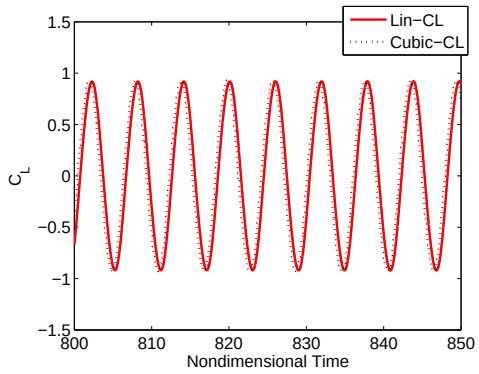

(c) Time History of C_L

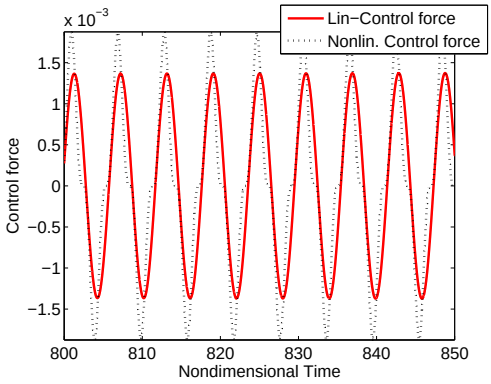

(d) Time History of Control force

Figure 4.4: Time histories of the (a) displacement, (b) velocity, (c) lift coefficient, and (d) control force when $K_c = 6.5 \times 10^{-2} Ns/m$ and $G = 300 Ns^3/m^3$ when Re = 106.

4.4.1 Theoretical Explanations

The linear control force is $F_L = -K_c \dot{Y}$ and the oscillation can be expressed as $Y = DA_1 \cos(\omega_n t + \phi_1) + DA_3 \cos(3\omega_n t + \phi_3)$ where $\omega_n = 2\pi f_n$; f_n is the dimensional natural frequency of the cylinder; and A_{L1} and A_{L3} are, respectively, the amplitudes of first and third harmonics of the nondimensional cylinder displacement. Inspecting figure 4.6, we note that the amplitude of the third harmonic is very small compared to that of the first harmonic. Hence, the cylinder

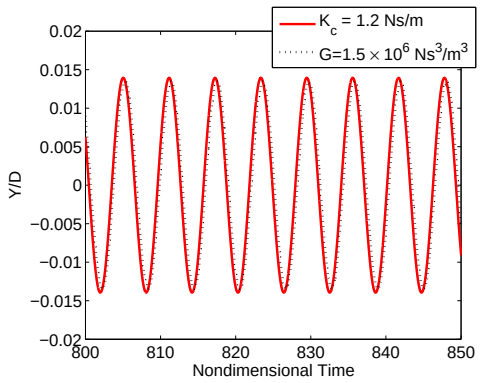

(a) Time History of Displacement

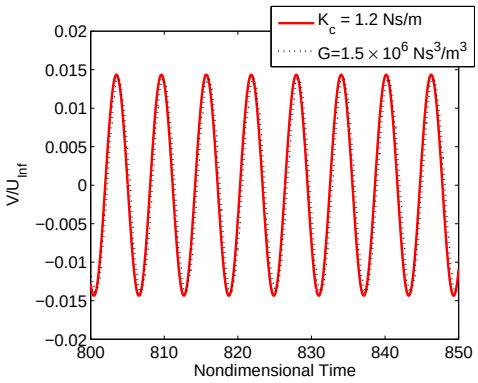

(b) Time History of Velocity

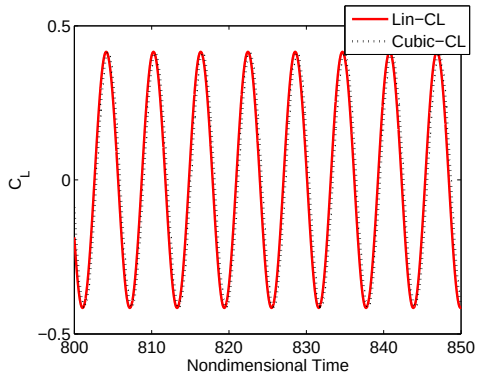

(c) Time History of C_L

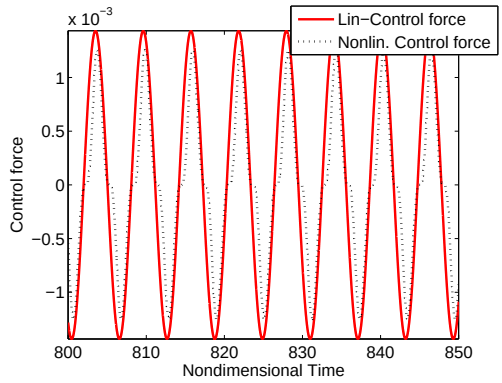

(d) Time History of Control force

Figure 4.5: Time histories of the (a) displacement, (b) velocity, (c) lift coefficient, and (d) control force when $K_c = 1.2Ns/m$ and $G = 1.5 \times 10^6 Ns^3/m^3$ when Re = 106.

displacement can be approximated by $DA_1 \cos(\omega_n t + \phi_1)$. The average power is given by

$$P_{avg} = \lim_{T\to\infty} \frac{1}{T} \int_0^T F(t)\dot{Y}(t)\, dt$$

For the case of linear velocity feedback, this average is equal to

$$P_{L_{avg}} = \frac{1}{2} K_c A_{L1}^2 D^2 \omega_n^2 \tag{4.9}$$

where A_{L1} is the nondimensional oscillation amplitude of the cylinder for the linear velocity feedback controller. In the case of the nonlinear controller, the required force is $-G\dot{Y}^3$. The

average required power is then equal to

$$P_{NL_{avg}} = \frac{3}{8} G A_{NL1}^4 D^4 \omega_n^4 \tag{4.10}$$

where A_{NL1} is the nondimensional oscillation amplitude of the cylinder for the cubic velocity feedback controller. The ratio of the average powers required for the nonlinear and linear controllers is then written as

$$\frac{P_{NL_{avg}}}{P_{L_{avg}}} = \frac{3}{4} \frac{G}{K_c} \frac{A_{NL1}^4}{A_{L1}^2} D^2 \omega_n^2 \tag{4.11}$$

It is clear that the ratio depends strongly on the desired controlled amplitude and the required gains. The ratios of the average power of the considered three cases are presented in Table 4.1. We note that the linear controller is more appropriate if relatively large controlled amplitudes are allowed. However, for cases where very small controlled amplitudes are desired, the nonlinear controller is more efficient. As a matter of fact, the power level needed can be reduced significantly if a nonlinear controller with a relatively large gain is used. This is evident from figure 4.7, where the controlled power for both controllers is plotted as a function of the controlled amplitude.

Table 4.1: Comparison of the power requirements for the linear and nonlinear controllers.

Cases	Amplitudes ($\frac{Y_{max}}{D}$)	Gains	P_{NL}/P_L
1	$A_{NL} \cong A_L \sim 0.4$	$K_c = 5 \times 10^{-3} Ns/m$ and $G = 10 Ns^3/m^3$	1.12
2	$A_{NL} \cong A_L \sim 0.2418$	$K_c = 6.5 \times 10^{-2} Ns/m$ and $G = 300 Ns^3/m^3$	1.04
3	$A_{NL} \cong A_L \sim 0.013$	$K_c = 1.2 Ns/m$ and $G = 1.5 \times 10^6 Ns^3/m^3$	0.84

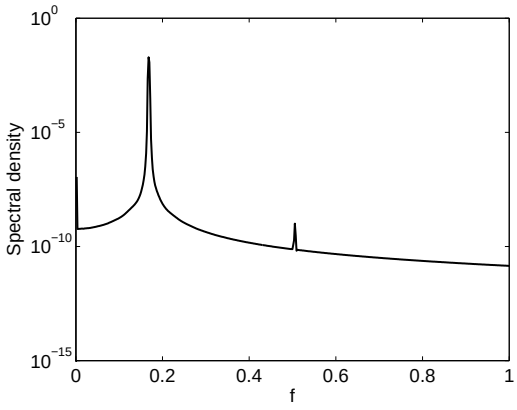

Figure 4.6: Power spectrum of the displacement of a rigid cylinder oscillating in the cross-flow direction when Re = 106 and $G = 300Ns^3/m^3$.

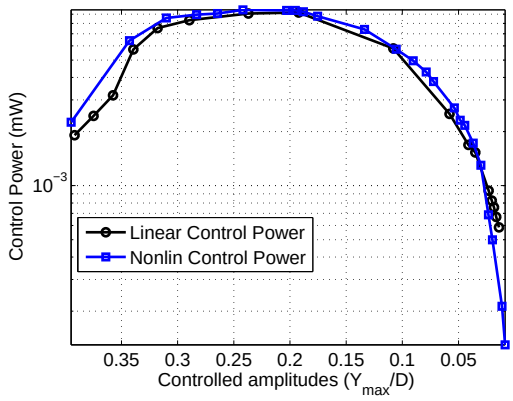

Figure 4.7: Comparison between the linear and nonlinear control powers as a function of the controlled amplitude when Re = 106.

4.5 Conclusions

We investigated the effectiveness of linear and nonlinear velocity feedback controllers to suppress high-amplitude oscillations of an elastically-mounted rigid cylinder. Each controller imparts an opposing force to the cylinder motion, thereby reducing its high-amplitude oscillations. The opposing force, in the case of the linear controller, is proportional to the velocity of the cylinder, while, in the case of the nonlinear controller, it is proportional to the cubic velocity of the cylinder. The results show that both control laws have a significant effect on the response of the cylinder and damp the high-amplitude oscillations of the cylinder in the synchronization regime. A comparison of the performance of the two controllers based on suppressing the oscillations to the same desired amplitude was performed. The results show that, for relatively allowed large controlled amplitudes, the linear velocity feedback controller is more efficient. On the other hand, for very small controlled amplitudes, the cubic velocity feedback controller is more efficient.

Chapter 5

Effect of Nonlinear Energy Sink (NES) on Vortex-Induced Vibrations of a Circular Cylinder

We investigate in detail the possibility of controlling vortex-induced vibrations of a freely oscillating circular cylinder by using a nonlinear energy sink that consists of a secondary system having linear damping and an essential nonlinear cubic stiffness. We vary the sink parameters (mass and damping) and determine their effects on the response of the coupled system. We find multiple stable responses (periodic and quasiperiodic) of the coupled system for different mass ratios and damping coefficient of the sink, depending on the initial conditions. In addition, we find that the oscillation amplitude of the secondary system may be too large and restricts its practical implementation.

5.1 Introduction

Passive controllers are usually desined for a specific oscillation-amplitude/frequency. They may not be effective over a wide range of oscillation amplitudes and may be constrained to a limited frequency range (25; 30). One approach to overcome this limitation is the use of a secondary system having an essential nonlinear stiffness to which vibrations are transferred.

Both experimental (57–61) and numerical (37; 58; 62–65) investigations have shown that secondary systems are able to react efficiently over a broad frequency range. The nonlinear secondary system would make use of energy pumping phenomenon; a one-way irreversible transfer of energy from the primary system to a connected nonlinearizable sytem. This secondary system is usually termed as a nonlinear energy sink (NES). Roberson (62) studied the response of an undamped coupled system consisting of a primary mass having a linear stiffness attached to a secondary mass having an essential nonlinear stiffness. The coupled system was forced by externally applied periodic forces of constant amplitudes and varied excitation frequencies over a limited range near the main frequency. It was found that for the optimum coefficients of both linear and nonlinear springs, the suppression bandwidth is much wider when compared to a linear absorber. Rice and McCraith (66) also studied the behavior of the nonlinear energy sink and determined that the operating frequency is critical in defining the usefulness of the NES. If the operating freqency is close to the critical tuning frequency, a linear absorber is equally advantageous. However, the NES is a better option, in cases where control is needed over a range of operating frequencies.

Gendelman (63) investigated the transition of energy from a linear system that is weakley coupled to a highly nonlinear damped subsystem. An asymmetric system was considered to enable the energy transfer between the system modes. It was observed that the nonlinear energy sink is effective for any external force if the amplitude of linear oscillator is able to activate the highly nonlinear modes. Also, it was found that, for a specific frequency, the nonlinear energy sink can absorb only a certain amount of energy. Jiang et al. (57) experimentally and theoretically studied the dynamics of an NES weakley coupled to a linaer structure that is influenced by harmonic forcing. They found that due to the nonlinearity, the NES can vibrate with any mode of the primary system. They observed periodic responses of both the primary mass and the NES. Lee at al. (67; 68) investigated the dynamics of an ungrounded NES that is strongly coupled to a linear oscillator. They found different periodic orbits for the coupled system.

Gourdon and Lamarque (64) studied the effectiveness of an NES that is loosely coupled to the primary mass. They found that the NES starts attenuating the oscillation amplitude of the primary mass when the primary mass reaches a specific amplitude. They also studied

the energy pumping phenomenon by attaching many nonlinear energy sinks to a primary mass and observed energy pumping phenomenon over a broad frequency range. Because the coupled system has an essential nonlinearity, it will have multi nonlinear normal modes. As such, there is a possibility that the nonlinear attachment will vibrate with the primary system over a range of frequencies. Initially, it will take place between the linear mode of the primary mass and one of the nonlinear normal mode of the NES for a specific energy. As the energy of the primary mass changes, another nonlinear normal mode will interact with the linear mode of the primary mass; thus, still having the desired energy pumping phenomenon. This way the span of frequencies over which energy transfer between the primary mass and the NES increases. Vakakis et al. (58; 65) observed the phenomenon of resonance cascades theoretically and experimentally. They considered many primary masses having a linear stiffness that is weakly attached to the nonlinear energy sink having an essential nonlinearizable cubic stiffness. The system was excited with a force having multifrequency components and found that energy can be transferred from the linear substructures to the NES. When the system is oscillating with high energy, the nonlinear energy sink resonates with the system's high frequency mode and extracts energy from that substructure. As the energy of the substructure decreases due to dissipation, the nonlinear energy sink resonates with the lower energy mode and extracts energy from the second high energy substructure, thus attenuating the oscillation amplitude of the primary masses over a wide range of frequencies.

McFarland et al. (59) experimentally studied the broadband transfer of energy from a damped linear oscillator weakly coupled to a secondary mass having linear damping and nonlinear stiffness of cubic order. They found that the NES starts oscillating after the primary mass reaches a critical oscillation amplitude. Gendelman et al. (69) also observed that to optimize the rate of energy pumping, the system initial conditions should bring the system close to the bifurcation points (i.e, critical oscillation amplitude) as early as possible. Gendelman et al. (60) observed a quasiperiodic behavior both numerically and experimentally when studying the response of an NES that is strongly coupled to the primary mass under external harmonic force. They found that NES ensures better suppression region than the best tuned linear absorber, having the same stiffness and damping parameters. Recently, Tumkur et al. (37; 38) proposed passive control of VIV of a circular cylinder over a broad

frequency range by attaching a NES. Their results show a reduction in the root mean square (rms) of the oscillation amplitude of the cylinder for different NES masses.

However, introducing an essential cubic nonlinearity to a coupled system could lead to multiple stable responses, depending on the initial conditions and the system characteristics and parameters. Malatkar and Nayfeh (70) explored the rich dynamics of the coupled system considered by Jiang et al. (57) by determining its periodic responses and their bifurcations. Not surprisingly, they found a lot of interesting dynamics over a broad frequency range: cyclic-fold, Hopf, symmetry-breaking, and period-doubling bifurcations; phase-locked motions; regions with multiple coexisting solutions; hysteresis; and chaos. Moreover, contrary to the claim made by Jiang et al. (57), they did not find any indication of nonlinear energy pumping or localization of energy in the NES, away from the directly forced linear subsystem, indicating that the NES is not effective for controlling the vibrations of forced linear structures. In a rebuttal, Vakakis and Bergman (71) disputed the conclusions of Malatkar and Nayfeh (70) and stated that, in their view, the existence or not of forced localization and steady-state energy pumping cannot be judged solely by simple comparisons, such as those made in figure 18 of Malatkar and Nayfeh (70) and, in fact, they (57) executed a careful program involving theoretical, computational, and experimental studies to prove that, indeed, steady-state energy pumping occurs in certain frequency ranges of the coupled system. In answer to Vakakis and Bergman, Malatkar and Nayfeh (72) produced more detailed results showing that the addition of an NES to a forced linear oscillator would not result in nonlinear energy pumping or localization of the steady-state vibration in the NES and away from the forced linear subsystem and it would result in an increase rather than a decrease in the vibration amplitude of the latter.

Controlling the system's initial conditions, characteristics, and parameters may not be easy in some cases. This is especially true in the case of aeroelastic oscillations or vibrations where gusts and turbulence may influence the flow dynamics and loads instantly in a significant manner. Vortex-induced vibrations of circular cylinders certainly fall in this category. Furthermore, the excitation force results from flow separation, which has a nonlinear aspect that could not be linearized. Consequently, the system nonlinearities could interact in a coupled manner to exhibit multiple solutions. In this work, we investigate in detail the feasibility

of using a nonlinear energy sink to control the vortex-induced vibrations of a freely oscillating circular cylinder. Particularly, we aim to determine the effects of the NES parameters (mass, stiffness, and damping) and initial conditions on the responses of the primary (cylinder) and secondary (NES) subsystems. The focus is on the synchronization region of the VIV where the oscillation amplitudes are relatively high.

5.2 Representation of the Nonlinear Energy Sink

The governing equations of an elastically-mounted rigid circular cylinder coupled with a nonlinear energy sink subjected to external fluid forces are given by

$$(M - M_{nes})\ddot{Y_2} + C\dot{Y_2} + KY_2 + C_{nes}(\dot{Y_2} - \dot{Y_1}) + K_{nes}(Y_2 - Y_1)^3 = F_L, \quad (5.1)$$

$$M_{nes}\ddot{Y_1} + C_{nes}(\dot{Y_1} - \dot{Y_2}) + K_{nes}(Y_1 - Y_2)^3 = 0, \quad (5.2)$$

where Y_2 is the transverse cylinder displacement and Y_1 is the displacement of the nonlinear energy sink, also constrained to be perpendicular to the flow. M is the mass of the primary cylinder per unit length, C and K are used to represent the structural damping and stiffness, respectively. M_{nes}, C_{nes}, and K_{nes} represent the mass, damping, and stiffness of the NES respectively; and F_L is used to represent the time-dependent external force exerted by the fluid flow on the cylinder.

Using the diameter of the cylinder D and the incoming free-stream velocity U_∞ as length and velocity scales, respectively, we rewrite equations (5.1, 5.2) in a nondimensional form as

$$(1-\mu)\ddot{Y_2}^* + \tilde{C}\dot{Y_2}^* + \tilde{K}Y_2^* + \tilde{C}_{nes}(\dot{Y_2}^* - \dot{Y_1}^*) + \tilde{K}_{nes}(Y_2^* - Y_1^*)^3 = \frac{2}{\pi m^*}C_L, \quad (5.3)$$

$$\mu\ddot{Y_1}^* + \tilde{C}_{nes}(\dot{Y_1}^* - \dot{Y_2}^*) + \tilde{K}_{nes}(Y_1^* - Y_2^*)^3 = 0, \quad (5.4)$$

where $Y_2{}^* = \frac{Y_2}{D}$ and $Y_1{}^* = \frac{Y_1}{D}$ are, respectively, the nondimensional transverse cylinder's and NES displacements, $\mu = \left(\frac{M_{nes}}{M}\right)$ is the mass ratio. $\tilde{C} = \left(\frac{4\pi\zeta}{U_r}\right), \tilde{K} = \left(\frac{2\pi}{U_r}\right)^2$ are the nondimensional damping and stiffness of the primary mass respectively. where $\zeta = \frac{C}{C_{crit}} = \frac{C}{2\sqrt{KM}}$ is the structural damping ratio, $U_r = \frac{U_\infty}{f_n D}$ is the reduced velocity and f_n is the

natural frequency of the cylinder. $\tilde{C}_{nes} = \left(\frac{C_{nes}}{Mf_nU_r}\right), \tilde{K}_{nes} = \left(\frac{KnesD^2}{Mf_n^2U_r^2}\right)$ are, respectively, the nondimensional damping and stiffness of the NES. $m^* = \frac{M}{M_f}$ is the ratio of the primary structural mass to the fluid mass, and $M_f = \frac{1}{4}\pi\rho D^2$ represents the fluid mass per unit length replaced by the cylinder. C_L is the lift coefficient determined from the numerical simulations of eqn. 2.8. Equations (5.3) and (5.4) can be equivalently written as a system of four coupled first-order ordinary differential equations; that is,

$$\dot{y_1} = y_2, \tag{5.5}$$

$$\dot{y_2} = \frac{1}{1-\mu}\left[-\tilde{K}y_1 - \tilde{C}y_2 - \tilde{K}_{nes}(y_1 - y_3)^3 - \tilde{C}_{nes}(y_2 - y_4) + \frac{2}{\pi m^*}C_L\right], \tag{5.6}$$

$$\dot{y_3} = y_4, \tag{5.7}$$

$$\dot{y_4} = \frac{1}{\mu}\left[-\tilde{K}_{nes}(y_3 - y_1)^3 - \tilde{C}_{nes}(y_4 - y_2)\right], \tag{5.8}$$

where $y_1 = {Y_2}^*$, $y_2 = \dot{{Y_2}}^*$, $y_3 = {Y_1}^*$ and $y_4 = \dot{{Y_1}}^*$.

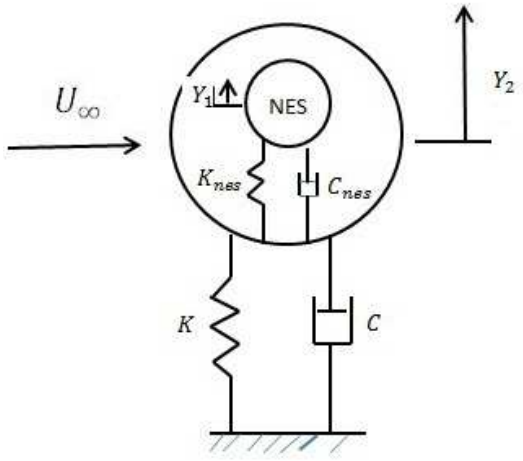

Figure 5.1: Schematic diagram of the primary cylinder coupled with NES.

5.2.1 Coupling Scheme

Equations (2.5) and (2.6), which govern the dynamics of the flow field, and equations (5.3) and (5.4), which govern the dynamics of the cylinder and NES are solved in a coupled manner.

The same procedure is used i.e., the fluid load (output of the CFD code-equation-2.8) is coupled to ODEs (equation-5.5-5.8) governing the cylinder's and NES motion. The predicted state of the cylinder and NES (equation 2.36), based on the fluid load which was computed in the previous time step, is then used in the CFD code to compute the new fluid load (equation-2.8). This new load is then used to compute the new states of the cylinder and voltage using the corrector scheme (equation 2.37). To do so, equations (5.5-5.8), are rewritten as equation (2.9) and then integerated by using the numerical integeration scheme discussed in Section 2.4.

5.3 Results and Discussion

To investigate the performance of the nonlinear energy sink for the purpose of controlling vortex-induced vibrations, we performed numerical simulations of the flow at Re = 106. This Reynolds number lies in the synchronization regime for the considered parameters of the cylinder (1; 28). The cylinder is assumed to have linear stiffness and viscosity and the attachment is connected to a nonlinear spring and a damper to dissipate the extracted energy from the cylinder. A schematic of the system under consideration is presented in figure 5.1. For the cylinder, we considered the same mass ratio $m^* = \frac{M}{M_f} = 149.10$ and damping ratio $\zeta = 0.0012$ as in the experimental work (1), whereas we varied the mass, stiffness, and damping of the NES and are given for each case.

First, we consider the response of the cylinder without the NES. As the flow passes over a cylinder, vortices are formed in the wake and shed with a specific frequency. At the considered Reynolds number, the frequency of vortex-shedding is extremely close to the natural frequency of the cylinder, which causes the cylinder to oscillate with a high amplitude, as shown in figure 5.2(a). The plot also shows that the transverse cylinder displacement starts to increase monotonically until it reaches a stable limit cycle, as shown in figure 5.2(b). Because of lock-in, both of the wake and cylinder have synchronized frequencies, as shown in figure 5.2(c). The phase-portrait, plotted in figure 5.2(d), confirms that the cylinder undergoes periodic oscillations.

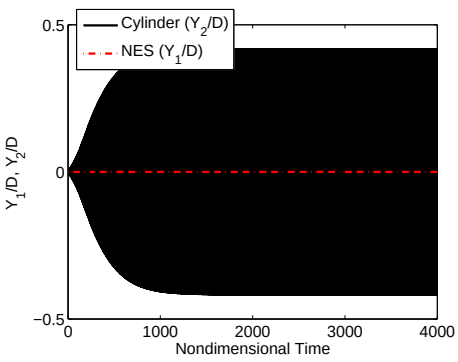

(a) Time history of the cylinder and NES displacement

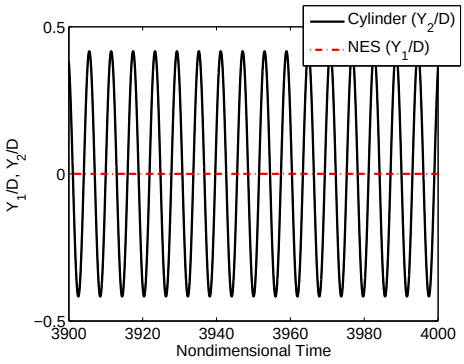

(b) Steady state

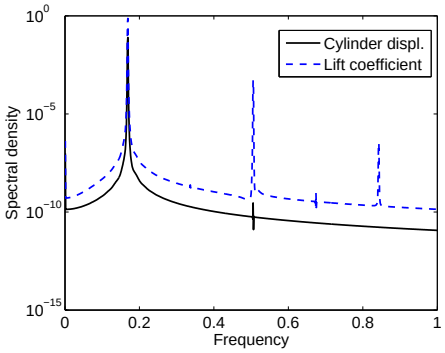

(c) Spectral density

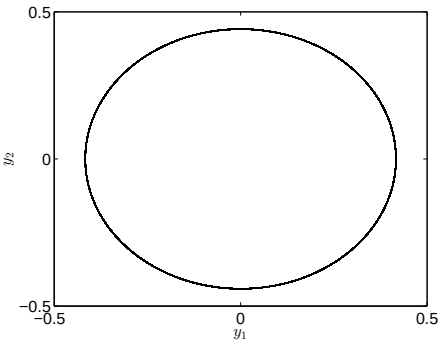

(d) Phase portrait

Figure 5.2: Response of the cylinder without activating the NES in the lock-in region.

5.3.1 Effect of the Ratio of the Masses of the NES and Cylinder

From a practical perspective, it would be desirable to have a small mass ratio; that is, maintain the mass of the NES small relative to the mass of the cylinder. To this end, we examined the effect of this ratio on the ability of the NES to extract the energy of the cylinder oscillations. We did so by keeping all other system parameters constant. The mass ratio was varied over the range $0.01 \leq \mu \leq 0.1$, where $\mu = \frac{M_{nes}}{M}$. The stiffness and damping of the cylinder were set to $\tilde{K} = 1.13404$ and $\tilde{C} = 0.0026$, and those of the NES were set to $\tilde{K}_{nes} = 0.8\tilde{K} = 0.907232$ and $\tilde{C}_{nes} = 0.8\tilde{C} = 0$. In all of the results presented in this subsection, the initial conditions

are trivial.

Figure 5.3(a) shows a zoomed part of the initial response of the coupled system for $\mu = 0.01$. The black solid line shows the response of the cylinder and the red dotted line shows the response of the nonlinear energy sink. This plot shows that the oscillation amplitude of the cylinder slowly increases. When this amplitude reaches $\frac{Y_2}{D} = 0.055$, the energy pumping becomes effective in that the oscillation amplitudes of the NES become larger than those of the cylinder. However, it is clear that, although the energy pumping phenomenon is there, the NES is unable to significantly reduce the amplitude of the cylinder oscillations which remain at about $\frac{Y_2}{D} = 0.35$, as shown in figure5.3(b), in comparison to the uncontrolled value of $\frac{Y_2}{D} = 0.42$ shown in figure5.2(b); a reduction of about 15%. A similar qualitative behavior is observed when the mass ratio, μ, is increased to 0.02. However the critical amplitude at which the amplitude of the NES becomes larger than that of the cylinder is delayed. It takes place when the amplitude of the cylinder oscillations reaches a value near $\frac{Y_2}{D} = 0.089$, as shown in figure5.3(c). Figure 5.3(d) shows the steady-state responses of the coupled system. The amplitude reduction caused by the NES is about 18% for $\mu = 0.02$. However, the amplitude of the NES oscillation is larger than the radius of the cylinder, and hence the NES would impact the cylinder. Consequently, this response is theoretical and practically unrealistic, i.e., if the NES were to be placed inside the cylinder.

Initial and steady-state responses of both of the cylinder and NES for the mass ratio $\mu = 0.03$ are shown in Figs. 5.4(a) and 5.4(b). Figure 5.4(a) shows that the oscillation amplitude of the cylinder grows slowly. The NES attenuates the oscillations of the cylinder to an rms value near 0.0413, which constitutes a reduction of about 86% of the uncontrolled response. The responses of both subsystems are strongly modulated as shown in figure 5.4(b). The motion is highly localized in the nonlinear energy sink, as can be seen from figure 5.4(b). As discussed in the next section, this response is one of at least three responses, that depend on the initial conditions.

Similar response characteristics are observed for higher values of the mass ratio. For all of these mass ratios, it was observed that the energy pumping phenomenon starts after the oscillation amplitude of the cylinder exceeds a critical value. This critical amplitude increases as the mass ratio, μ, is increased. For example, the critical amplitude is $\frac{Y_2}{D} = 0.1003$ for

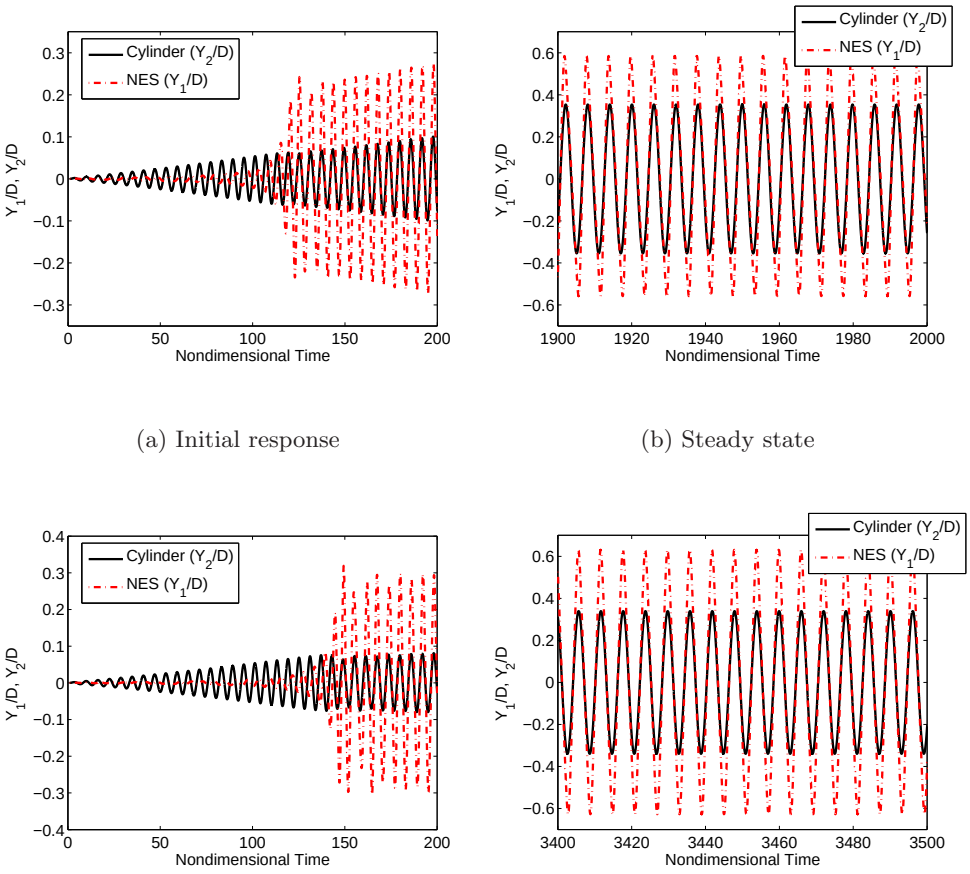

(a) Initial response

(b) Steady state

(c) Initial response

(d) Steady state

Figure 5.3: Responses of the cylinder and NES obtained using trivial initial conditions when Re = 106, $\tilde{K}_{nes} = 0.8\tilde{K}$, and $\tilde{C}_{nes} = 0.8\tilde{C}$: (a,b) $\mu = 0.01$ and (c,d) $\mu = 0.02$.

$\mu = 0.04$, $\frac{Y_2}{D} = 0.1119$ for $\mu = 0.05$, $\frac{Y_2}{D} = 0.1234$ for $\mu = 0.062$ and increases to $\frac{Y_2}{D} = 0.161$ for $\mu = 0.1$. Figure 5.5 shows the maximum amplitude of the NES as a function of the mass ratio with zero displacement and velocity as the initial conditions. Figure 5.5 and Table 5.1 show that the maximum amplitude is larger than 0.38D in the best case scenario, indicating that its implementation may be questionable because the secondary system must occupy some volume. Furthermore, in cases where the cylinder is used as a pipe, it would not be possible to place an NES system within it.

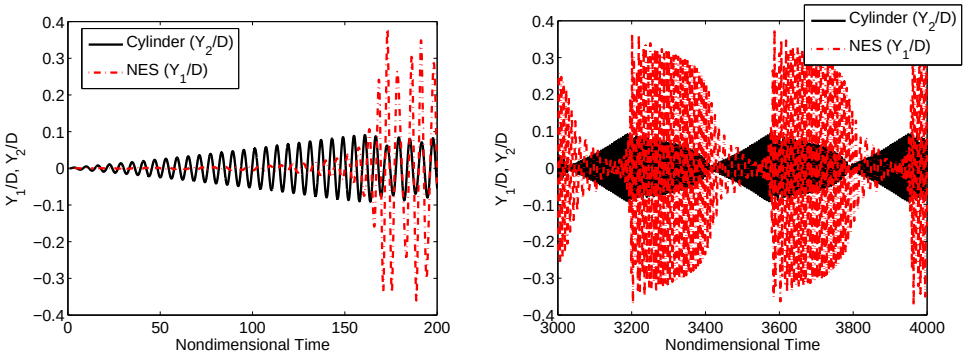

(a) Initial response (b) Steady state

Figure 5.4: Responses of the cylinder and NES obtained using trivial initial conditions for the mass ratio $\mu = \frac{M_{nes}}{M} = 0.03$ when Re $= 106$, $\tilde{K}_{nes} = 0.8\tilde{K}$, and $\tilde{C}_{nes} = 0.8\tilde{C}$.

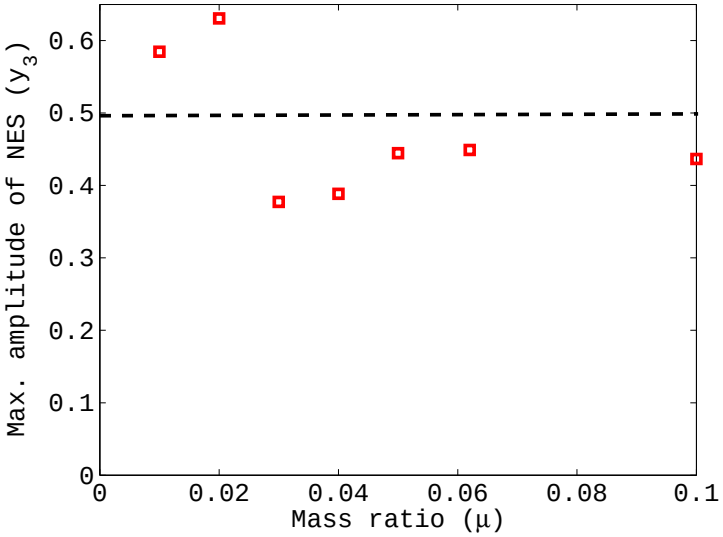

Figure 5.5: Variation of the maximum amplitude of the NES with the mass ratio $\frac{M_{NES}}{M}$ obtained using trivial initial conditions.

5.3.2 Effect of Initial Conditions

Malatkar and Nayfeh (70) investigated the system initially considered by Jiang et al. (57) and found multiple solutions for an undamped or slightly damped linear subsystem. They

Table 5.1: Effect of the mass ratio on the maximum oscillation amplitudes of both masses obtained using trivial initial conditions.

Cases	Mass ratio $\mu = \frac{M_{nes}}{M}$	max. y_1 (cylinder)	max y_3 (NES)
1	0.00	0.4167	0.0
2	0.01	0.3541	0.5848
3	0.02	0.3395	0.6308
4	0.03	0.0911	0.3773
5	0.04	0.1027	0.3885
6	0.05	0.1147	0.4447
7	0.062	0.1250	0.4490
8	0.1	0.1620	0.4366

observed that, in some cases, especially lightly damped systems, the NES actually increases the oscillation amplitude of the linear subsystem. To assess the effects of the initial conditions on the response of the VIV, we consider the response of the coupled system for a mass ratio $\mu = 0.03$ under different initial conditions. The damping and stiffness coefficients of the coupled system are set to $\tilde{K} = 1.13404$, $\tilde{C} = 0.0026$, $\tilde{K}_{nes} = 0.8\,\tilde{K} = 0.907232$, $\tilde{C}_{nes} = 0.8$, and $\tilde{C} = 0.00208$. The response of the coupled system for these parameters with zero initial conditions ($y_1 = y_3 = 0.0$ and $y_2 = y_4 = 0.0$) is shown in Figs. 5.4(a) and 5.4(b) and was discussed in the preceding section..

To determine the effects of the initial conditions, we change the velocity of the cylinder (y_2) while keeping $y_1 = 0.0$, $y_3 = 0.0$, and $y_4 = 0.0$. Figures 5.6(a) and 5.6(b) show the response of the coupled system for $y_2 = 0.1$. The plots show that the NES is able to suppress the high oscillation amplitude of the cylinder. Also, the system exhibits modulated responses similar to the ones observed for $y_2 = 0.0$, as shown in Figs. 5.4(a) and 5.4(b). The NES resonates with the cylinder; thus, making it possible to extract energy from the cylinder. Again, even in this best scenario, the NES oscillation amplitude is too large for practical implementation.

Next, we consider the response for $y_2 = 0.2$. The initial response of the coupled system

is shown in figure 5.6(c). The plots show that the response of the cylinder steadily grows to reach a stable limit cycle, as shown in figure 5.6(d). The nonlinear energy sink oscillates with an amplitude higher than that of the cylinder; indicating the activation of the energy pumping phenomenon. However, the NES is unable to effectively attenuate the oscillations of the cylinder. Qualitatively, the same behavior is observed when considering the cases of $y_2 = 0.3$ and 0.4, as shown in Figs. 5.6(e) and 5.6(f), respectively. Although the reduction in the rms of the oscillation amplitudes of the cylinder when $\mu = 0.03$ in the latter cases are high, the oscillation amplitudes of the NES mass exceed the radius of the cylinder and hence they are not practical.

Next, we consider the response of the coupled system when the cylinder is initially allowed to oscillate freely without activating the nonlinear energy sink and the NES is activated after a specific time. In the first simulation, the NES was activated after 100 nondimensional time units, as shown in figure5.7(a). The steady-state behavior of the coupled system is shown in figure 5.7(b), which is the same as that obtained with zero initial conditions. In the second simulation, the NES was activated after 250 nondimensional time units. The initial and steady-state responses of the coupled system are shown in Figs. 5.7(c) and 5.7(d), respectively. Here, it is observed that the oscillation amplitude of the cylinder grows under the action of the fluid forces, as shown in figure 5.7(c). As the nonlinear energy sink was activated after 250 nondimensional time units, the NES also starts oscillating with a high amplitude, which exceeds the radius of the cylinder, as shown in figure 5.7(d).

Numerical simulations were also performed to determine the effects of initial conditions for other mass ratios. Variation of the maximum amplitude of the NES mass and percentage reduction in the rms amplitude of the cylinder with the mass ratio is shown in Figs. 5.8(a) and 5.8(b). These plots show a range of mass ratios between 0.02 and 0.05 where we found multiple stable solutions. We emphasize that we only considered limited initial conditions and the coupled system may possess other stable solutions, depending on different initial conditions. Most of these solutions are not practical because the oscillation amplitudes of the NES mass exceed the cylinder radius. In the following section, we discuss the characteristics of these solutions.

Response Characteristics

Further insight into the character of the attractors (stable steady-state solutions) obtained using the limited initial conditions can be gained from the time histories, power spectra, phase portraits, and Poincaré sections presented in figure5.9. For the trivial initial conditions ($y_1 = 0.0, y_2 = 0.0, y_3 = 0.0$ and $y_4 = 0.0$), we observe the same modulated attractor of the response of the cylinder as shown in figure5.9(a). Figure 5.9(b) also shows that this response consists of more than one independent frequency. The two-dimensional projection of the phase portrait onto the $y_1 - y_2$ plane presented in figure 5.9(c) shows characteristics that indicate a non-periodic behavior. The Poincaré section in figure 5.9(d) shows an infinite number of points falling on a closed curve, indicating that the attractor is two-period quasiperiodic. The attractor obtained for the initial conditions $y_1 = 0.0, y_2 = 0.1, y_3 = 0.0$, and $y_4 = 0.0$ is the same as the attractor obtained for zero initial conditions, as can be seen from the time history, power spectra, phase portrait, and especially the Poincaré section presented in Figs. 5.9(e),5.9(f),5.9(g),5.9(h), respectively.

For the initial conditions $y_1 = 0.0, y_2 = 0.2, y_3 = 0.0$, and $y_4 = 0.0$, the response of the coupled system is quite different. Figure 5.9(i) shows that the response of the cylinder is periodic and qualitatively similar to that of the uncontrolled one. Figure 5.9(j) shows the power spectra of the displacements of the cylinder and the NES mass. Both spectra exhibit a sharp peak at 0.1669 and smaller peaks at its third and fifth harmonics. Furthermore, both of the subsystems oscillate with the same frequency. The two-dimensional projection of the phase portrait in figure 5.9(k) shows a single closed curve, confirming its periodic behavior. The Poincaré section in figure 5.9(l) consists of a single point, confirming the periodic nature of the response of the coupled system. The same periodic attractor was obtained for the initial conditions $y_1 = 0.0, y_2 = 0.4, y_3 = 0.0, y_4 = 0.4$, as shown from the time history, power spectra, phase portrait, and Poincaré section presented in Figs. 5.9(q),5.9(r),5.9(s),5.9(t), respectively. Next, as we set the initial conditions $y_1 = 0.0, y_2 = 0.3, y_3 = 0.0$, and $y_4 = 0.0$, the response of the coupled system is characterized by a period-doubled attractor. The power spectra shown in figure 5.9(n) consist of peaks at a frequency near the fundamental frequency of the periodic attractor and its odd harmonics as well as a subharmonic peak of

order one-half and its odd harmonics. The two-dimensional projection of the phase portrait, presented in figure 5.9(o), consists of two loops. The Poincaré section, figure 5.9(p), consists of two discrete points, confirming that the attractor is a two-period torus. Not surprising, the coupled nonlinear system possesses multiple attractors depending on the initial conditions.

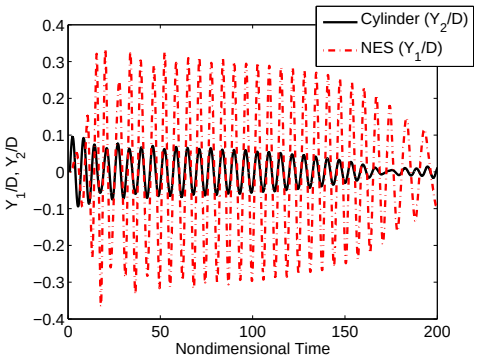

(a) Initial response $y_2 = 0.1$

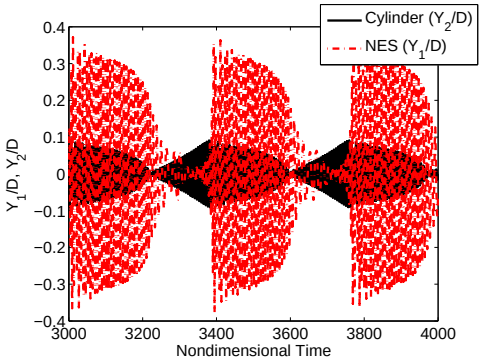

(b) Steady state $y_2 = 0.1$

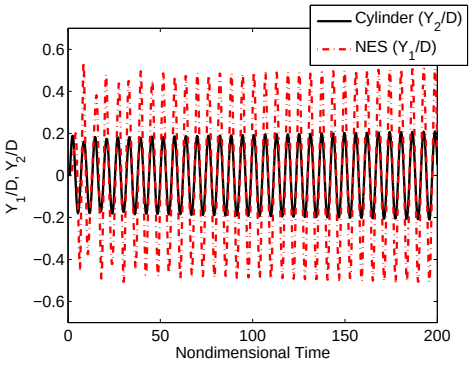

(c) Initial response $y_2 = 0.2$

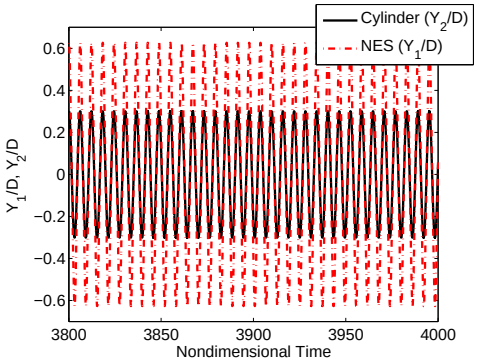

(d) Steady state $y_2 = 0.2$

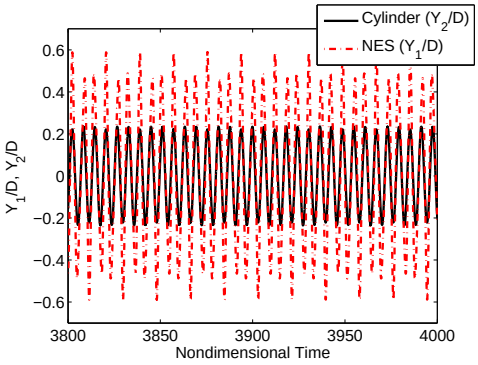

(e) Steady state $y_2 = 0.3$

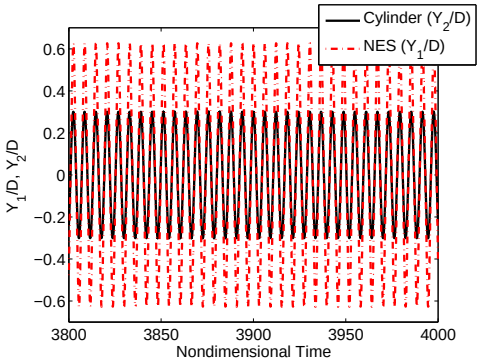

(f) Steady state $y_2 = 0.4$

Figure 5.6: Responses of the cylinder and NES obtained using different initial conditions for the mass ratio $\mu = \frac{M_{nes}}{M} = 0.03$ when Re $= 106$, $\tilde{K}_{nes} = 0.8\tilde{K}$, and $\tilde{C}_{nes} = 0.8\tilde{C}$.

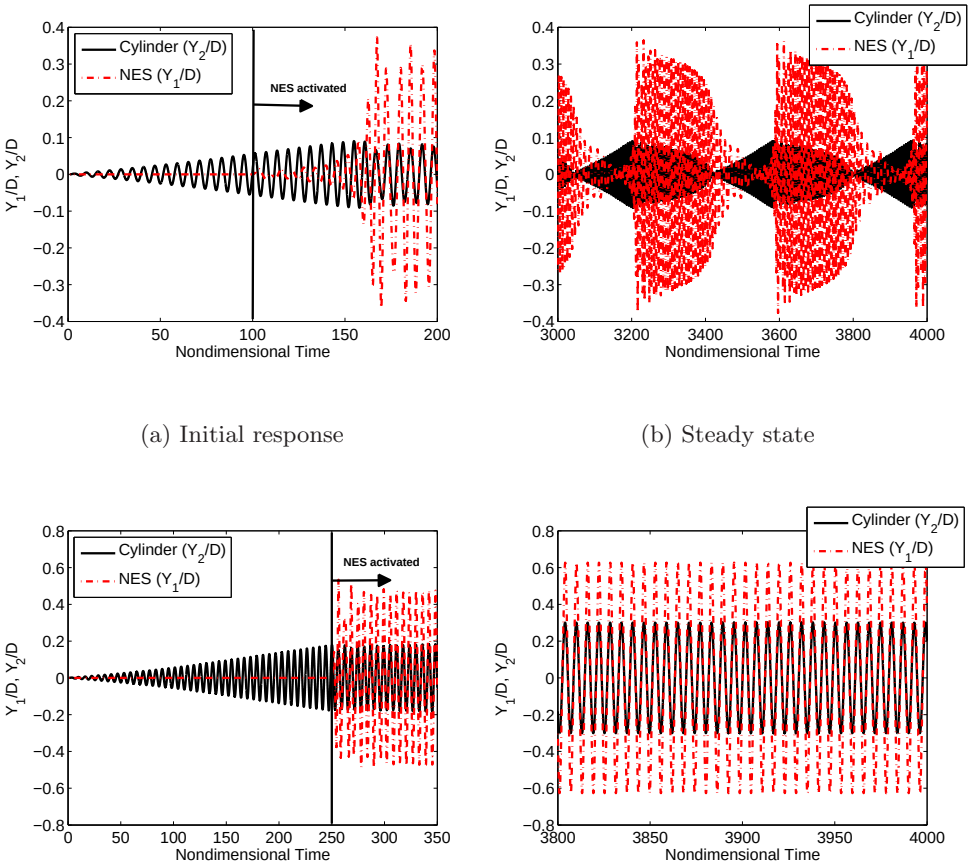

(a) Initial response

(b) Steady state

(c) Initial response

(d) Steady state

Figure 5.7: Responses of the cylinder and NES obtained where NES is activated after (a,b) $t = 100$, and (c,d) $t = 250$ nondimensional time steps for the mass ratio $\mu = \frac{M_{nes}}{M} = 0.03$, $\tilde{K}_{nes} = 0.8\tilde{K}$, and $\tilde{C}_{nes} = 0.8\tilde{C}$.

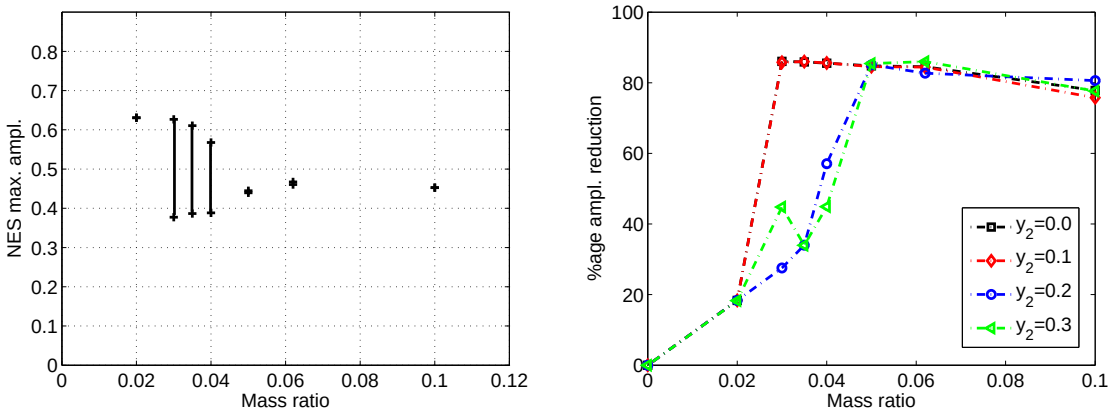

(a) (b)

Figure 5.8: (a) Variation of the maximum amplitude of the NES mass (b) Percentage reduction in the rms amplitude of the cylinder with the mass ratio $\frac{M_{NES}}{M}$ using different initial conditions.

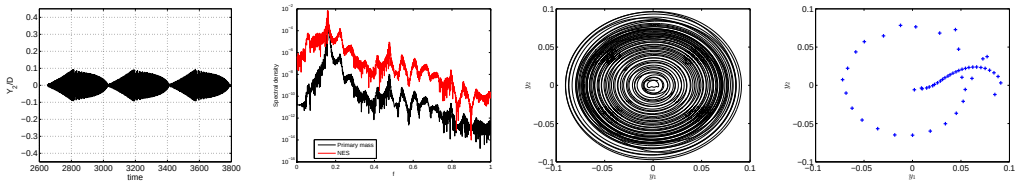

(a) $y_2 = 0.0$ (b) (c) (d)

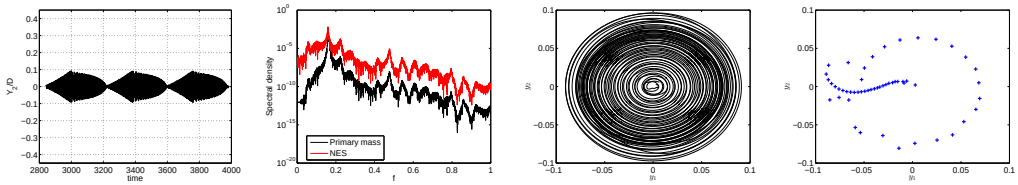

(e) $y_2 = 0.1$ (f) (g) (h)

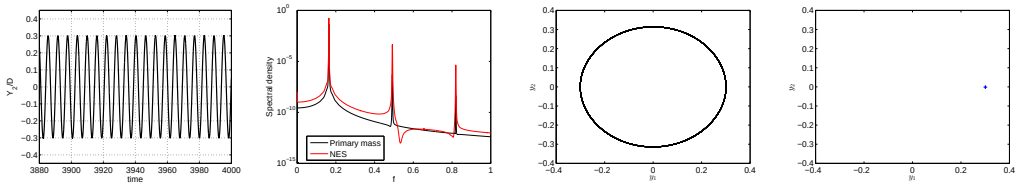

(i) $y_2 = 0.2$ (j) (k) (l)

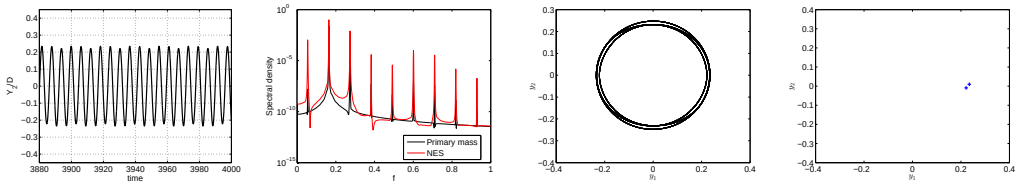

(m) $y_2 = 0.3$ (n) (o) (p)

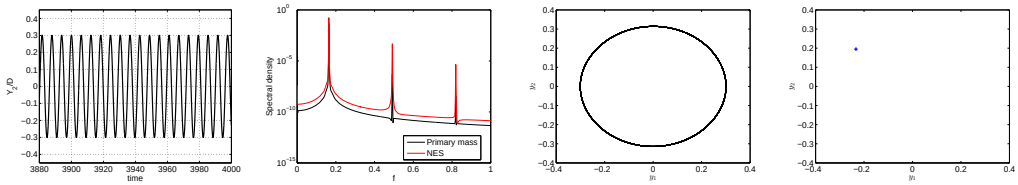

(q) $y_2 = 0.4$ (r) (s) (t)

Figure 5.9: Time histories(a,e,i,m,q), power spectra(b,f,j,n,r), phase portraits(c,g,k,o,s), and Poincaré sections(d,h,l,p,t) when Re = 106 and $\mu = 0.03$ obtained using different initial conditions.

5.3.3 Effect of Damping

To determine the effect of the damping coefficient $\tilde{C}_{nes}$ of the NES on the control of VIV, we vary its value while keeping all other parameters constant. We keep the mass ratio constant with a value $\mu = 0.03$ (i.e., mass of the NES is 3% of the mass of the cylinder). The stiffness of the NES is maintained constant and equal to $\tilde{K}_{nes} = 0.8\tilde{K} = 0.907232$. The damping and stiffness of the cylinder are also kept as $\tilde{C} = 0.0026$ and $\tilde{K} = 1.13404$, respectively.

Initially, we set the damping value of the NES equal to 40% of the damping value of the cylinder; that is, $\tilde{C}_{nes} = 0.4\tilde{C} = 0.00104$. The oscillation amplitude of the cylinder initially grows, as shown in figure 5.10(a), and reaches a stable limit cycle, as shown in figure 5.10(b). On the other hand, the NES mass oscillates with an amplitude higher than that of the cylinder. However, this amplitude is larger than the radius of the cylinder.

As we increase the damping coefficient of the NES mass to $\tilde{C}_{nes} = 0.7\tilde{C} = 0.00182$, modulated responses of the coupled system are observed, as shown in Figs. 5.11(a) and 5.11(b). Figure 5.11(a) shows that the oscillation amplitude of the cylinder slowly increases. After reaching a critical amplitude, the NES mass starts oscillating with a high amplitude. Beyond that, the oscillation amplitude of the NES mass increases and that of the cylinder decreases. The system response is similar to the modulated responses discussed above. The same modulated attractor is observed upon increasing the damping of the nonlinear energy sink to $\tilde{C}_{nes} = 0.8\tilde{C} = 0.00208$.

For low damping coefficient of the nonlinear energy sink, the response of the coupled system is periodic, but the NES amplitude exceeds the cylinder radius. As this coefficient is increased, the response acquires quasiperiodic characteristics. The maximum and the rms amplitudes of the cylinder and the NES mass are presented in Table 5.2. We can note from these results, that for small damping values, the NES is not able to reduce the oscillation amplitude of the cylinder and the maximum NES amplitude exceeds the cylinder radius. For large values, we found multiple stable solutions. Some of the solutions have NES amplitudes that exceed the cylinder radius.

Table 5.2: Effect of damping.

Cases	NES parameters	max. y_1 (cylinder)	max. y_3 (NES)
1	$\tilde{K}_{nes} = 0.8\tilde{K}, \tilde{C}_{nes} = 0.3\tilde{C}$	0.3619	0.7046
2	$\tilde{K}_{nes} = 0.8\tilde{K}, \tilde{C}_{nes} = 0.4\tilde{C}$	0.3514	0.6913
3	$\tilde{K}_{nes} = 0.8\tilde{K}, \tilde{C}_{nes} = 0.5\tilde{C}$	0.3402	0.6772
4	$\tilde{K}_{nes} = 0.8\tilde{K}, \tilde{C}_{nes} = 0.6\tilde{C}$	0.3282	0.6620
5	$\tilde{K}_{nes} = 0.8\tilde{K}, \tilde{C}_{nes} = 0.7\tilde{C}$	$0.0913 - 0.3124$	$0.3697 - 0.6142$
6	$\tilde{K}_{nes} = 0.8\tilde{K}, \tilde{C}_{nes} = 0.8\tilde{C}$	$0.0911 - 0.3008$	$0.3773 - 0.6268$

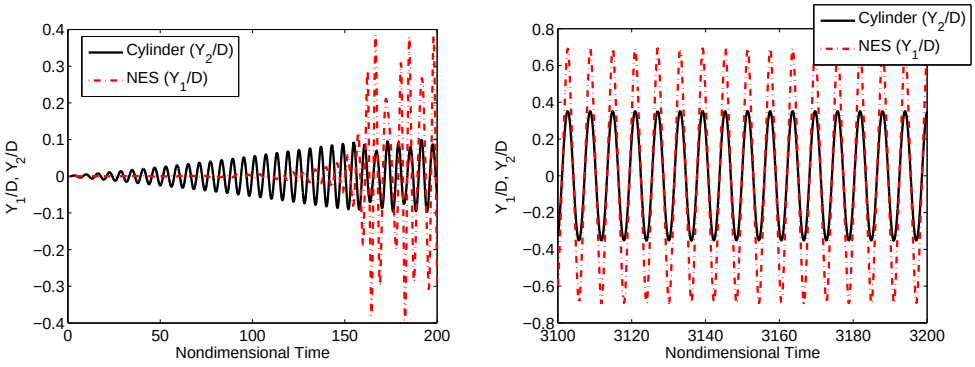

(a) Initial response

(b) Steady state

Figure 5.10: Responses of the cylinder and NES when Re = 106, $\mu = \frac{M_{nes}}{M} = 0.03$, where $\tilde{K}_{nes} = 0.8\tilde{K}$ and $\tilde{C}_{nes} = 0.4\tilde{C} = 0.00104$.

5.4 Conclusions

We investigated in detail the feasibility of using a nonlinear energy sink (NES) to control the vortex-induced vibrations of a freely oscillating circular cylinder. We solved simultaneously in the time domain for the motions of the cylinder, NES, and flow using a parallelized computer fluid solver. We varied the mass of the NES and its damping. We varied in a limited way the initial conditions from zero values. The results show periodic, two-period quasiperiodic, and period-doubled steady-state responses (attractors) that depend on these conditions. The

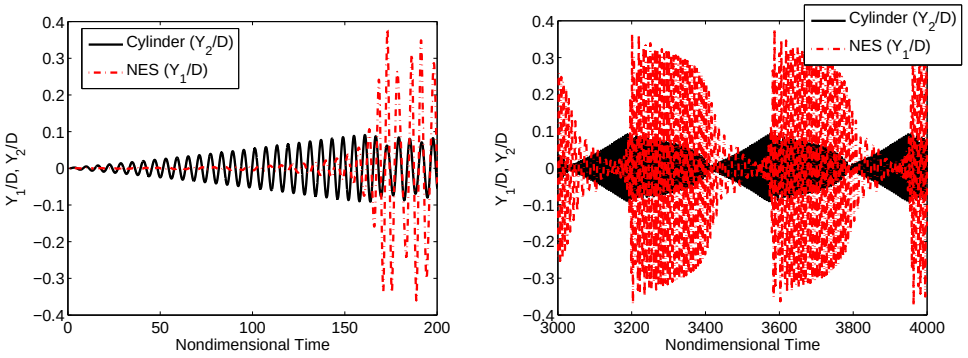

(a) Initial response

(b) Steady state

Figure 5.11: Responses of the cylinder and NES when Re = 106, $\mu = \frac{M_{nes}}{M} = 0.03$, where $\tilde{K}_{nes} = 0.8\tilde{K}$ and $\tilde{C}_{nes} = 0.7\tilde{C} = 0.00182$.

amplitude of the NES mass in most of the calculated solutions exceeds the cylinder radius, and hence they are not practical. For the best scenario of the multiple attractors, the maximum amplitude is larger than 76% of the cylinder radius, indicating that its implementation may be questionable. Furthermore, in cases where the cylinder is used as a pipe, it would not be possible to place an NES system within it.

Chapter 6

Optimization of Drag Reduction on a Cylinder Undergoing Rotary Oscillations

We discuss drag reduction through rotational oscillations of a circular cylinder and its optimization. The optimization is performed by combining a CFD solver with a global deterministic optimization algorithm. The use of this optimization tool allows for a rapid determination of the rotational amplitude and frequency domains that yield minimum drag. We observe that the rotational oscillations significantly affect the pattern of shedding vortices and find that the mean drag is decreased at higher forcing frequencies. The results show there is a threshold of rotational oscillation amplitude below which the mean drag does not decrease for any excitation frequency.

6.1 Introduction

The flow over a circular cylinder constitutes the canonical problem for studying flow separation, vortex shedding, and associated force coefficients (8; 13–15) in flows over bluff bodies. In these flows, an organised and periodic motion of a regular array of concentrated vorticity sheds from the body to form its wake. This vortex shedding is associated with the oscil-

latory forces on the body, which can be decomposed into drag and lift components along the freestream and crossflow directions, respectively. Reducing the strength of the generated vortices or affecting their shedding in an appropriate manner is thus a way of controlling these forces and any related vortex-induced vibrations. Many active and passive control mechanisms of the vortex shedding have been tested, both experimentally and numerically. For instance, passive controls include the use of splitter plates(12; 35; 36). Active controls such as suboptimal blowing and suction(73), inline and transverse oscillations(6; 31), and rotational oscillations (4; 5; 32–34) have also been proposed. In this chapter, the focus will be on reducing the mean drag on the cylinder through harmonic rotations of the cylinder.

Tokumaru and Dimotakis (32) performed experiments on a rotationally oscillating circular cylinder in a steady uniform flow at high Reynolds number $\mathrm{Re} = 15,000$. Using flow visualization and wake profile measurement, they reported that the fluctuating component of the drag can be reduced up to 80%. Thiria et al. (34) experimentally investigated the flow past a cylinder undergoing a harmonic rotation at $\mathrm{Re} = 150$. They observed that the forcing parameters affect the structure of vortex shedding. Numerical studies on the flow past an oscillating rotating cylinder have been performed by Shiels and Leonard(33) over a range of $150 \leq \mathrm{Re} \leq 15000$. Their results compare well with those obtained experimentally by Tokumaru and Dimotakis(32). They observed that multipole vorticity structures, triggered by appropriate rotational oscillations, reveal a bursting phenomenon in the boundary layer. This phenomenon leads to a time averaged separation delay and thus drag reduction. They also found that the impact of forcing depends strongly on the Reynolds number and would be effective only if $\mathrm{Re} \geq 3000$ because the viscosity suppresses the multipole growth in the case of low Reynolds number. The Reynolds number dependence for mean drag reduction was also observed by Choi et al.(4). They studied the effect of rotary oscillations in an unsteady laminar flow past a circular cylinder at $\mathrm{Re} = 100$ in the range of $0.2 \leq \Omega \leq 2.5$ and $0.02 \leq S_f \leq 0.8$, where Ω and S_f are the maximum rotational speed and forcing oscillation frequency, respectively, normalized by the free stream velocity and cylinder diameter. They computed the mean drag for Reynolds number of 100 and 1000 and found mean drag reductions of 12% and 60%, respectively. They observed that the lock-on frequency range becomes wider as Ω increases. They also determined that local minimum points for the mean drag were

found near the boundaries of the lock-on regions. Protas et al. (5) numerically investigated the flow over a cylinder undergoing rotary oscillations using the vortex method at Re = 150 and observed that the drag is reduced at the higher forcing frequencies. They also suggested that the mean drag coefficient does not monotonically decrease as the forcing frequency is increased, but there is an optimal forcing frequency beyond which the mean drag increases. The value of this frequency depends on Reynolds number and rotational amplitude.

In the present chapter, we investigate the effect of rotating the cylinder in an oscillatory motion on the mean drag at Reynolds number Re = 150. To this end, we combine an efficient global optimization code called VTDIRECT95 (74; 75) and the numerical methodology to find optimal rotational velocity and frequency that minimize the mean value of the drag.

6.2 Numerical Methodology and Validation

We use the same CFD solver 2.2.2 to simulate the flow field past a rotating cylinder in a uniform stream. To include the effect of the rotation of the cyinder, we enforce the boundary conditions as:

$$\begin{aligned} (u, v) &= (1, 0) \qquad \text{(inlet)}, \\ \tfrac{\partial \mathbf{u}}{\partial \mathbf{n}} &= 0 \qquad \text{(outlet)}, \\ (u, v) &= (-\Omega y, \Omega x) \qquad \text{(surface)} \end{aligned} \tag{6.1}$$

where Ω is the angular velocity of the cylinder and is nondimensionalized as $(\Omega D)/(2U_\infty)$.

To validate our numerical method for cylinders undergoing rotary oscillations, we compare our numerical results with those of Choi et al. (4) at Re = 100 and 1000 in the range of $0.2 \leq \Omega \leq 2.5$ and $0.02 \leq S_f \leq 0.8$ as shown in figure 6.1. The plot shows good agreement for the variation of the relative mean drag with the nondimensional forcing frequency S_f. In the current study, we use the Reynolds number of 150. The primary reason for choosing this Reynolds number is that the two- and three dimensional results are the same since the Mode A instability is initiated at Re = 180 (8). At Re = 150, we compare our numerical results with the results obtained by Protas et al. (5) with rotational oscillation amplitude $\Omega = 2.0$. As shown in figure 6.2, we find good agreement between the two results.

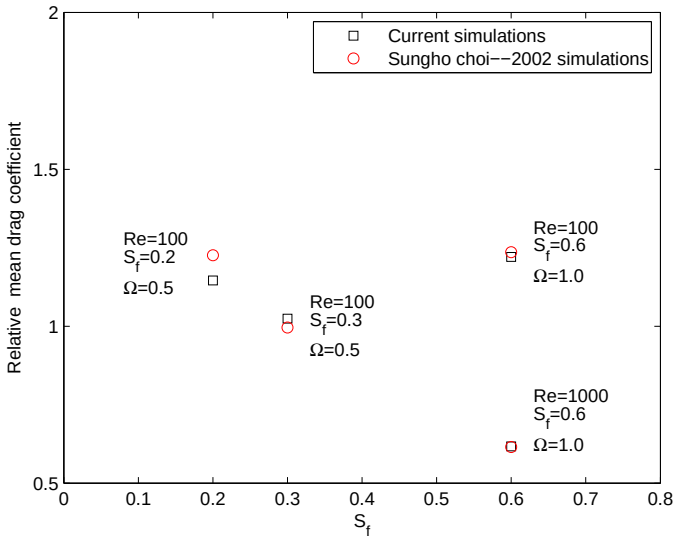

Figure 6.1: Comparison between current simulations and those of Choi et al. (4) for the variations of the mean drag coefficient, relative to that of the stationary cylinder, at Re = 100 1000 induced by rotational oscillations as a function of forcing frequency S_f where rotational amplitudes Ω varies as shown.

6.3 Global Optimization

To perform the optimization, we couple the parallel CFD code (24), solving the incompressible Navier-Stokes equations to simulate flows past a circular cylinder, with a deterministic global optimization algorithm VTdirect (74; 75) through an "interface module". The optimization package VTDIRECT95 is a Fortran 95 code that contains an implementation, called VTdirect, of a deterministic global optimization algorithm called direct (76). This algorithm is widely used in multidisciplinary engineering problems and physical science applications. It has been designed as an effective global optimization method that avoids being trapped at local optima and performs the search for global optimal points through three main operations that include

1. selection of potentially optimal boxes that are the regions most likely to contain the global optimum;

2. point sampling;

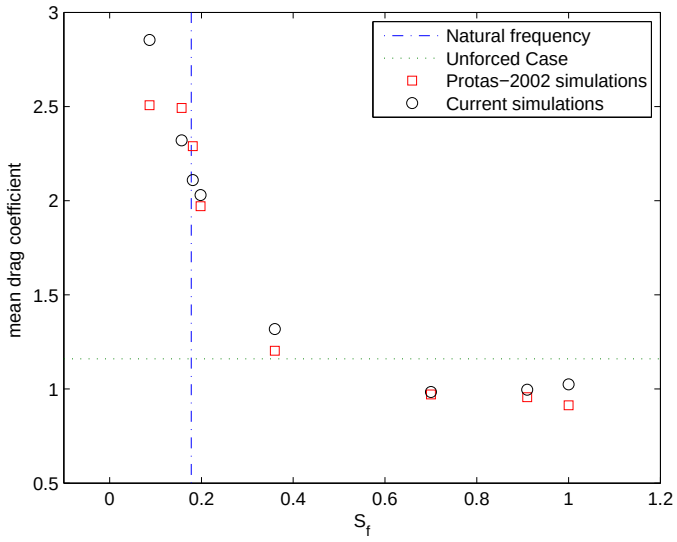

Figure 6.2: Comparison between current simulations and those of Protas et al. (5) for the variations of the mean drag coefficient at Re = 150 induced by rotational oscillations as a function of forcing frequency S_f where $\Omega = 2.0$.

3. space division.

A detailed description and implementation of the code is provided in He et al. (74; 75). A distinctive characteristic of deterministic algorithms like direct is their frugal use of function evaluations, compared to population based evolutionary algorithms.

In the optimization problem, we consider a cylinder undergoing rotational oscillations and investigate the reduction in the mean drag coefficient as the amplitude of the rotational oscillations (Ω) and forcing frequencies (S_f) are varied. As such, the optimization problem is formulated as

$$\begin{aligned} & \min \quad C_D(v_\theta), \\ \text{subject to} \quad & v_\theta \in D, \end{aligned}$$

where $v_\theta = (\Omega, S_f)$, $D = \{v_\theta \in R^2 \mid l_\theta \leq v_\theta \leq u_\theta\}$ is a 2-dimensional box, and C_D is the mean value of the drag coefficient.

In order to emphasize the usefulness of combining this optimization code (VTdirect) with the CFD solver, we note that most of the experimental or numerical studies dealing with drag

reduction through oscillatory rotations of circular cylinders consider variations of only one control parameter (4; 5; 34). In these studies, to identify the optimal point, a refined sweep is performed in the specified range of the control parameter. In the example of reducing the mean drag, the frequency is usually taken as the control parameter while keeping the amplitude of the rotational oscillation constant. Adding more control parameters would require many more experimental runs or a large number of numerical simulations to locate the optimal point where the mean drag is minimized. To show the significance of coupling the CFD code with an optimizer, we keep the rotational speed constant ($\Omega = 1.5$) and vary the frequency in the range $0.1 \leq S_f \leq 1.0$ with a constant increment of 0.1. As a brute force method, we perform ten simulations to obtain the frequency response curve as shown in figure 6.3. There is in fact a drag amplification when $S_f = 0.1$ and 0.2, these two data points are omitted in the plot. From this plot, we observe that the maximum drag reduction of approximately 14% occurs near $S_f = 0.7$. In order to further refine our results, we would require another set of simulations in the proximity of this locally optimal point, thus the total number of simulations may be of the order of 100.

In comparison we use VTdirect for one control parameter, i.e, frequency, and consider the same range of variations. VTdirect specifies the value of the input frequency and the simulations are performed to compute the mean drag. The interface module feeds back the computed mean drag to VTdirect, which specifies the rotational frequency for the next simulation. In this way, VTdirect searches for the optimal point where minimum mean drag is achieved. The frequency search for the minimum mean drag is also plotted in the figure 6.3 for the sake of comparison. The results show that VTdirect was able to converge to a drag reduction factor of 14% corresponding to $S_f = 0.65$ with only five simulations. On the other hand, the brute force method would have required many more simulations to identify the optimal point. Thus, VTdirect provides an efficient algorithm to locate the optimal configuration for reducing the mean drag. Considering other parameters would add significantly to the computational cost of parameter sweeps. The same argument can be extended to the application of VTdirect for more than one control parameter where each parameter has its own sweeping range. If we require N_s simulations for one control parameter, then using a brute force method, P control parameters would require N_s^P simulations, orders

of magnitude more than VTdirect would need.

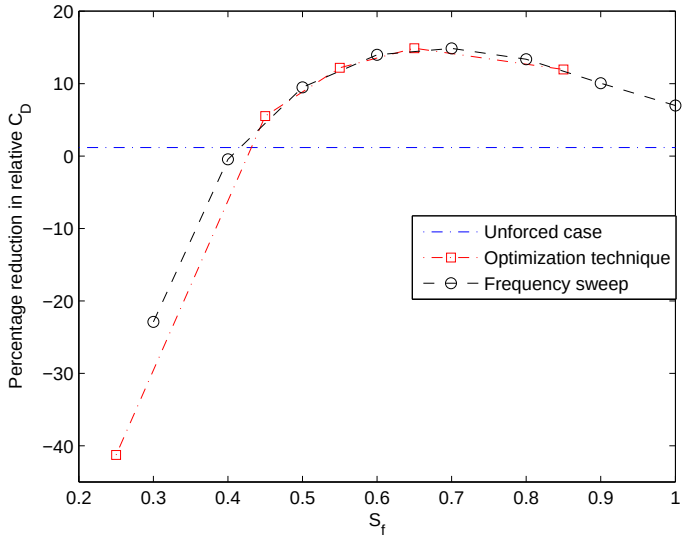

Figure 6.3: Percentage reduction in the mean drag coefficient with the non-dimensional forcing frequency S_f for a rotationally oscillating cylinder at Re = 150 with the non-dimensional rotational amplitude $\Omega = 1.5$.

6.4 Results and Discussion

In order to investigate the physics of drag reduction using the rotation of the cylinder as a control mechanism, we consider variations of the amplitude (Ω) and the frequency (S_f). The upper and lower bounds of the amplitude of the rotational oscillations (Ω) and forcing frequency (S_f) are shown in Table 6.1.

Table 6.1: Control variables constraints (rotation motion).

Parameter	Lower bound	Upper bound
Ω	0.1	3.0
S_f	0.1	1.0

To perform the optimization search, we specify the maximum number of iterations and function evaluations, the minimal relative change in the objective function and minimum box diameter. These limits serve as the stopping conditions for VTdirect. In the current study, we specify the limit on the number of function evaluations used by VTdirect as 41. By specifying the above stopping conditions, the optimization algorithm yielded the four locally optimal results reported in Table 6.2.

Table 6.2: Summary of locally optimal points.

Case	Ω	S_f	C_D
1	2.08	0.78	0.975
2	2.18	0.78	0.9759
3	2.30	0.78	0.9779
4	2.08	0.75	0.9796

Experimental (32; 34) and numerical studies (4; 33) show that changes in the value of drag coefficient on a rotationally oscillating cylinder are associated with changes in the structure of the wake of the cylinder. Depending on the oscillation amplitude Ω and forcing frequency S_f, the wake of the cylinder exhibits different flow patterns. For some specific values of these control parameters, the vortices are shed with the external excitation frequency and the phenomenon is then referred to as "lock-in" or "synchronization" whereby the frequency of vortex shedding becomes identical to that of the cylinder oscillations. As such, the body oscillations control the flow pattern in the wake and forces on the cylinder.

To determine the effects of forcing the cylinder with rotary oscillations on its wake, we use the flow over a stationary cylinder at Re = 150 as the reference case. Three snapshots of contours of the instantaneous vorticity in the wake of the stationary cylinder are shown in figure 6.4. The plots show an alternating pattern for the vortex shedding from the upper and lower halves of the cylinder. Snapshots of vorticity contours for the optimal case of drag reduction where $\Omega = 2.08$ and $S_f = 0.78$ obtained from VTdirect are shown in figure 6.5. The contours show that the oscillatory cylinder releases single vortices of opposite signs during

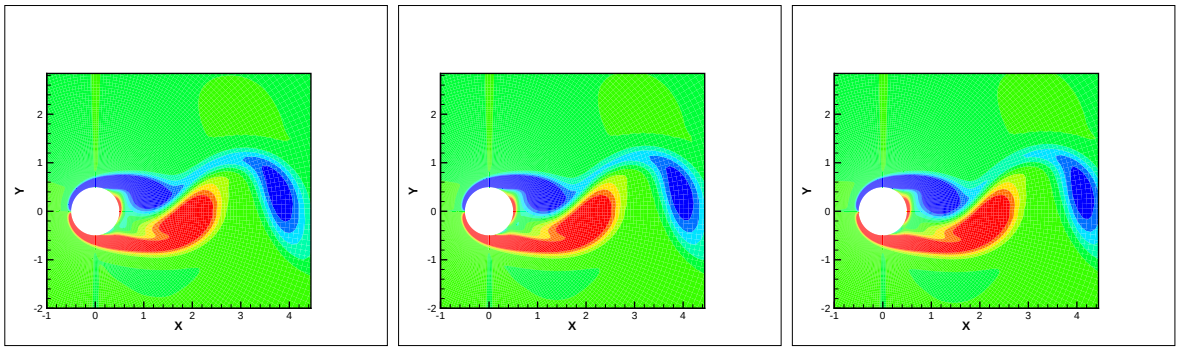

(a) (b) (c)

Figure 6.4: Three snapshots of the vorticity contours for the flow over a stationary cylinder.

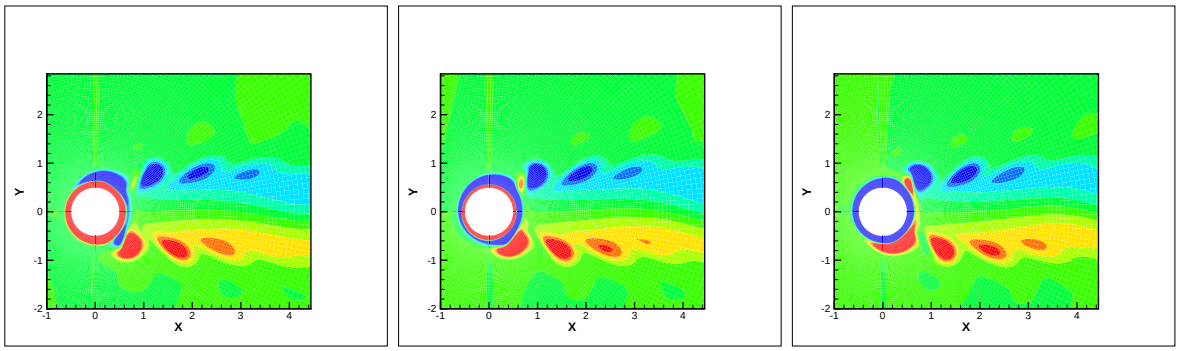

(a) (b) (c)

Figure 6.5: Snapshots of the vorticity contours for the case where the highest percentage reduction in the mean drag coefficient($\approx 16\%$) at $\Omega = 2.08$ and $S_f = 0.78$ is attained.

each half cycle. It is observed from the power spectra of the lift and drag coefficient, shown in figure 6.6, that the vortices are shed at the rotational oscillation forcing frequency. The magnitude of the peak at this frequency is much larger than the magnitude of the peak corresponding to the shedding frequency of the stationary cylinder.

Snapshots of the vorticity contours for the case where the mean drag coefficient is increased significantly (by 42%) are presented in figure 6.7. In this case, the wake structure is still synchronized with the forcing frequency but the wake exhibits large-scale vortices behind the

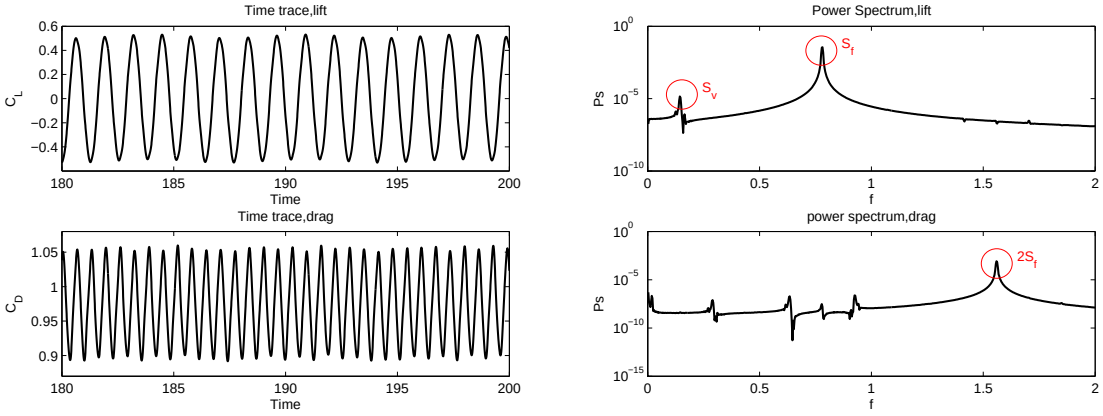

(a) (b)

Figure 6.6: Time histories(a) and power spectra(b) of the optimal case for $\Omega = 2.08$ and $S_f = 0.78$.

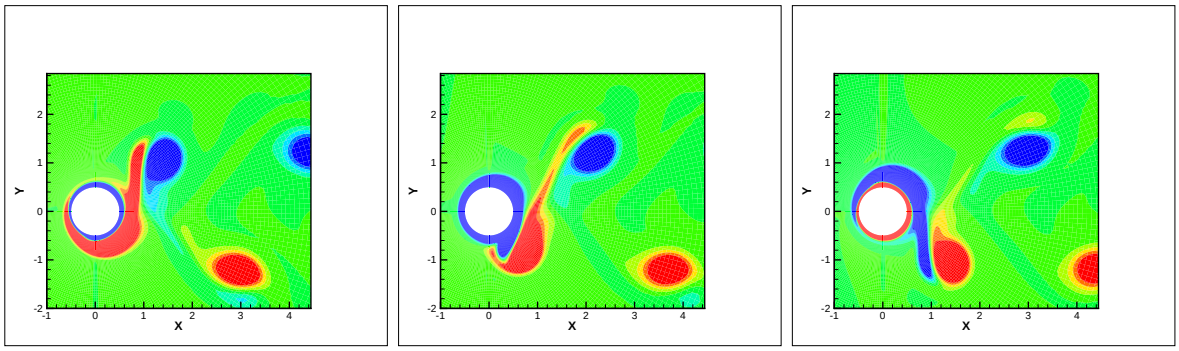

(a) (b) (c)

Figure 6.7: Snapshots of the vorticity contours for the case where the mean drag coefficient($\approx$ 42%) at $\Omega = 1.55$ and $S_f = 0.25$ is increased.

body that are shed in an alternating manner. The vortices on the lower half of the cylinder are the result of counter-clockwise rotation of the cylinder, during which the rotation of the cylinder generates vorticity and the incident flow sheds it into the wake.

figure 6.9 and Table 6.3 show variations of the mean values of the drag coefficient with the forcing frequency. The results are presented in terms of the percentage reduction in the drag

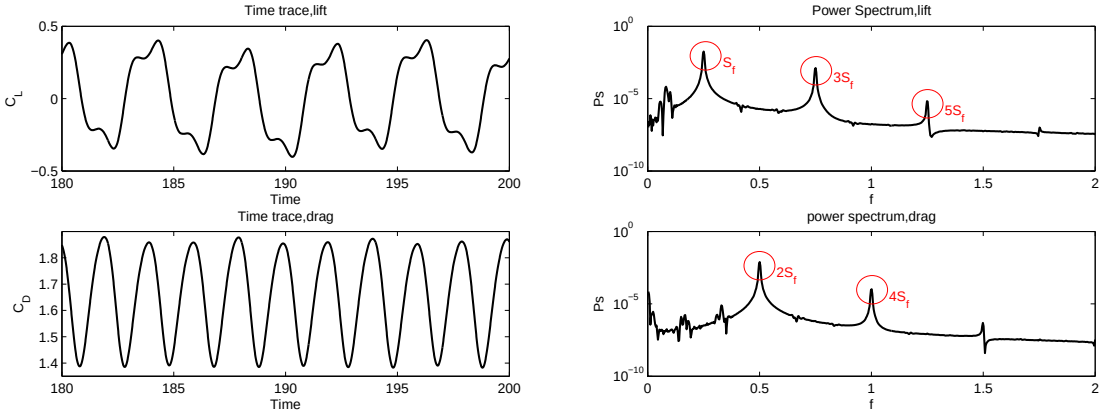

(a) (b)

Figure 6.8: Time histories(a) and power spectra(b) for the percentage increase in the mean drag coefficient($\approx 42\%$) at $\Omega = 1.55$ and $S_f = 0.25$.

coefficient relative to the its value on a stationary cylinder. The first observation to be made here is that at low oscillation frequencies ($S_f < 0.25$), the drag coefficient is larger than that of the stationary case. Over this region, increasing the amplitude of the oscillations results in significant increase in the value of the drag coefficient. As the forcing frequency is increased to values above 0.45, the drag coefficient becomes smaller than that of the stationary cylinder. These observations indicate a minimum threshold for the oscillation frequency to attain drag reduction. The highest reduction of about 15% is attained over the forcing frequency range between 0.75 and 0.85 and at oscillations amplitudes that are near 2.20.

6.5 Conclusions

We have simulated the flow past a cylinder undergoing harmonic rotational oscillations and investigated the effect of rotational motion on the drag force. We have combined a CFD solver with a global optimizer to speed up the search for the regions where maximum drag reduction can be realized. Our results showed that increasing the forcing frequency leads to a reduction in the drag. We found that drag reduction may reach 16% for an excitation frequency equal to 4.7 times vortex shedding frequency. We also observe that there is a threshold of the

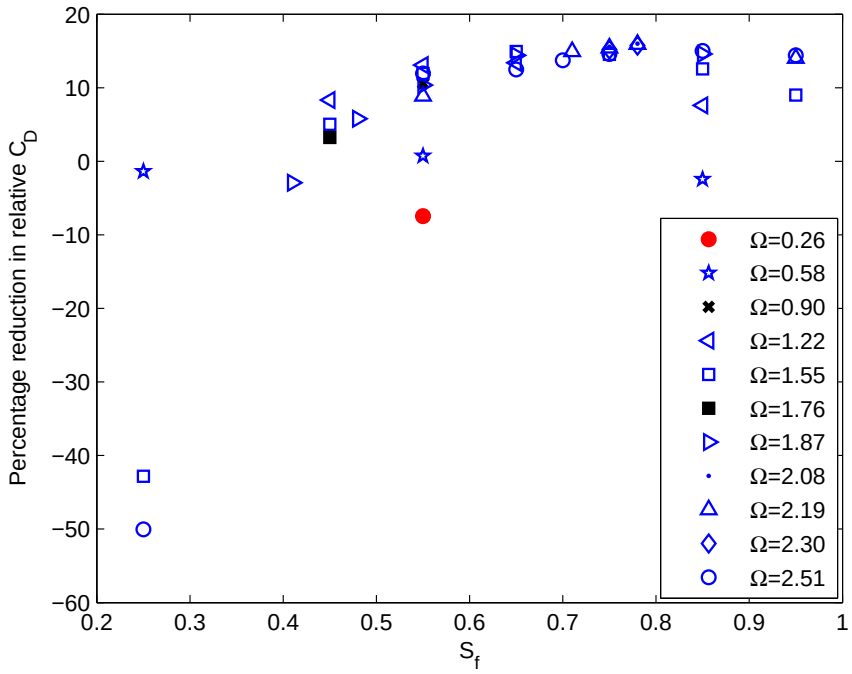

Figure 6.9: Summary of percentage variations of the reduction in the mean drag coefficient with the non-dimensional forcing frequency S_f for a rotationally oscillating cylinder at Re = 150 with the various non-dimensional rotational amplitudes Ω as obtained from VTdirect.

oscillation amplitude below which the mean drag does not decrease for any forcing frequency. We argue that the small and large vortices that are shed in the wake of the cylinder are responsible for low and high pressure gradients, thus modifying the drag force. Furthermore, these modifications in the wake are associated with the injection of external vortices obtained by the rotation of the cylinder. The use of the optimizer enabled the identification of the optimal points where maximum drag reduction is reached.

Table 6.3: Summary of percentage variations of the reduction in the mean drag coefficient with the nondimensional forcing frequency S_f for a rotationally oscillating cylinder at Re = 150 with the various non-dimensional rotational amplitudes Ω as obtained from VTdirect; *italics*(threshold points); **boldface**(optimal points).

2.50	*-50.052*				11.927	12.478	13.719		14.59		15.003	14.392
2.45					7.627							
2.37			*-0.629*									
2.30									**15.176**	**15.727**		
2.20					0.876			14.917	**15.417**	**15.9**	**15.236**	
2.08									**15.581**	**15.977**		
1.97			*1.732*									
1.87		*-2.921*		5.774	10.358	14.409					14.59	
1.76			3.232									
1.55	*-42.821*		5.041		11.927	14.926					12.565	8.997
1.20			8.333		13.09	13.401					7.609	
0.90					10.565							
0.58	*-1.37*		*0.724*			*-2.456*						
0.26					*-7.454*							
Ω/S_f	0.25	0.41	0.45	0.48	0.55	0.65	0.70	0.71	0.75	0.78	0.85	0.95

Chapter 7

Synchronization and Force Reduction of In-line Oscillating Cylinder

We perform two and three-dimensional numerical simulations of the flow past an inline vibrating cylinder and plot the frequency/amplitude response curves. We focus on the three-dimensional effects on the inline vibrating flow field and compare the response with corresponding two-dimensional frequency/amplitude response curves. We observe that more energy is required to achieve synchronization for three-dimensional flows when compared to the corresponding two-dimensional ones. We attribute this effect to the presence of dominant streamwise structures in the wake.

7.1 Introduction

Most of the experimental and numerical investigations have considered cross-flow vibrations for studying the effect of the forcing frequency and amplitude on the vortex shedding and its relevance to vortex-induced vibrations (VIV) (8; 10; 15; 16; 77–79). It has been observed that, if the forcing amplitude is large enough and the forcing frequency is close to the natural shedding frequency, *synchronization* takes place, causing the shedding to occur at the forcing

frequency.

In contrast, fewer studies (6; 7; 80) considered the synchronization phenomenon between vortex shedding and inline cylinder oscillations. It was found both experimentally (6) and numerically (7) that, in the *synchronization* region, the cylinder oscillations reduce the rms of the lift coefficient to near zero. The mean drag also drops and saturates at a value independent of the driving frequency. Our main focus is to further extend the earlier two-dimensional investigation of this phenomenon by Marzouk and Nayfeh (7) and analyze the effects of the third dimension.

Lift suppression may be used in various applications in which transverse forces are undesirable(80). However, for all practical purposes, three-dimensional (3-D) effects must be considered. For instance, it has been observed that the 3-D vortical structures alter the wake significantly after the onset of Modes A and B instabilities at Re $\approx$ 180 and Re $\approx$ 260, respectively (77; 81). As a result, two-dimensional (2-D) simulations, which do not capture the streamwise vortices, fail to accurately predict the flow field (15; 77). Furthermore, as shown in Table 7.1, 3-D simulations predict flow quantities more accurately than their 2-D counterpart.

7.2 Numerical Methodology and Validation

We use the same CFD solver described in Section 2.2.2 to simulate the flow field past an inline vibrating cylinder in a uniform stream. In the current simulations, the equation governing the nondimensional displacement (forced-oscillation) of the cylinder is modeled by a simple harmonic motion in the inline direction as follows:

$$x = A_x \sin(2\pi f_e t) \tag{7.1}$$

where A_x is the nondimensional amplitudes in the inline direction, and f_e is the nondimensional excitation frequency.

We validate the inline oscillations of the parallel CFD solver by comparing the current numerical results with the experimental data of Tanida et al. (6). They conducted their experiments in oil at $Re = 80$, with the inline motion amplitude $A_x = 0.14D$. They took all the measurements at the central section of the test cylinder in order to reduce the three

dimensional effects. Figure 7.1(a) shows the comparison between our simulation and the measurements for different forcing-to-shedding frequency ratios f_e/f_{st} with the nondimensional excitation frequency f_e for an inline cylinder oscillating. figure 7.1(a) shows good agreement between the simulation results and the reported measurements and also exhibits one type of synchronization in which f_{st} is equal to f_e/f_{st}. figure 7.1(b) compares variations of the mean drag of a single in-line oscillating cylinder with the nondimensional excitation frequency f_e and found a good agreement between the current simulations and the experimental data.

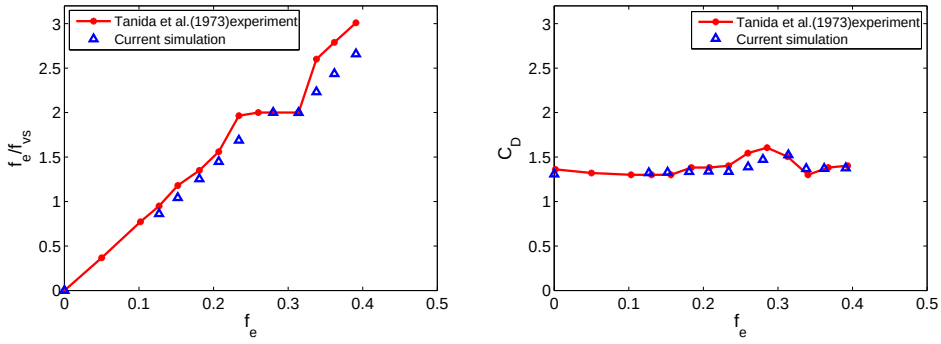

(a) (b)

Figure 7.1: Comparison between our simulations and the measurements of Tanida et al. (6) for the variations of (a) the forcing-to-shedding frequency ratio f_e/f_{vs} and (b) the mean drag with the non-dimensional excitation frequency f_e for an inline oscillating cylinder at Re = 80 with a nondimensional amplitude $A_x = 0.14$.

7.3 Results and Discussion

We perform 2-D and 3-D simulations at Re = 500 and 1000 using a parallel CFD solver, in contrast with the artificial compressibility code used by Marzouk and Nayfeh (7). Details of the formulation, validation, and verification of the numerical method can be found in Ref. (53). For the 2-D simulations, we employ a 192×256 grid with the domain size of $30D$, where D is the cylinder diameter. On the other hand, for the 3-D simulations, we employ a $192 \times 256 \times 32$ grid with a span $L_z/D = \pi$. In figure 7.2, we plot the root mean square

Table 7.1: Computed flow parameters.

Data from	Re	$\overline{C_D}$	C_L^{max}	St
2-D (7)	500	1.37	1.02	0.217
2-D (Present)	500	1.3431	1.09	0.2197
3-D DNS (77)	525	1.24	0.64	−−
3-D DNS (Present)	500	1.2864	0.9489	0.2075
Experiment(82)	1000	1.0	−−	0.21
2-D (83)	1000	1.54	−−	0.238
2-D (Present)	1000	1.4290	1.3822	0.2319
3-D DNS (83)	1000	1.02	−−	0.202
3-D DNS (Present)	1000	1.11	1.1004	0.205

(rms) of the lift coefficient relative to the one obtained for the stationary case for a forcing amplitude of $A_x/D = 0.2$. The predicted synchronization region is in good agreement with that predicted by Marzouk and Nayfeh(7).

To further investigate the onset of the synchronization phenomenon, we perform numerous simulations to obtain frequency-response curves using both 2-D and 3-D simulations of the flow field. To achieve this, we perform sweeps over a wide range of inline forcing amplitudes and frequencies and determine synchronization maps for Re = 500 and 1000. The outcomes are plotted in figure 7.3, which shows the non-dimensional forcing amplitude A_x/D as a function of the ratio of the forcing frequency f_{ex} to the Strouhal or vortex shedding frequency f_{st} of the stationary cylinder. The lines in figure 7.3 indicate the boundaries separating synchronization and non-synchronization. The key observations are as follows:

1. In the 2-D simulations, as the Reynolds number is increased from 500 to 1000, the synchronization boundary is shifted to the left, indicating that a smaller forcing amplitude is needed to achieve synchronization with the same forcing frequency. On the contrary, in the 3-D simulations, as the Reynolds number is increased from 500 to 1000, the synchronization boundary is shifted to the right, indicating that a larger forcing

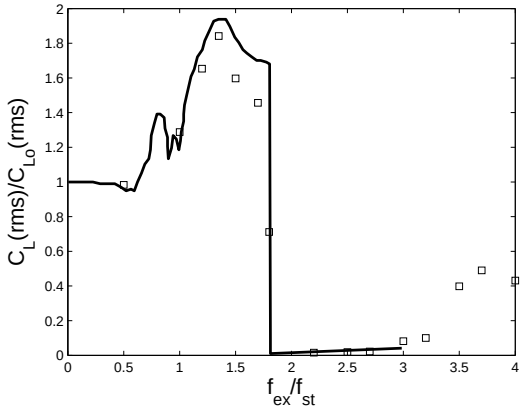

Figure 7.2: Comparison of the variation of the relative rms C_L with the non-dimensional forcing-to-shedding frequency f_{ex}/f_{st} obtained by Marzouk and Nayfeh(7)(solid line) with that obtained with the current simulations(square) for a non-dimensional forcing amplitude $A_x/D = 0.20$ and Re $= 500(2D)$.

amplitude is needed to achieve synchronization with the same forcing frequency.

2. The slope of the synchronization boundary remains almost the same in both of the 2-D and 3-D simulations.

3. For both Re = 500 and 1000, synchronization of the 3-D flow requires a higher forcing frequency than the 2-D flow for the same forcing amplitude.

To explicitly asses the effect of the forcing frequency on the lift suppression, we fix the forcing amplitude and oscillate the cylinder along the stream over a range of frequencies between $1.6f_{st}$ and $2.3f_{st}$ for two Reynolds numbers. In figure 7.4, we show variation of the 3-D simulated relative rms C_L with the non-dimensional forcing-to-shedding frequency f_{ex}/f_{st} for Re = 500 and Re = 1000 and four forcing amplitudes. We observe that, before initiation of synchronization, the lift amplitude is higher than that of the stationary cylinder. Once synchronization takes place, the lift amplitude decreases abruptly, resulting in complete suppression of the lift. The mean drag coefficient exhibits similar qualitative behavior, but it is reduced only by 20% and then remains constant independently of the forcing frequency (84).

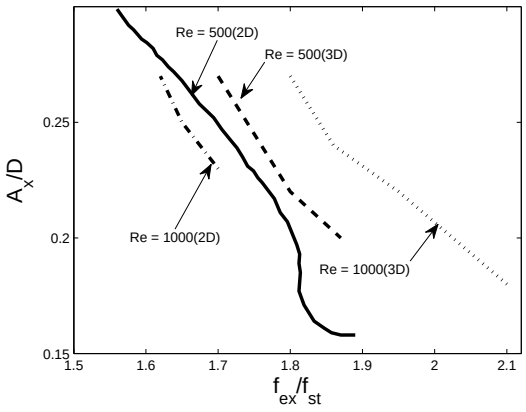

Figure 7.3: Comparison between the synchronization maps obtained by Marzouk and Nayfeh(7) for Re = 500($2D$) (solid line) and the present simulations for Re = 500($3D$) (Dashed line), Re = 1000($3D$) (Dotted line), and Re = 1000($2D$) (Dashed-dot line).

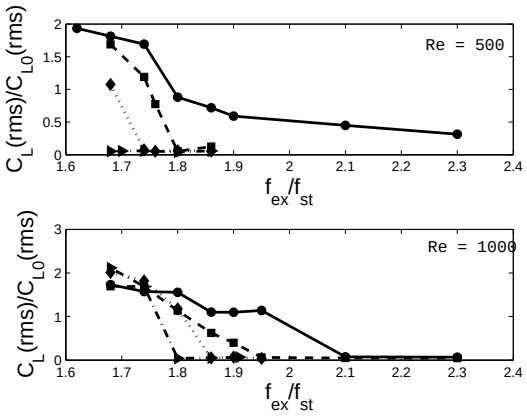

Figure 7.4: Variation of the 3-D simulated relative rms C_L with the non-dimensional forcing-to-shedding frequency f_{ex}/f_{st} at Re = 500 and Re = 1000; $A_x/D = 0.18$ (solid line, circle), $A_x/D = 0.22$ (Dashed line, square), $A_x/D = 0.24$ (Dotted line, diamond), $A_x/D = 0.27$ (Dashed-dot line, Right pointing triangle)

.

The need for higher magnitudes of the amplitude/frequency to achieve lift reduction, in three-dimensional flows, can be explained from the vortical structures developed in the wake. In the flow over a stationary cylinder, the increase in the Reynolds number from 500 to 1000 destabilizes the structured wake, resulting in a more significant breakdown of the large vortices, as shown in figure 7.5(a) and 7.5(b). These results are in line with the experimental visualization of Williamson (8) and the numerical results of Mittal and Balachandar (77). When the cylinder oscillates along the stream in the non-synchronous regime, vortex shedding persists in an alternating manner, as can be seen in figure 7.5(c) and 7.5(d). This oscillatory nature of the vortices causes the variation in the instantaneous lift force on the cylinder. On the other hand, in the synchronous regime, symmetric vortices are shed from the top and bottom sides of the cylinder, as shown in figure 7.5(e) and 7.5(f).

From a dynamical system viewpoint, synchronization occurs when the forcing frequency entraps the natural frequency. In the synchronous regime, the inertia of the cylinder moving in the streamwise direction takes over the formation of alternate vortex shedding on the cylinder. The vortices are shed simultaneously from the top and bottom surfaces of the cylinder, rendering the flow symmetric about the streamwise axis. For the sake of clarity, we term this behavior as "inertia coupling". This results in a symmetric distribution of the pressure with respect to the x-axis and, in turn, leads to lift suppression, which is a manifestation of the synchronization phenomenon.

We explain each observed phenomenon in figure 7.3 with the following arguments:

1. In the two-dimensional case, the synchronization curve shifts to the left as the Reynolds number is increased from 500 to 1000. With the increase in the Reynolds number, the vorticity in the wake increases, causing the vortices in the wake to be more "compact" or concentrated. In this configuration, inertia coupling takes place at relatively lower forcing frequency and amplitude. On the contrary, for three-dimensional flows, the wake becomes unstable as the Reynolds number is increased. In other words, the wake is no more "compact" and contains complex vortical structures, such as ribs, hair-pin, horse-shoe vortices, etc. Thus, it requires more energy (higher inline frequency ratio or amplitude) to drive the flow towards inertia coupling.

2. The inertia coupling generally shows a similar trend for all cases presented here. It is also a measure of how much energy is required to maintain this coupling on a frequency-amplitude plot. The trend becomes nonlinear at extreme values of frequencies and amplitudes.

3. Keeping the Reynolds number fixed beyond Mode A instability, the third dimensionality allows the flow to destabilize in the spanwise direction. Complex vortical structures are formed in the wake and more inertia is required to overcome these structures and align them in the synchronized state. Thus, for both of the Reynolds numbers of 500 and 1000, the synchronization curve is shifted to the right. We observe a larger shift for $\mathrm{Re} = 1000$ than for $\mathrm{Re} = 500$ due to the more complex structures in the wake.

To appropriately predict the synchronization region and benefit from the lift suppression phenomenon, that is associated with inline forcing of circular cylinders, in engineering and industrial applications, it is important to understand the effects of the wake and spanwise variations. In this work, we have analyzed the lift suppression phenomenon that occurs when the frequency of inline oscillations is close to twice that of the vortex shedding frequency. We have observed a shift in the synchronization maps towards higher frequency ratios/amplitude of oscillations indicating that more energy is required to achieve synchronization in the three-dimensional flow.

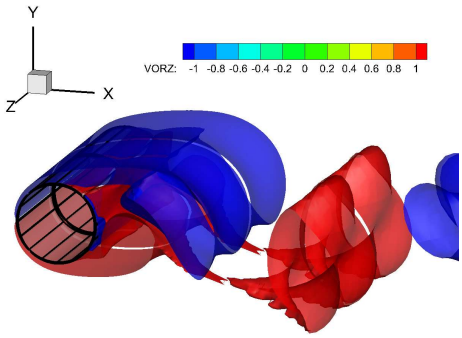

(a) Stationary at Re = 500

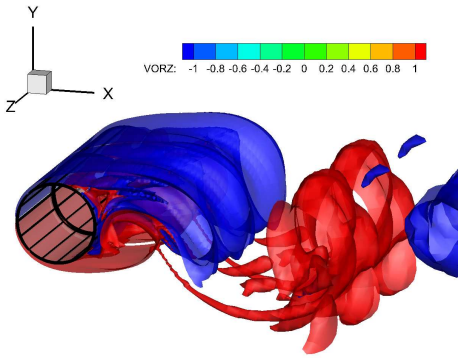

(b) Stationary at Re = 1000

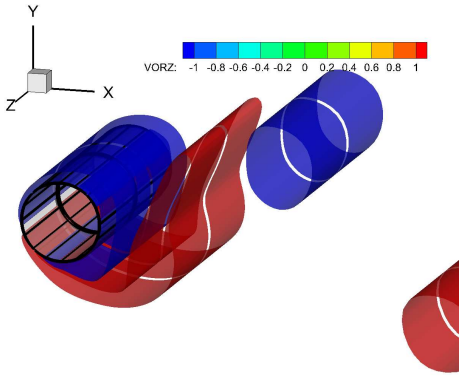

(c) Nonsynchronous at Re = 500

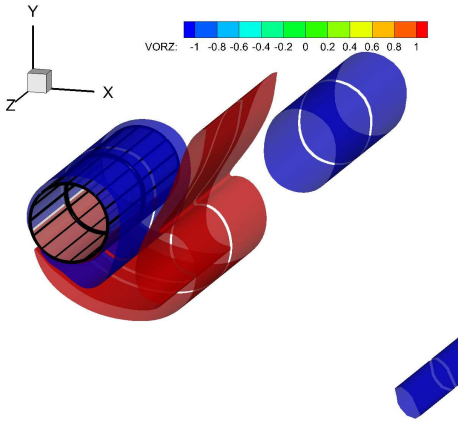

(d) Nonsynchronous at Re = 1000

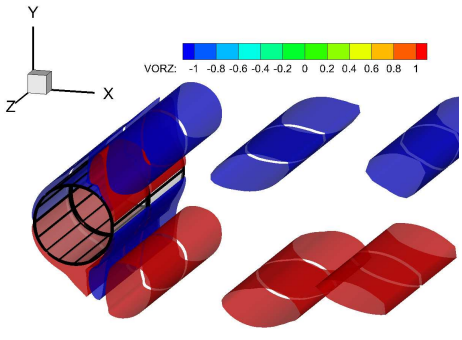

(e) Synchronous at Re = 500

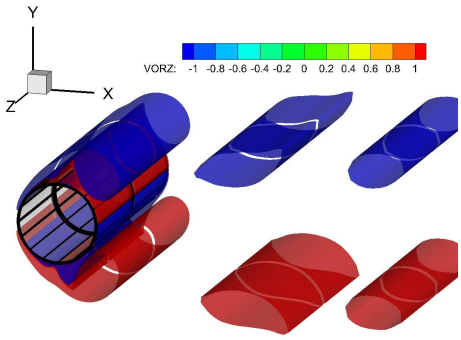

(f) Synchronous at Re = 1000

Figure 7.5: Snapshots of vorticity contours for three dimensional flow at Re = 500 and Re = 1000

7.4 Conclusions

In this work, we have performed three dimensional numerical simulations of an inline vibrating cylinder over a range of amplitudes and frequencies. We have analyzed the lift suppression phenomenon in which the lift goes to zero when the frequency of inline oscillation is close to twice the shedding frequency. We have compared the frequency response curves for two and three dimensional flows and observed a shift in the synchronization maps towards higher frequency ratios/amplitude of oscillations indicating that more energy is required to achieve synchronization in the three-dimensional flow. We have also compared the wake of the synchronous and nonsynchronous regions and attributed the additional energy to achieve lift suppression to the spanwise structures in the wake.

Chapter 8

Piezoelectric Energy Harvesting from Vortex-Induced Vibrations of Circular Cylinder

We investigate the concept of harvesting energy from a circular cylinder undergoing vortex-induced vibrations. The energy is harvested by attaching a piezoelectric transducer to the transverse degree of freedom. We perform numerical simulations for Reynolds numbers (Re) in the range $96 \leq \mathrm{Re} \leq 118$, which covers the pre-synchronization, synchronization, and post-synchronization regimes. We consider the load resistances (R) in the range $500\Omega \leq R \leq 5\mathrm{M}\Omega$. The results show that the load resistance has a significant effect on the oscillation amplitude, lift coefficient, voltage output, and harvested power. The results also show that the synchronization region widens when the load resistance increases. We also find that there is an optimum value of the load resistance for which the harvested power is maximum. This optimum value does not correspond to the case of largest oscillations, which points to the need for a coupled analysis as performed here.

8.1 Introduction

Converting ambient and aeroelastic vibrations to a usable form of electric power has been proposed for powering electronic components, such as microelectromechanical systems, actuators (85; 86), and health monitoring wireless sensors (87–89), or for replacing small batteries that have a finite life span or would require hard and expensive maintenance (90; 91). Different transduction mechanisms can be employed for converting these vibrations to electric power, including electrostatic (39; 40), electromagnetic (41), and piezoelectric (41; 42) transduction. Of particular interest is the piezoelectric option, which has received the most attention because it can be used to harvest energy over a wide range of frequencies (40) and can be easily implemented. To date, most of energy harvesting from mechanical vibrations has concentrated on exploiting base excitations (92–96). More recently, there has been several investigations into the conversion of aeroelastic vibrations into electric power (43–46; 94; 97–99).

When a fluid passes over a cylinder, and vortices are shed at a frequency near the natural frequency of the cylinder, it undergoes high-amplitude oscillations. During this fluid-structure interaction, naturally occuring motion is available, that can be converted by attaching energy harvesting materials. Also, to accurately determine the level of harvested power from vortex-induced vibrations of circular cylinders, one needs to consider the tightly coupling between the mechanical and electrical components of the harvester. This can only be achieved by simultaneously solving the governing equations. In this work, we consider the flow, cylinder's motion and electrical transduction as one single dynamical system. We then perform tightly coupled simulations to determine the level of harvested power from this system under different operating conditions including the Reynolds number and load resistance.

8.2 Mathematical Modeling and Numerical Simulations

8.2.1 Representation and Modeling of the Piezoaeroelastic System

The energy harvester under investigation consists of an elastically-mounted rigid cylinder, which undergoes vortex-induced vibrations in the transverse direction when subjected to an

incoming flow; as shown in the schematic presented in figure 8.1. Including the piezoelectric transducer and considering a load resistance in the electrical circuit (100–102), we add to the flow equations, the equations governing the cylinder displacement, Y, and generated voltage, V, which are written as;

$$M\ddot{Y} + C\dot{Y} + KY - \theta V = F_Y(t), \tag{8.1}$$

$$C_P\dot{V} + \frac{V}{R} + \theta\dot{Y} = 0 \tag{8.2}$$

where M is the mass of the oscillating cylinder per unit length, C and K are used to represent the structural damping and stiffness, respectively, $F_Y(t)$ characterizes the time-dependent excitation of the fluid flow applied on the structure, R is the electrical load resistance, V is the voltage across this load resistance, C_P is the capacitance of the piezoelectric layer, and θ is the electromechanical coupling term. To assess the physics of this system, we consider as an example, a system that has geometric and material properties as presented in Table 8.1. The geometric and material properties of the cylinder are the same as in the experiments of Anagnostopoulos and Bearman (1) which is used to validate the flow solver.

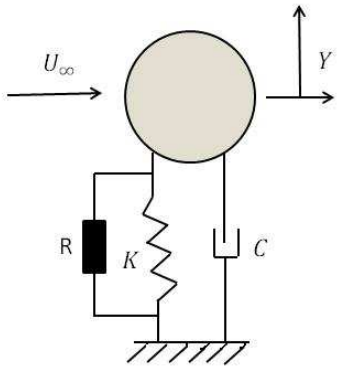

Figure 8.1: A schematic of the proposed cylinder-based piezoaeroelastic energy harvester.

8.2.2 Nondimensionalization and Coupling of the Piezoaeroelastic System

To generalize and solve the coupled problem, we use the diameter of the cylinder D and the incoming free-stream velocity U_∞ as the length and velocity scales. We then rewrite

Table 8.1: Properties of the coupled system.

Physical parameters	Values
Mass of the cylinder per unit length (M) [Kg]	0.2979
Diameter (D) [mm]	1.6
Stiffness per unit length (K) [N/m]	579
Damping per unit length (C) [Ns/m]	0.0325
Damping ratio (ζ)	0.0012
mass ratio (m^*)	149.1
Cylinder oscillation frequency (f_n) [Hz]	7.016
Capacitance (C_p) [nF]	120
Electromechanical coupling (θ) [N/V]	1.55×10^{-3}

equations (8.1) and (8.2) in nondimensional form as

$$\ddot{Y}^* + (\frac{4\pi\zeta}{U_r})\dot{Y}^* + (\frac{2\pi}{U_r})^2 Y^* - (\frac{1}{U_r}^2)V^* = \frac{2}{\pi m^*}C_L, \tag{8.3}$$

$$\dot{V}^* + \sigma_1\dot{Y}^* + \frac{\sigma_2}{U_r}V^* = 0 \tag{8.4}$$

where $Y^* = \frac{Y}{D}$ is the nondimensional transverse cylinder displacement, $U_r = U_\infty/f_n D$ is the reduced velocity, $\zeta = C/C_{crit} = C/2\sqrt{KM}$ is the structural damping ratio, $m^* = \frac{M}{M_f}$ is the mass ratio, $M_f = \frac{1}{4}\rho\pi D^2$ represents the fluid mass per unit length displaced by the cylinder, $V^* = \frac{V}{V_o}$, $V_o = \frac{Mf_n^2 D}{\theta}$, $\sigma_1 = \frac{\theta^2}{MC_P f_n^2}$, $\sigma_2 = \frac{1}{RC_P f_n}$, and f_n is the natural vibration frequency of the rigid cylinder.

The governing electromechanical equations (8.3) and (8.4) can be written as a coupled system of three first-order ordinary-differential equations as

$$\dot{y_1} = y_2 \tag{8.5}$$

$$\dot{y_2} = -(\frac{2\pi}{U_r})^2 y_1 - \frac{4\pi\zeta}{U_r}y_2 + \frac{1}{U_r^2}y_3 + \frac{2}{\pi m^*}C_L \tag{8.6}$$

$$\dot{y_3} = -\sigma_1 y_2 - \frac{\sigma_2}{U_r}y_3 \tag{8.7}$$

where $y_1 = Y^*$, $y_2 = \dot{Y}^*$ and $y_3 = V^*$.

8.2.3 Coupling Scheme

Equations (2.5) and (2.6), which govern the dynamics of the flow field, and equations (8.3) and (8.4), which govern the dynamics of the cylinder and generated voltage are solved in a coupled manner. For that purpose, we use the Hamming fourth-order predictor-corrector technique (20).

In this technique, the fluid load (output of the CFD code-equation-2.8) is coupled to ODEs (equation-8.5-8.7) governing the cylinder's motion and harvested voltage. The predicted state of the cylinder (equation 2.36), based on the fluid load which was computed in the previous time step, is then used in the CFD code to compute the new fluid load (equation-2.8). This new load is then used to compute the new states of the cylinder and voltage using the corrector scheme (equation 2.37). To do so, equations (8.5)-(8.7), are rewritten as equation (2.9) and then integerated by using the numerical integeration scheme discussed in Section 2.4.

8.3 Effect of the Load Resistance on the Onset of Synchronization

Adding a load resistance results in a variation of the natural frequency and damping of the coupled system. Because the onset of the synchronization region is defined by matching the natural frequency of the coupled electromechanical system with the frequency of the vortex-induced vibration, we perform, as a first step, a linear analysis to determine the variations in the natural frequency and damping that are due to adding the load resistance. As such, we consider the electromechanical governing equations of the cylinder, which are rewritten as

$$M\ddot{Y} + C\dot{Y} + KY - \theta V = 0 \tag{8.8}$$

$$C_P\dot{V} + \frac{V}{R} + \theta\dot{Y} = 0 \tag{8.9}$$

we rewrite equations (8.8) and (8.9) as the following set of first-order differential equations:

$$\dot{X}_1 = X_2, \tag{8.10}$$

$$\dot{X}_2 = -(2\pi f_n)^2 X_1 - 4\pi f_n \zeta X_2 + \frac{\theta}{M} X_3, \tag{8.11}$$

$$\dot{X}_3 = -\frac{\theta}{C_p} X_2 - \frac{1}{C_p R} X_3 \tag{8.12}$$

where $X_1 = Y$, $X_2 = \dot{Y}$ and $X_3 = V$.

Equations (8.10)-(8.12) can be expressed in vector form as

$$\dot{\mathbf{X}} = \mathbf{A}(R)\mathbf{X} \tag{8.13}$$

where

$$\mathbf{A}(R) = \begin{pmatrix} 0 & 1 & 0 \\ -(2\pi f_n)^2 & -4\pi f_n \zeta & \frac{\theta}{M} \\ 0 & -\frac{\theta}{C_p} & -\frac{1}{C_p R} \end{pmatrix}$$

and

$$\mathbf{X} = \begin{pmatrix} X_1 \\ X_2 \\ X_3 \end{pmatrix}$$

Variations of the real and imaginary parts of the eigenvalue k_i of the linear electromechanical coupled system are shown in figure 8.2. It is clear from figure 8.2(a) that, for the considered parameters of the coupled system, the global natural frequency remains almost constant, with a value near 44.05 rad/s, for small values of the load resistance $R < 30\text{K}\Omega$. This value of the global natural frequency ($R = 100\Omega$) is referred as the short global frequency. For large values of R, the global natural frequency becomes equal to 44.8 rad/s. This value of the global natural frequency ($R = 10\text{M}\Omega$) is referred to the open global frequency. The plot in figure 8.2(b) shows that the electromechanical damping remains very low for small values of the load resistance, increases to a maximum for load resistance values of nearly 200KΩ, and then decreases and remains low for larger values of the load resistance. This maximum value in the coupled electromechanical damping is due to the resistive shunt damping effect. This analysis shows that the load resistance impacts the natural frequency and damping of the coupled electromechanical system. The impact of these variations in both of the frequency and damping on the system outputs is discussed further in Section 8.4.2.

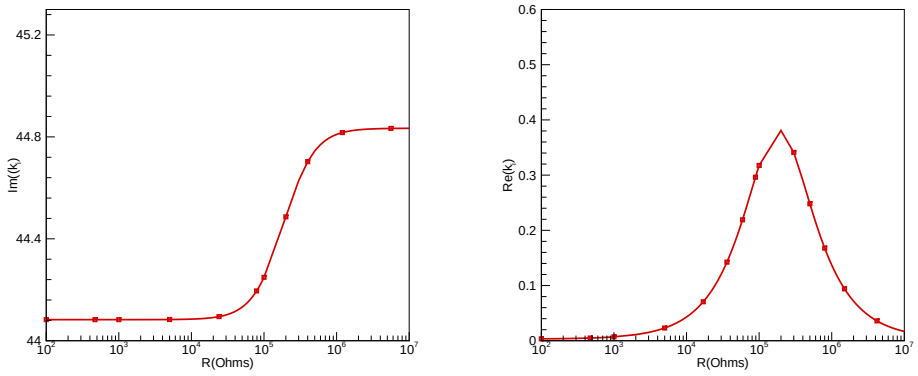

(a) (b)

Figure 8.2: Variations of the real k_r and imaginary k_i parts of the eigenvalue k of the linear system with the load resistance

8.4 Results and Discussion

8.4.1 Effect of Reynolds Number on the System Outputs

To investigate harvesting energy from the considered piezoaeroelastic system, we perform numerical simulations of the flow over a rigid cylinder that moves in the cross-flow direction and has a piezoelectric transducer attached to this direction. As the ultimate goal is to power small sensors and actuators, we limit this study to a Reynolds number in the range $96 \leq \mathrm{Re} \leq 118$, which corresponds to a cylinder having a diameter ranging from 0.1 mm to 1.6 mm and placed in a water stream of $0.96\ m/sec \leq U_\infty \leq 1.18\ m/sec$ and/or $0.06\ m/sec \leq U_\infty \leq 0.07375\ m/sec$. This range corresponds to reduced velocities in the range $5.34 \leq U_r \leq 6.57$. Note that, for all cases the flow over a stationary cylinder was initially computed for the same Reynolds number. Then, the cylinder was allowed to move and the frequency of vortex shedding (f_{vs}), the cylinder oscillation frequency, the voltage output, and the harvested power are recorded, after reaching steady state.

We conducted numerical simulations for a wide range of load resistances. The same tendency in the system outputs was observed over the whole range. To present the important

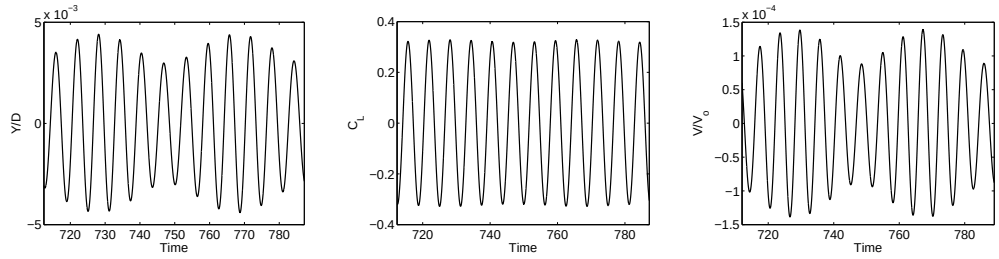

(a) Pre-Synch. (Re = 96) (b) Pre-Synch. (Re = 96) (c) Pre-Synch. (Re = 96)

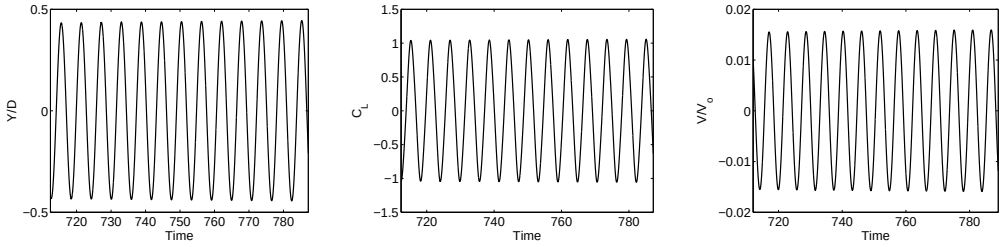

(d) Synchronous (Re = 104) (e) Synchronous (Re = 104) (f) Synchronous (Re = 104)

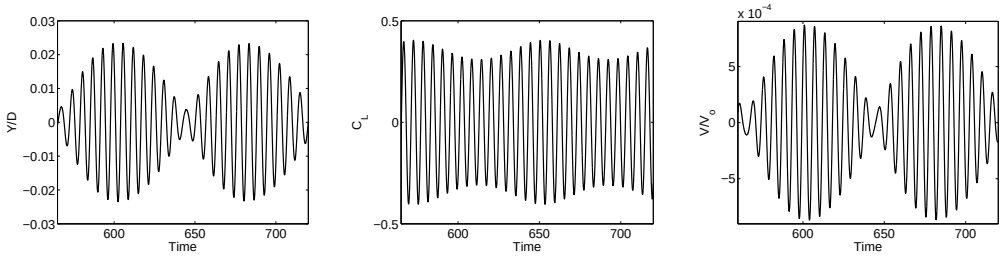

(g) Post-Synch.(Re = 116) (h) Post-Synch.(Re = 116) (i) Post-Synch.(Re = 116)

Figure 8.3: Time histories of the transverse displacement, fluctuating lift coefficient, and voltage output for the pre-synchronous (a,b,c), synchronous (d,e,f), and post-synchronous (g,h,i) regimes, respectively, when the load resistance $R = 5\text{K}\Omega$.

physical observations, we consider the response of the cylinder and the level of generated voltage for $R = 5\text{K}\Omega$ while varying the Reynolds number. In figure 8.3, we show time

histories of the cylinder displacement, lift coefficient, and associated voltage output for the pre-synchronous, synchronous, and post-synchronous regimes. In the pre-synchronous regime (Re = 96), the cylinder oscillations remain very low ($\frac{Y}{D} \sim 10^{-3}$), as shown in figure 8.3(a). The lift coefficient, presented in figure 8.3(b), oscillates around a zero mean with a peak value of 0.325. The response in this regime is quasi-periodic consisting of two major frequencies, the shedding frequency and the cylinder global frequency. The voltage output in figure 8.3(c) shows that, as expected, its time history follows very closely that of the displacement. Similar values for the displacement, lift, and voltage are observed for Reynolds numbers up to Re = 104. At Re = 104, high oscillation amplitudes of the cylinder are observed. Time histories of the cylinder displacement, lift coefficient, and voltage output at Re = 104 are shown in Figs. 8.3(d), 8.3(e), and 8.3(f), respectively. These plots show periodic responses with a dominant frequency, which is the cylinder natural frequency. These large oscillation amplitudes extend up to Re = 114. This is due to the fact that the range from Re = 104 to Re = 114 corresponds to the synchronization regime at $R = 5\text{K}\Omega$. At Re = 116, the synchronization phenomenon bifurcates, a high level of modulation is observed in the time histories of the displacement and voltage, as shown in Figs. 8.3(g) and 8.3(i). Modulations also exist in the time history of the lift coefficient presented in figure 8.3(h). For all considered cases, we note that the time histories of the transverse displacement and harvested voltage have the same trend. This is expected because the generated voltage is directly related to the transverse displacement through the Gauss law (equation 8.9).

Further insight into the different aspects of the displacement and lift coefficient can be obtained from the power spectra of their time histories, as shown in figure 8.4. When Re = 96, in the pre-synchronous regime, figure 8.4(a) shows two spectral peaks: one peak at 0.1602, which is the vortex shedding frequency, and a smaller one at 0.185, which corresponds to the cylinder global natural frequency. Here, it can be inferred that the response is quasi-periodic and is not synchronized with the cylinder global frequency. In the synchronous regime (Re = 104), figure 8.4(b) shows that both of the lift and displacement have the same oscillation frequency. Moreover, the vortices are shed at the cylinder global natural frequency (i.e., $f_{vs} \cong f_c$), indicating that synchronization has taken place as the two frequencies have merged. In the post-synchronous regime, (Re = 116), figure 8.4(c) shows three dominant peaks:

the vortex shedding frequency ($f_{vs} = 0.1669$) and two asymmetric sidebands, indicating an amplitude and phase modulated response.

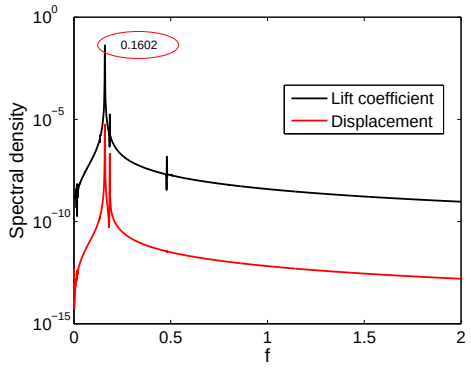

(a) Pre-synch. (Re = 96)

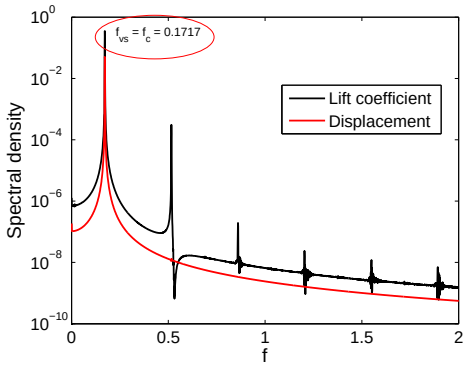

(b) VIV-Synch. (Re = 104)

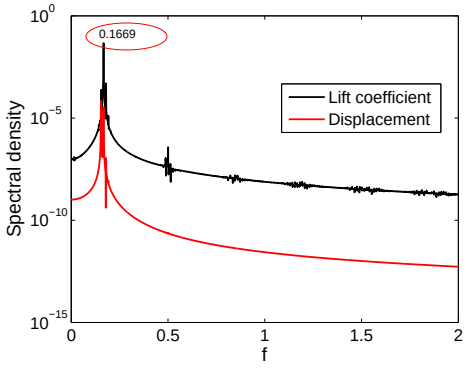

(c) Post-synch. (Re = 116)

Figure 8.4: Power spectra of (a) pre-synchronous, (b) synchronous, and (c) post-synchronous regimes for an oscillating cylinder in the cross-flow direction at the specified Reynolds number when $R = 5\text{K}\Omega$.

8.4.2 Effect of the Load Resistance on the System Outputs

Numerical simulations are performed for different values of the electrical load resistances over a range of Reynolds numbers that covers the pre-synchronous, synchronous, and post-

synchronous regimes. Figure 8.5(a) shows variations of the root mean square (rms) amplitudes of the cylinder oscillations with the Reynolds number and load resistance. The plot shows that the synchronization phenomenon starts for all load resistances at about the same Reynolds number (i.e., Re = 104). This is due to the fact that the system overall global frequency does not change appreciably with the load resistance (see figure 8.2(a)). However, it is important to note that the synchronized amplitude of the cylinder oscillations varies significantly with the load resistance. The amplitude of oscillations is high for small values of the load resistance with a maximum value of $\frac{Y_{rms}}{D} = 0.3229$ for $R = 5\text{K}\Omega$. This amplitude decreases to 0.0901 for $R = 100\text{K}\Omega$ and increases again to 0.3107 for $R = 5\text{M}\Omega$. For $R = 100\text{K}\Omega$, the amplitude of cylinder oscillations are the smallest ones compared to the rest of the considered load resistances. This is due to the fact that maximum value of the coupled electromechanical damping is obtained at this load resistance, as shown in the linear analysis performed in Section 8.3 (see figure 8.2(b)). Variations of the rms fluctuating lift coefficient with the Reynolds number and load resistances are shown in figure 8.5(b). The plot shows that the behavior of the lift coefficient is qualitatively similar to that of the cylinder oscillation amplitude. In fact, smaller values of the fluctuating lift coefficient are obtained for $R = 100\text{K}\Omega$ and $R = 500\text{K}\Omega$. On the other hand, we note the possibility of antiresonance occuring after the resonance peak in terms of Reynolds number for load resistance values equal to 100KΩ, 500KΩ and 5MΩ.

Variations of the root mean square values of the voltage with the Reynolds number for different values of the electrical load resistance are shown in figure 8.6(a). This figure shows that, for all considered load resistances, the voltage output increases as the electrical load resistance increases. The maximum voltage is attained when the Reynolds number reaches Re = 104. Above this Reynolds number, the voltage remains almost constant over the whole synchronization regime. It is also interesting to note that, by increasing the load resistance, the synchronization regime is slightly expanded to cover higher Reynolds numbers. For example, for the load resistance $R = 500\Omega$, synchronization starts at the critical value Re = 104 and extends to Re = 112. In contrast, for $R = 5\text{M}\Omega$, synchronization starts at the same critical value Re = 104 but extends to Re = 114. At Re = 116, the voltage is low. Still, the voltage in this regime (post-synchronous regime) is relatively higher in comparison to that

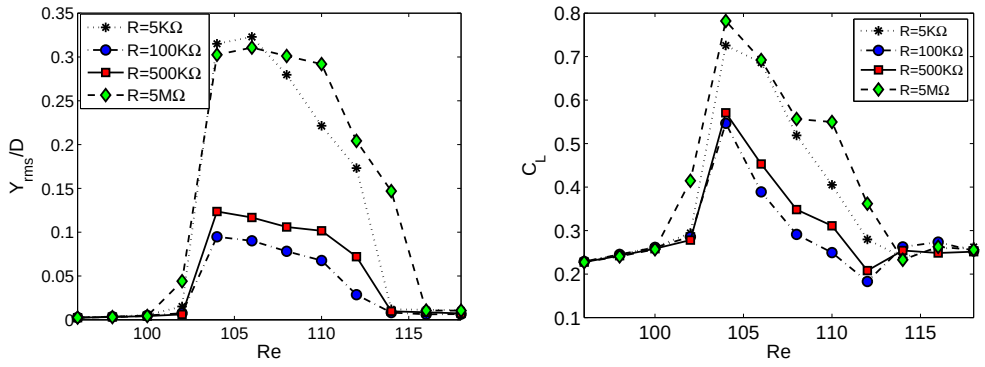

(a) cylinder's displacement (b) lift coefficient

Figure 8.5: Variations of the cylinder displacement ($\frac{Y_{rms}}{D}$) and lift coefficient (C_L) with the Reynolds number for different load resistances.

in the pre-synchronous regime. This behavior is clearly shown in figure 8.6(b), where the rms values of the voltage are plotted as a function of the load resistance. In this figure, the voltage output is plotted for the pre-synchronous, synchronous, and post-synchronous regimes. For the sake of discussion, we plot only two values from each regime for all considered resistances. Figure 8.6(b) shows that the generated voltages at the Reynolds numbers Re = 96 and Re = 100, which are part of the pre-synchronous regime, are smaller than the corresponding values in the post-synchronous regime (i.e., Re = 114 and 116) for all load resistances. However, the voltage output is the largest in the synchronous regime (i.e., Re = 104 and 106). Figure 8.6(b) also shows that the voltage is larger at higher values of the load resistance. However, the rate of increase is smaller for $R \geq 500\text{K}\Omega$. Similar observations have been made in the literature of piezoelectric energy harvesting from ambient vibrations (based on cantilever beams) (100) and from aeroelastic vibrations (based on wings) (94; 100).

Figure 8.7(a) shows variations of the harvested power with the Reynolds number for different values of the electrical load resistance. The generated power is computed from the voltage according to the following relation:

$$P_{avg} = \frac{V_{rms}^2}{R} \tag{8.14}$$

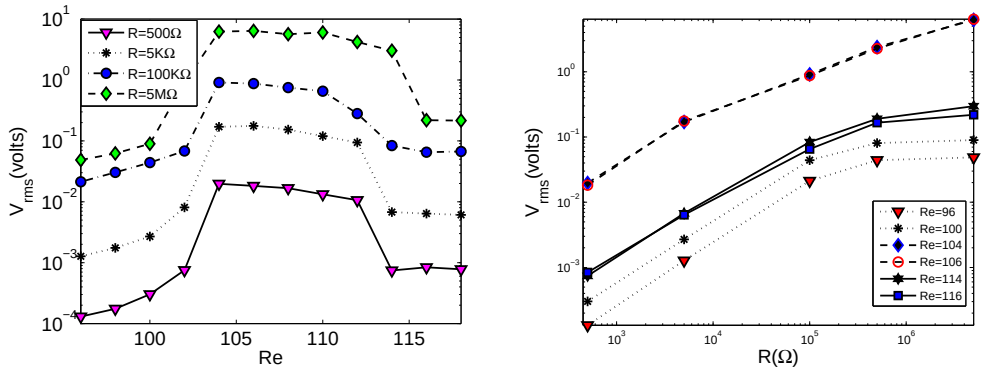

(a) (b)

Figure 8.6: Variations of the voltage output with the (a) Reynolds number and (b) load resistance.

where V_{rms} is the rms value of the voltage output and R is the electrical load resistance across the piezoceramic layer. Figure 8.7(a) shows that the highest levels of harvested power are obtained in the synchronization region for all considered load resistances. However, unlike the voltage output, the harvested power achieves a maximum and then decreases when using higher load resistances. This behavior is clear from figure 8.7(b), where the harvested power is plotted as a function of the load resistance. The plot shows that the harvested power increases as the electrical load increases from $R = 500\Omega$ to $R = 100\text{K}\Omega$. When the value of the load resistance is set equal to $R = 500\text{K}\Omega$, the harvested power starts to decrease. Here, the maximum power is harvested at $R = 500\text{K}\Omega$. Of interest, however, is the fact that, for this optimum resistance, the electromechanical damping is also maximum (see figure 8.2(b)) due to shunt damping effect, this translates into lower amplitudes of the cylinder oscillations (see figure 8.5(a)). This means that the largest oscillations do not lead to maximum generated power, as one would expect from a non-coupled analysis. The existence of an optimum value for the load resistance for which the highest levels of harvested power are obtained has been observed in the literature of piezoelectric energy harvesting from ambient vibrations (based on cantilever beams)(97) and from aeroelastic vibrations (based on wings) (94; 100).

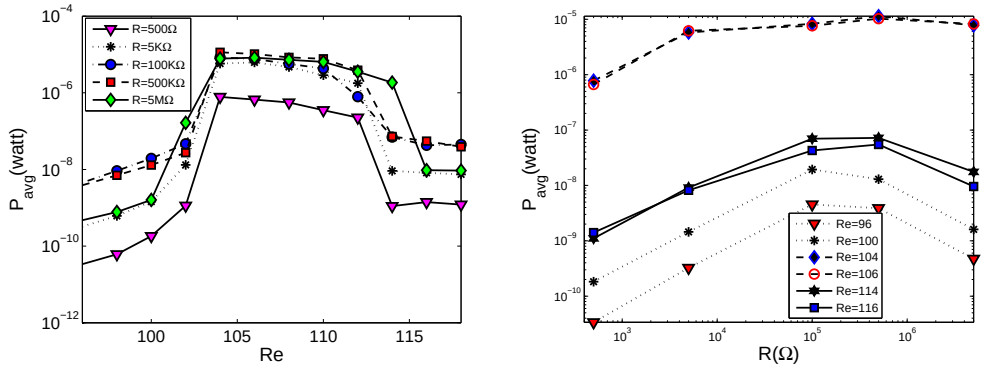

(a) (b)

Figure 8.7: Variations of the harvested power with the (a) Reynolds number and (b) load resistance.

8.5 Conclusions

We have performed numerical simulations to investigate energy harvesting from vortex-induced vibrations of a circular cylinder. The simulations were performed for a range of Reynolds numbers that covers the pre-synchronization, synchronization, and post-synchronization regimes. The effect of the load resistance on the harvester response have been analyzed. Based on the linear analysis, we have found that the load resistance impacts the onset of synchronization because it affects the global frequency and damping of the electromechanical system. The results also show that the voltage output continuously increases when increasing the load resistance. In contrast, there is an optimum value of the electrical load resistance for which the level of the harvested power is maximum. This value does not correspond to the largest cylinder oscillations, which shows the need for a coupled analysis.

Chapter 9

Conclusions and Future Recommendations

9.1 Conclusions

The research in this dissertation is motivated to understand the phenomena of fluid-structure interactions resulting in vortex-induced vibrations. The behavior of a structure undergoing VIV depends mainly on the natural frequency of the structure and vortex shedding frequency. If the frequency of the vortex shedding is close to a natural frequency of the body, the body will start to oscillate with high amplitudes, which may lead to structural failure of the body. The main features of this dissertation can be categorized in three aspects (i) development of a three-dimensional parallel CFD solver capable of simulating the flow past a freely oscillating circular cylinder (ii) suppressing the resulting vibrations using active and/or passive controllers, and (iii) converting the naturally occuring vortex induced vibrations into a usable form of electric power. In this chapter, we summarize our results and present concluding remarks.

1. We have developed and validated a parallel CFD code, in which the incompressible continuity and unsteady Navier-Stokes equations are solved using an accelerated reference frame technique. The code solves the flow field over a freely oscillating circular cylinder. We also employed the Hamming fourth-order predictor-corrector technique to

account for the interaction between the fluid load and the cylinder motion.

2. We have investigated the effects of different initial conditions around the bifurcation point. We found an unstable region at both ends of the synchronization regime, depending on the initial displacement/velocity of the cylinder. We observed a periodic response within the synchronization regime. However, we observed period-n (where n > 1), quasiperiodic and chaotic responses outside the synchronization regime.

3. We have investigated the effectiveness of linear and nonlinear velocity feedback controllers to suppress high-amplitude oscillations of an elastically-mounted rigid cylinder. The results show that, for relatively allowed large controlled amplitudes, the linear velocity feedback controller is more efficient. On the other hand, for very small controlled amplitudes, the cubic velocity feedback controller is more efficient.

4. We have investigated in detail the feasibility of using a nonlinear energy sink (NES) to control the vortex-induced vibrations of a freely oscillating circular cylinder. We varied the mass of the NES and its damping and also varied in a limited way the initial conditions of the system from zero values. The results show a significant shortcoming in having multiple solutions including periodic, two-period quasiperiodic, and period-doubled steady-state responses (attractors) that depend on the initial conditions of the cylinder.

5. We have investigated drag reduction through rotational oscillations of a circular cylinder. We have found that the mean drag is decreased at higher forcing frequencies. The results also showed there is a threshold of a rotational oscillation amplitude below which the mean drag does not decrease for any excitation frequency.

6. We have performed an analysis of the lift suppression phenomenon through forced inline oscillations of the cylinder. We have observed a shift in the synchronization maps towards higher frequency ratios/amplitude of oscillations indicating that more energy is required to achieve synchronization in the three-dimensional flow.

7. We have investigated the concept of energy harvesting from vortex-induced vibrations of a circular cylinder. The results showed there is an optimum value of the electrical

load resistance for which the level of the harvested power is maximum. This value corresponds to the minimum value of the cylinder's displacement which shows the electrical and mechanical components of the system are tightly coupled.

9.2 Recommendations for Future Work

As a continuation of this effort, one should consider, the capability of the CFD code which could be enhanced by considering the cylinder's combined motion (i.e., crossflow and inline). Also, flow control concepts which include injection/suction on the rear surface of the cylinder could be investigated. The rate of blowing/suction and the proper location of these controls is an active research field. Also in order to model, predict, and control vortex shedding, full simulation of the coupled flow and structure equations is needed. This involves accounting for three-dimensional effects, turbulence structures, and elasticity, among other considerations. The capability of CFD solver could be enhanced by resolving the turbulent structures and control the VIV of the circular cylinder at much higher Reynolds number.

Bibliography

[1] Anagnostopoulos, P. and Bearman, P. W., "Response characteristics of a vortex-excited cylinder at low Reynolds numbers," *Journal of Fluids and Structures*, Vol. 6, 1992, pp. 39–50.

[2] Yang, J., Preidikman, S., and Balaras, E., "A strongly coupled, embedded-boundary method for fluid-structure interactions of elastically mounted rigid bodies," *Journal of Fluids and Structures*, Vol. 24, 2008, pp. 167–182.

[3] Schulz, K. W. and Kallinderis, Y., "Unsteady flow structure interaction for incompressible flows using deformable hybrid grids," *Journal of Computational Physics*, Vol. 143, 1998, pp. 569–597.

[4] Choi, S. and Choi, H., "Characteristics of flow over a rotationally oscillating cylinder at low Reylolds number," *Physics of Fluids*, Vol. 14, 2002, pp. 2767–2777.

[5] Protas, B. and Wesfried, J. E., "Drag force in the open-loop control of the cylinder wake in the laminar regime," *Journal of Fluid Mechanics*, Vol. 14, 2002, pp. 810–826.

[6] Tanida, Y., Okajima, A., and Watanabe, Y., "Stability of a circular cylinder oscillating in uniform flow or in a wake," *Journal of Fluid Mechanics*, Vol. 61, 1973, pp. 769–784.

[7] Marzouk, O. A. and Nayfeh, A. H., "Reduction of the loads on a cylinder undergoing harmonic in-line motion," *Physics of Fluids*, Vol. 21, 2009, pp. 083103.

[8] Williamson, C. H. K., "Vortex dynamics in the cylinder wake," *Annual Review of Fluid Mechanics*, Vol. 28, 1996, pp. 477–539.

[9] Bearman, P. W., "Vortex shedding from oscillating bluff bodies," *Annual Review of Fluid Mechanics*, Vol. 16, 1984, pp. 195–222.

[10] Williamson, C. H. K. and Govardhan, R., "Vortex-Induced Vibrations," *Annual Review of Fluid Mechanics*, Vol. 36, 2004, pp. 413–455.

[11] Gabbai, R. D. and Benaroya, H., "An overview of modeling and experiments of vortex-induced vibration of circular cylinder," *Journal of Sound and Vibration*, Vol. 282, 2005, pp. 575–616.

[12] Roshko, A., "On the wake and drag of bluff bodies," *Journal of the aeronautical sciences*, Vol. 22, No. 2, 1955, pp. 124–132.

[13] Roshko, A., "On the development of turbulent wakes from vortex streets," *NACA Rep. 1191*, Vol. (unpublished), 1954.

[14] Bishop, R. and Hassan, A., "The Lift and Drag Forces on a Circular Cylinder in Flowing Fluid," *Proceedings of the Royal Society Series A*, Vol. 277, 1963, pp. 32–50.

[15] Karniadakis, G. E. and Triantafyllou, G. S., "Three-dimensional dynamics and transition to turbulence in the wake of bluff objects," *Journal of Fluid Mechanics*, Vol. 238, 1992, pp. 1–30.

[16] Williamson, C. H. K. and Roshko, A., "Vortex formation in the wake of an oscillating cylinder," *Journal of Fluids and Structures*, Vol. 2, 1988, pp. 355–381.

[17] Jauvtis, N. and Williamson, C. H. K., "The effect of two degrees of freedom on vortex-induced vibration at low mass and damping," *Journal of Fluid Mechanics*, Vol. 509, 2004, pp. 23–62.

[18] Anagnostopoulos, P., "Numerical investigation of response and wake characteristics of a vortex-excited cylinder in a uniform stream," *Journal of Fluids and Structures*, Vol. 8, 1994, pp. 367–390.

[19] Blackburn, H. M. and Henderson, R., "Lock-in behavior in simulated vortex-induced vibration," *Experimental thermal and fluid science*, Vol. 12, 1996, pp. 184–189.

[20] Carnahan, B., Luther, H. A., and Wilkes, J. O., *Applied Numerical Methods*, Wiley, New York, 1969.

[21] Blevins, R. D., "The effect of sound on vortex shedding from cylinders," *Journal of Fluid Mechanics*, Vol. 161, 1985, pp. 217–237.

[22] el Hak, M. G., *Flow Control: Passive, Active and Reactive Flow Management*, Cambridge University Press, 2000.

[23] H. Choi, W.-P. J. and Kim, J., "Control of flow over a bluff body," *Annual Review of Fluid Mechanics*, Vol. 40, 2008, pp. 113–139.

[24] Akhtar, I., *Parallel Simulations, Reduced-Order Modeling, and Feedback Control of Vortex Shedding using Fluidic Actuators*, Ph.D. thesis, Virginia Tech, Blacksburg, VA, 2008.

[25] Baz, A. and Ro, J., "Active control of flow-induced vibrations of a flexible cylinder using direct velocity feedback," *Journal of Sound and Vibration*, Vol. 146, 1991, pp. 33–45.

[26] Williams, J. E. F. and Zhao, B. C., "The active control of vortex shedding," *Journal of Fluids and Structures*, Vol. 3, 1988, pp. 115–122.

[27] Huang, X., "Feedback control of vortex shedding from a circular cylinder," *Experiments in Fluids*, Vol. 20, 1996, pp. 218–224.

[28] Mehmood, A., Abdelkefi, A., Akhtar, I., Nayfeh, A., Nuhait, A., and Hajj, M., "Linear and nonlinear active feedback controls for vortex-induced vibrations of circular cylinders," *Journal of Vibration and Control*, 2012, pp. "DOI: 10.1177/1077546312469425".

[29] Zdravkovich, M. M., "Review and classification of various aerodynamic and hydrodynamic means for suppressing vortex shedding," *Journal of Wind Engineering and Industrial Aerodynamics*, Vol. 7, 1981, pp. 145–189.

[30] Walshe, D. E. and Wootton, L. R., "Preventing wind-induced oscillations of structures of circular section," *Proceedings of the Institution of Civil Engineers*, Vol. 47, 1979, pp. 1–24.

[31] Lofty, A. and Rockwell, D., "The near-wake of an oscillating trailing edge;Mechanisms of periodic and aperiodic response," *Journal of Fluid Mechanics*, Vol. 251, 1993, pp. 173.

[32] Tokumaro, P. T. and Dimotakis, P. E., "Rotary oscillation control of a cylinder wake," *Journal of Fluid Mechanics*, Vol. 224, 1991, pp. 77–90.

[33] Shiels, D. and Leonard, A., "Investigation of a drag reduction on a circular cylinder in rotary oscillation," *Journal of Fluid Mechanics*, Vol. 431, 2001, pp. 297–322.

[34] Thiria, B., Goujon-Durand, and Wesfried, J. W., "The wake of a cylinder performing rotary oscillations," *Journal of Fluid Mechanics*, Vol. 560, 2006, pp. 123.

[35] Kwon, K. and Choi, H., "Control of laminar vortex shedding behind a circular cylinder using splitter plates," *Physics of Fluids*, Vol. 8, 1996, pp. 479.

[36] Unal, M. F. and Rockwell, D., "On vortex formation from a cylinder. Part 2. Control by splitter-plate interference," *Journal of Fluid Mechanics*, Vol. 190, 1988, pp. 513.

[37] Tumkur, R. K. R., Calderer, R., Masud, A., Bergman, L. A., Pearlstein, A. J., and Vakakis, A. F., "Passive suppression of laminar vortex induced vibration of a circular cylinder," ENOC 2011, 24-29 July, 2011.

[38] Tumkur, R. K. R., Domany, E., Gendelman, O. V., Masud, A., Bergman, L. A., and Vakakis, A. F., "Reduced-order model for laminar vortex-induced vibration of a rigid circular cylinder with an internal nonlinear absorber," *Journal of Commun. Nonlinear Sci. Numer. Simulat.*, Vol. 18, 2013, pp. 1916–1930.

[39] Arnold, D., "Review of microscale magnetic power generation," *IEEE Trans. Magn.*, Vol. 43, 2007, pp. 3940–3951.

[40] Mitcheson, P., Miao, P., Start, B., Yeatman, E., Holmes, A., and Green, T., "MEMS electrostatic micro-power generator for low frequency operation," *Sensors and Actuators A: Physical*, Vol. 115, 2004, pp. 523–529.

[41] Anton, S. R. and Sodano, H. A., "A review of power harvesting using piezoelectric materials (2003-2006)," *Smart Materials and Structures*, Vol. 16, 2007, pp. 1–21.

[42] Cook-Chennault, K. A., Thambi, N., and Sastry, A. M., "Powering MEMS portable devices–a review of non-regenerative and regenerative power supply systems with emphasis on piezoelectric energy harvesting systems," *Smart Materials and Structures*, Vol. 17, 2008, pp. 043001.

[43] Bryant, M. and Garcia, E., "Energy harvesting: a key to wireless sensor nodes," *Proceeding SPIE*, Vol. 7493, 2009, pp. 74931W.

[44] Abdelkefi, A., Hajj, M. R., and Nayfeh, A., "Sensitivity analysis of piezoaeroelastic energy harvesters," *Journal of Intelligent Material Systems and Structures*, Vol. 23, 2012, pp. 1523–1531.

[45] Abdelkefi, A., Yan, Z., and Hajj, M. R., "Modeling and nonlinear analysis of piezoelectric energy harvesting from transverse galloping," *Smart Materials and Structures*, Vol. 22, 2013, pp. 025016.

[46] Abdelkefi, A., Hajj, M., and Nayfeh, A., "Power harvesting from transverse galloping of square cylinder," *Nonlinear Dynamics*, Vol. 70, 2012, pp. 1377–1388.

[47] Hirt, C. W., Amsden, A. A., , and Cook, J. L., "An arbitrary Lagrangian-Eulerian computing method for all flow speeds," *Journal of Computational Physics*, Vol. 14, 1974, pp. 227–253.

[48] Mittal, R. and Iaccarino, G., "Immersed Boundary Methods," *Annual Review of Fluid Mechanics*, Vol. 37, 2005, pp. 239–261.

[49] Blackburn, H. M. and Henderson, R., "A study of two-dimensional flow past an oscillating cylinder," *Journal of Fluid Mechanics*, Vol. 255, 1999, pp. 1385.

[50] Blackburn, H. M., "Computational bluff body fluid dynamics and aeroelasticity," *N.G. Barton, J. Periaux (Eds.), Coupling of Fluids, Structures and Waves Problems in Aeronautics, Notes on Numerical Fluid Mechanics and Multidisciplinary Design (NNFM)*, Vol. 85, 2003, pp. 10–23.

[51] Zang, Y., Street, R., and Koseff, J., "A Non-staggered Grid, Fractional Step Method for Time-Dependent Incompressible Navier-Stokes Equations in Curvilinear Coordinates," *Journal of Computational Physics*, Vol. 114, 1994, pp. 18–33.

[52] Leonard, B. P., "A stable and accurate convective modeling procedure based on quadratic upstream interpolation," *Computational Methods in Applied Mechanical Engineering*, Vol. 19, 1979, pp. 59–98.

[53] Akhtar, I., Nayfeh, A. H., and Ribbens, C. J., "On the Stability and Extension of Reduced-Order Galerkin Models in Incompressible flows: A Numerical Study of Vortex Shedding," *Theoretical and Computational Fluid Dynamics*, Vol. 23, No. 3, 2009, pp. 213–237.

[54] Mehmood, A., Abdelkefi, A., Hajj, M., Nayfeh, A., Akhtar, I., and Nuhait, A., "Piezoelectric energy harvesting from vortex-induced vibrations of circular cylinder," *Journal of Sound and Vibration*, Vol. 332, No. 19, 2012, pp. 4656–4667.

[55] Feng, C. C., *The measurement of vortex-induced effects in flow past stationary and oscillating circular and D-section cylinders*, Ph.D. thesis, Univ. Br. Columbia, Vancouver., 1968.

[56] Govardhan, R. and Williamson, C. H. K., "Defining the 'modified Griffin plot' in vortex-induced vibration: revealing the effect of Reynolds number using controlled damping," *Journal of Fluid Mechanics*, Vol. 561, 2006, pp. 147–180.

[57] Jiang, X., Mcfarland, D. M., Bergman, L. A., and Vakakis, A. F., "Steady state passive nonlinear pumping in coupled oscillators: theoretical and experimental results," *Nonlinear Dynamics*, Vol. 33, 2003, pp. 87–102.

[58] Vakakis, A. F., Mcfarland, D. M., Bergman, L., Manevitch, L., and Gendelman, O., "Passive vibration control by nonlinear energy pumping," *IUTAM symposium on chaotic dynamics and control of systems and processes in mechanics*, 2005.

[59] Mcfarland, D. M., Bergman, L., and Vakakis, A. F., "Experimental study of non-linear

energy pumping occuring at a single fast frequency," *International Journal of Non-Linear Mechanics*, Vol. 40, 2005, pp. 891899.

[60] Gendelman, O. V., Gourdon, E., and Lamarque, C. H., "Quasiperiodic energy pumping in coupled oscillators under periodic forcing," *Journal of Sound and Vibration*, Vol. 294, 2006, pp. 651–662.

[61] Gourdon, E., Alexander, N. A., Taylor, C. A., Lamarque, C. H., and Pernot, S., "Nonlinear energy pumping under transient forcing with strongly nonlinear coupling: Theoretical and experimental results," *Journal of Sound and Vibration*, Vol. 300, 2007, pp. 522–551.

[62] Roberson, R. E., "Synthesis of a nonlinear dynamic vibration absorber," *Journal of the Franklin Institute*, Vol. 254, 1952, pp. 205–220.

[63] Gendelman, O. V., "Transition of energy to a nonlinear localized mode in a highly asymmetric system of two oscillators," *Nonlinear Dynamics*, Vol. 25, 2001, pp. 237–253.

[64] Gourdon, E. and Lamarque, C. H., "Energy pumping for a larger span of energy," *Journal of Sound and Vibration*, Vol. 285, 2005, pp. 711–720.

[65] Vakakis, A. F., Manevitch, L. I., Gendelman, O., and Bergman, L., "Dynamics of linear discrete systems connected to local, essentially non-linear attachments," *Journal of Sound and Vibration*, Vol. 264, 2003, pp. 559–577.

[66] Rice, H. J. and McCraith, J. R., "Practical non-linear vibration absorber design," *Journal of Sound and Vibration*, Vol. 116.

[67] Lee, Y. S., Kerschen, G., Vakakis, A. F., Panagopoulos, P., Bergman, L., and Mcfarland, D. M., "Complicated dynamics of a linear oscillator with a light, essentially nonlinear attachment," *Physica D*, Vol. 204, 2005, pp. 41–69.

[68] Kerschen, G., Lee, Y. S., Vakakis, A. F., Mcfarland, D. M., and Bergman, L. A., "Irreversible passive energy transfer in coupled oscillators with essential nonlinearity," *SIAM J. Appl. math*, Vol. 66, 2006, pp. 648–679.

[69] Gendelman, O. V., Gorlov, D. V., Manevitch, L. I., and Musienko, A. I., "Dynamics of coupled linear and essentially nonlinear oscillators with susstantially different masses," *Journal of Sound and Vibration*, Vol. 286, 2005, pp. 1–19.

[70] Malatkar, P. and Nayfeh, A. H., "Steady-state dynamics of a linear structure weakley coupled to an essentially nonlinear oscillator," *Nonlinear Dynamics*, Vol. 47, 2007, pp. 167179.

[71] Vakakis, A. F. and Bergman, L. A., "Rebuttal of "steady state dynamics of a linear structure weakly coupled to an essentially nonlinear oscillator" by P. Malatkar and A. H. Nayfeh," *Nonlinear Dynamics*, Vol. 53, 2008, pp. 167–168.

[72] Vakakis, A. F. and Bergman, L. A., "P. Malatkar and A. H. Nayfeh, "Authors' response to the rebuttal by A. F. Vakakis and L. A. Bergman of Steady state dynamics of a linear structure weakly coupled to an essentially nonlinear oscillator, Vol.47, 2007, pp. 167-179," *Nonlinear Dynamics*, Vol. 53, 2008, pp. 169–171.

[73] Min, C. and Choi, H., "Suboptimal feedback control of vortex shedding at low Reynolds numbers," *Journal of Fluid Mechanics*, Vol. 401, 1999, pp. 123–156.

[74] He, J., Watson, L. T., and Sosonkina, M., "Algorithm 897: VTDIRECT95: serial and parallel codes for the global optimization algorithm DIRECT," *ACM Transactions on Mathematical Software (TOMS)*, Vol. 36, 2009, pp. 1–24.

[75] He, J., Verstak, A., Watson, L. T., and Sosonkina, M., "Performance Modeling and Analysis of a Massively Parallel DIRECT—Part 1," *International Journal of High Performance Computing Applications*, Vol. 23, 2009, pp. 14–28.

[76] Jones, D. R., Pertunen, C. D., and Stuckman, B. E., "Lipschitzian optimization without the Lipschitz constant," *Journal Optimization Theory and Applications*, Vol. 79, 1963, pp. 157–181.

[77] Mittal, R. and Balachandar, S., "Effect of three-dimensionality on the lift and drag of nominally two-dimensional cylinders," *Physics of Fluids*, Vol. 7, No. 8, 1995, pp. 1841–1865.

[78] Mittal, R. and Balachandar, S., "On the inclusion of three-dimensional effects in simulations of two-dimensional bluff-body wake flows," *Proceedings of ASME Fluid Engineering Division Summer Meeting,Vancouver, BC, Canada*, ASME, 1997.

[79] Hay, A., Borggaard, J., Akhtar, I., and Pelletier, D., "Reduced-Order Models for Parameter Dependent Geometries based on Shape Sensitivity Analysis," *Journal of Computational Physics*, Vol. 229, 2010, pp. 1327–1352.

[80] Okajima, A., Nakamura, A., Kosugi, T., Uchida, H., and Tamaki, R., "Flow-induced in-line oscillation of a circualr cylinder," *European Journal of Mechanics - B/Fluids*, Vol. 23, 2004, pp. 115–125.

[81] Williams, D. R., Mansy, H., and Abouel-Fotouh, A., "Three-dimensional subharmonic waves during transition in the near-wake region of a cylinder," *Physics of Fluids*, Vol. 8, 1996, pp. 1476–1485.

[82] Norberg, C., "An experimental investigation of the flow around a circular cylinder: Influence of aspect ratio," *Journal of Fluid Mechanics*, Vol. 258, 1994, pp. 287–316.

[83] Evangelinos, C. and Karniadakis, G. E., "Dynamics and flow structures in the turbulent wake of rigid and flexible cylinders subject to vortex-induced vibrations," *Journal of Fluid Mechanics*, Vol. 400, 1999, pp. 91–124.

[84] Mehmood, A., Akhtar, I., Ghommem, M., Hajj, M., and Nayfeh, A. H., "Three Dimensional Effects on the Frequency Response Curve for the Inline Vibrating Cylinder," *Proceedings of the 49th AIAA Aerospace Sciences Meeting*, AIAA 2011-52, 2010.

[85] Muralt, P., "Ferroelectric Thin Films for Micro-Sensors and Actuators: a review," *Journal of Micromechanics and Microengineering*, Vol. 10, 2000, pp. 136–146.

[86] Zhou, W., Liao, W. H., and Li, W. J., "Analysis design of a self-powered piezoelectric microaccelerometer," *Proc. Smart Structures and Materials Conference. SPIE*, 2005.

[87] Inman, D. J. and Grisso, B. L., "Towards autonomous sensing," *Smart Structures and Materials Conference SPIE*, Vol. 6174, 2006, pp. 61740T.

[88] Renno, J. M., Daqaq, M. F., and Inman, D. J., "On the optimal energy harvesting from a vibration source," *Journal of Sound and Vibration*, Vol. 320, 2009, pp. 386405.

[89] Roundy, S. and Wright, P. K., "'Energy Efficient Mobile Wireless Sensor Networks," *Journal of Intelligent Materials and Structures*, Vol. 16, 2005, pp. 809–823.

[90] Capel, I. D., Dorrell, H. M., Spencer, E. P., and Davis, M. W., "The amelioration of the suffering associated with spinal cord injury with subperception transcranial electrical stimulation," *Spinal Cord.*, Vol. 41, 2003, pp. 109–117.

[91] Priya, S., Popa, D., and Lewis, F., "Energy efficient mobile wireless wensor networks," *Proc. ASME International Mechanical Engineering Congress Exposition, Chicago, IL.*

[92] Karami, M. A. and Inman, D. J., "Analytical modeling and experimental verification of the vibrations of the zigzag microstructure for energy harvesting," *Journal of Vibration and Acoustics*, Vol. 133, 2011, pp. 011002.

[93] Masana, R. and Daqaq, M. F., "Electromechanical modeling and nonlinear analysis of axially loaded energy harvesters," *Journal of Vibration and Acoustics*, Vol. 133, 2011, pp. 1–10.

[94] Abdelkefi, A., Nayfeh, A. H., and Hajj, M. R., "Modeling and analysis of piezoaeroelastic energy harvesters," *Nonlinear Dynamics*, Vol. 67, 2012, pp. 925–939.

[95] Abdelkefi, A., Nayfeh, A. H., and Hajj, M. R., "Enhancement of power harvesting from piezoaeroelastic systems," *Nonlinear Dynamics*, 2012, pp. DOI 10.1007/s11071–011–0234–9.

[96] Daqaq, M. F., "On intentional introduction of stiffness nonlinearities for energy harvesting under white Gaussian excitations," *Nonlinear Dynamics*, Vol. 69, 2012, pp. 1063–1079.

[97] Abdelkefi, A., Nayfeh, A., and Hajj, M., "Design of piezoaeroelastic energy harvesters," *Nonlinear Dynamics*, Vol. 68, 2012, pp. 519–530.

[98] Abdelkefi, A., Nayfeh, A. H., and Hajj, M. R., "Enhancement of power harvesting from piezoaeroelastic systems," *Nonlinear Dynamics*, Vol. 68, 2012, pp. 531–541.

[99] Marqui, C. D., Vieira, W. G. R., Erturk, A., and Inman, D. J., "Modeling and analysis of piezoelectric energy harvesting from aeroelastic vibrations using the doublet-lattice method," *Journal of Vibration and Acoustics*, Vol. 133, 2011, pp. 011003.

[100] Erturk, A., Vieira, W. G. R., Marqui, C. D., and Inman, D. J., "On the energy harvesting potential of piezoaeroelastic systems," *Applied Physics Letters*, Vol. 96, 2010, pp. 184103.

[101] Adhikari, S., Friswell, M., and Inman, D., "Piezoelectric energy harvesting from broadband random vibrations," *Smart Materials and Structures*, Vol. 18, 2009, pp. 115005.

[102] Ali, S., Friswell, M., and Adhikari, S., "Piezoelectric energy harvesting with parametric uncertainty," *Smart Materials and Structures*, Vol. 19, 2010, pp. 105010.